UNIVERSITÀ DEGLI STUDI DI PALERMO

Dottorato in Scienze della Terra e del Mare
Dipartimento di Scienze della Terra e del Mare
Settore Scientifico Disciplinare (GEO/08)

"Monitoring SO_2 degassing on Stromboli using a permanent UV Camera network"

IL DOTTORE
ELEONORA LO COCO

IL COORDINATORE
Prof. ALESSANDRO AIUPPA

IL TUTOR
Prof. ALESSANDRO AIUPPA

IL CO TUTOR
Dr. DARIO DELLE DONNE

CICLO XXXII
2020

Table of Contents

Acknowledgements

From my Undergraduate degree, I have to thank my supervisor Alessandro Aiuppa and also Giancarlo Tamburello for showing faith in my ability, giving me the opportunity to deepen volcanological studies on Etna and Stromboli volcano degassing.

My obvious thanks go to my co-tutor Dario Delle Donne for his precious scientific advices, without which I could not understand the world of geophysics applied to volcanoes.

A big thanks goes to Marcello Bitetto, Francesco La Monica, Angelo Battaglia, Roberto D'Aleo for their unwavering support, without them I would not have been able to present and discuss the obtained results in this Ph.D thesis.

I devote my doctorate to my little Alessandro. Thanks to the immense joy and energy he gave me, this journey was unique. I would like to thank my partner Andrea immensely for always supporting me. He gave me the strength to go ahead and fulfill my aspirations.

A special thank goes to my parents (Michela e Andrea), for always helping me, for accepting any choice I did in my life, for allowing me to study, for never having made me miss anything and having transmitted to me the values of life. I thank them and the parents of Andrea (Adriana and Gino) for being always present and taking care of Alessandro at any necessity. An affectionate thank go to my aunt Giusy for her support and encouragement.

Furthermore, I am grateful to all people who were present during all the trips abroad during my Ph.D.

I wish to thank prof. Theodoros Ntaflos for hosting me at the University of Wien and teaching me on electron microprobe analysis, for his kindness and hospitality. I will never forget the moments spent together, the dinners with his wife Lisa, and the stuffed animal (since then nicknamed Theo) that they gave to Alessandro and that keeps him company on nights.

I wish to thank prof. Andrew McGonigle, Dr. Tom Pering and all Sheffield Volcano Group who welcomed me as one of them. I will never forget the lunches spent with them talking about volcanoes over a good English beer.

Finally, a special thanks to prof. Andrea Di Muro and his family for the hospitality, the logistic support, and friendship provided during my family and my stays at La Reunion Island. I will never forget the unique moments spent with them and with the IPGP group of the "Observatoire volcanologique du Piton de la Fournaise", especially when I went up to the Dolomie crater, where I could admire an incredible volcanic scenario.

To all the other people I have encountered me. Especially, my dear friends Stella, Erica, Vincenzo and my Ph.D colleague João. I already know that I will miss our talks about life and science in front of a cup of coffee.

My apologies for the numerous others that I have almost certainly forgotten to mention.

Abstract

Magmatic degassing plays a key role in the dynamics of volcanic activity. Volatiles carry crucial information on pre- to sin-eruptive processes at active volcanoes. Measurements of crater plumes emission rates, therefore, improve our understanding of degassing processes and magmatic conditions at depth, and contribute decisively to eruption forecasting and risk mitigation at highly hazardous volcanic settings

In this study, I take advantage of the UV camera technology to characterize the SO_2 release from Stromboli volcano at high spatial and temporal resolutions. This allows for comparison of degassing, seismic, infrasonic and thermal datasets, and opens new, interdisciplinary opportunities to deepen our understanding of volcanological processes. This multidisciplinary approach allows for a better characterization of Stromboli's SO_2 degassing dynamics, and contributes to our understanding of the volcano's shallow plumbing system.

Strombolian activity is the focus of most studies, albeit represents only a minor fraction of the total gas output at Stromboli. Indeed, explosive activity is accompanied by continuous passive emissions that represent the largest fraction of Stromboli's 'bulk degassing'. Here, we focus on the implications of using UV Camera networks to understand Stromboli's SO_2 flux behaviour during "regular"

Strombolian activity. To do so, we report on reporting (in Chapter 4) a ~ 4.5 year-long (June 2014–December 2018) UV camera based SO_2 flux time-series.

The analysis of that encompass the August 2014 effusive eruption and 4 years of "regular" Strombolian activity allows to constrain the volcano's SO_2 degassing activity, mostly characterized by passive degassing.

The recorded signals reflect the temporal fluctuations of magma supply to the shallow conduit. High to very high levels are only observed prior and during effusive eruptions, when the magma input rate in the conduit accelerates to >0.3 m^3/s. During 'regular' activity, SO_2 emissions and magma input rates are systematically lower. This robust SO_2 flux dataset enables the study of ordinary and effusive activity phases of Stromboli volcano, suggesting possible SO_2 thresholds for volcanic monitoring.

The obtained results further demonstrate that SO_2 flux time-series at Stromboli exhibit yearly cyclic modulations, likely related to seasonal variations in sunlight illumination, and meteorological conditions. Variations prior and during the 2014 eruption are well beyond these seasonal trends.

Stromboli releases gases from three active craters (North-East crater, NEC; South-West crater, SWC; Central crater, CC) located at an elevation of ~750 m above sea level. Each one of them is characterized by a distinct degassing and explosive regime, are likely to contribute to the total volatile flux differently. Due to complex conduit systems, the temporal observation of different crater vents is mandatory in order to improve the capability of forecasting rapid changes of magmatic activity at depth. This requires the use of at least two UV cameras located in strategic sites.

In Chapter 5, I report on high frequency (~0.5 Hz) automated measurements of the SO_2 flux at Stromboli, obtained by the UV camera network aforementioned. The network is composed of two ad-hoc designed and stand-alone permanent UV cameras, located on north-eastern and south-western upper flank of Stromboli. The strategic positions of these UV cameras allow, for the first time at this volcano, to simultaneously resolve SO_2 emissions from the northern (NEC) and central-southwestern (SWCC) crater vents. These results, in tandem with infrasonic and seismic measurements, also allow discriminating active (explosions+puffing) vs. passive (quiescent) SO_2 contributions. This highlights substantial swings in degassing activity between the two craters during <8 months of observations (June 2017 - January 2018). Importantly, these crater-to-crater modulations in SO_2 emissivity correspond to consistent shifts in infrasound source, thus validating our spatially resolved SO_2 flux records. Clustering of degassing activity at the NEC corresponds to periods of heightened explosive activity, as demonstrated by SO_2 and seismic records. This is interpreted as due to preferentially gas/magma channeling into the structurally weaker NE portion of the crater terrace as the supply rate of buoyant, bubble-rich magma increases in the shallow plumbing system. These vent-resolved degassing results of Stromboli volcano contribute to our ability to forecast effusive eruptions with direct implication on early warning procedures.

As in other persistently active, open-vent basaltic volcanoes, strong and hazardous explosions periodically interrupt Stromboli volcanic activity. Rapid transitions from quiescent degassing to high-energy explosive eruptions poses a significant challenge for volcanic hazard evaluation and mitigation. The source mechanism of the "major" explosions is not yet well understood, even though these are far more frequent and potentially even more hazardous than paroxysmal events.

Here, making use of the high spatial resolution of UV cameras, to resolve SO_2 emissions from Stromboli craters during two major explosions that occurred on 1 November 2017 and 24 April 2018 (Chapter 6). I analyze in detail the SO_2 flux of the explosive sequences from the beginning to the final stages of gas codas. Moreover, I calculate explosive SO_2 masses, and estimate the first SO_2 budget from these two major explosions at Stromboli. Our results point to a dominant active (over-pressurized) degassing mode persisting for minutes even after the main explosive blast and dominating the SO_2 gas budget during a major explosion event. For the first time, the degassing magma volume sustaining a major explosion has been estimated based on UV camera measurements. This can be only compared with the volume of erupted products. Currently, there is no constrain about the correspondence between the volume of magma feeding the explosions and the products effectively erupted. The volume of degassing source magma, calculated for 1 November 2017 major explosion, is much higher than the ~100 m^3 of magma erupted during major explosions (Aiuppa et al. (2010).

Furthermore, I apply some basic statistical analysis to a dataset of 3655 ordinary explosions and the two major explosions aforementioned. The calculated SO_2 mass for major explosion implies the occurrence of an explosion every ~688 days. The obtained results suggest that ordinary and major explosions at Stromboli are not driven by the same magma degassing dynamics inside Stromboli's crater conduits.

This multidisciplinary study drives forward our understanding of the complex link between low and high-energy explosive events in Stromboli, with immediate implications for eruption forecast and precursory detection of volcanic unrest at Stromboli.

Introduction

Volcanic gases are important tracers of volcanic activity and one of the most evident signs of activity even during non-eruptive periods. Therefore, volcanic gas geochemistry has always played an important role in volcano monitoring (Oppenheimer et al., 2003; Galle et al., 2003). The study of chemical and isotopic composition of volcanic gas emissions has helped volcanologists to understand magmatic sources and magma evolution over time. The composition of subaerial gas emissions at Earth's surface represent the final stage of complex migratory processes governing the release of volatiles from rising and/or stationary degassing magma. Therefore, constrains on compositions (e.g., CO_2/S_T; Aiuppa et al., 2007, 2009) and fluxes (e.g., SO_2 fluxes; Burton et al., 2009, 2015; Tamburello et al., 2011; Delle Donne et al., 2017) of volcanic gases over time are important parameters in volcanic surveillance, and may assist in the detection of fresh magma migrating toward shallower reservoirs. Furthermore, inferences on magma migration are more constrained when gas measurements are combined with other observations, such as geophysical signals (Ripepe et al., 2005; McGonigle et al. 2009; Dalton et al., 2010; Kazahaya et al., 2011; Tamburello et al., 2012; Waite et al., 2013; Nadeau et al., 2011, 2015; Delle Donne et al., 2016, 2017).

Until recently, the methods used to measure volcanic plumes did not have the ability to detect rapid changes in outgassing, on the scale of standard geophysical observations. Over the past decades, however, remotely sensed observations of volcanic phenomena have increased substantially. This provides additional benefits such as high temporal resolution operation, real-time processing, and the possibility of data acquisition, even during eruptions.

Despite its relatively minor abundance in magmas (compared with H_2O and CO_2), sulfur has a great relevance in volcano monitoring. The advantages offered by SO_2 degassing measurements are: i) the existence of a strong contrast between the abundance of this gas in the atmosphere (~ 1 ppb) and in volcanic plumes (> 1 ppm); ii) the relationship between the pressure-dependent solubility of this gas

in magmas, which determines the relationship between SO_2 fluxes and magma fluxes degassing in magmatic reservoir or in volcanic conduits. Hence, SO_2 can help understanding magmatic evolution (including the processes triggering eruptions) and represents one of the most suitable tracers for volcano monitoring and hazard assessment.

UV cameras (Mori and Burton, 2006, 2009; Bluth et al., 2007; Dalton et al., 2009; Kantzas et al., 2010; Kern et al., 2010b) represent a useful tool for estimating degassing rates (which are difficult to measure based on point sampling) and detecting rapid changes in gas emissions. In recent years, UV camera has laid the foundations not only for estimating SO_2 fluxes, but also for understanding the dynamics of magma degassing and the role of volatiles in explosive events (Mori and Burton, 2009; Dalton et al., 2010; Pering et al., 2014b, 2016). The combined ability to measure gas emissions, released quickly and from different sources, allows the UV camera to discriminate and quantify gas fluxes resulting from different styles of volcanic activity. This opens up the possibility for new insights into magmatic dynamics, such as the relative proportion of gas released during quiescent degassing compared to that released in explosions (Tamburello et al., 2012; Delle Donne et al., 2017).

Changes in SO_2 degassing rates have been associated with the rise of magma to shallower levels (Casadevall et al., 1983). The potential of this parameter as a precursor of eruptive events has been demonstrated for several years in various volcanic contexts. Numerous campaigns to measure SO_2 emissions have been carried out in Stromboli (Stoiber et al., 1983; Francis et al., 1993; Allard et al., 1994; Burton et al., 2007b, 2009, 2015; Tamburello et al. 2012; Pering et al., 2014a; Barnie et al., 2015), on Etna (Pering et al., 2014a, 2014b; Peters et al., 2014; Tamburello et al., 2013) and in many other volcanoes (Pacaya volcano, Dalton et al., 2010; Santa Ana volcano, Olmos et al., 2007b; Galeras volcano, Zapata et al., 1997; Asama volcano, Kazahaya et al., 2011; Fuego volcano, Nadeau et al., 2011; Santiaguito volcano, Holland et al., 2011). However, the level of SO_2 emissions is relative and almost unique to each volcano. Hence, continuous measurements are needed to establish a degassing model for quiescence periods, and to detect anomalies that may suggest a deviation from the status of 'normal' activity.

In this direction, recent automated processing and interpretation of SO_2 fluxes from permanent monitoring UV camera stations (D'Aleo et al., 2016, 2019; Delle Donne et al., 2017, 2019) provide continuous and robust datasets. This allows to obtain new information on gas fluxes mechanisms of magmatic conduits that can trigger explosive eruptions. A further advancement of current technologies, in the future, could lead to the prediction of high hazardous volcanic phenomena (paroxysms, major eruptions). Defining the processes that underlie the dynamics of explosive

degassing represents a great step forward in the evaluation of volcanic risk and development of early warning systems.. The focus of Chapter 6 goes in this direction.

The object of my Ph.D thesis is Stromboli volcano. Stromboli volcano is considered one of the most active volcanoes on Earth, due to the extraordinary continuity of its eruptions over the past 1700 years (Rosi et al., 2000), and represents a suitable natural laboratory to perform measurements on volcanic emissions, which are key indicators of the state of activity of a volcano and the magmatic dynamics of its feeding system.

The following is an overview of the Chapters that compose this Ph.D thesis.

The aim of **Chapter 2** is to briefly introduce Stromboli degassing system and describe its (explosive and passive) degassing behaviors, which are the main focus of this thesis. The second part of this Chapter is focused on the UV camera technique and its application on volcanic degassing phenomena. **Chapter 3** includes UV camera specifications and methodological details, used within this thesis (acquisition and data processing), to obtain SO_2 fluxes at Stromboli volcano during observational period. Within **Chapter 4,** the main focus is to characterize 'regular' passive degassing of Stromboli thanks to the longest and most continuous UV camera based SO_2 flux time-series ever recorded. A network of two automatic and permanent UV cameras allows, for the first time at Stromboli, to simultaneously resolve SO_2 emissions from the northern (NEC) and central-southwestern (SWCC) crater vents. The obtained results are presented in **Chapter 5**. SO_2 fluxes highlight substantial fluctuations, which correspond to importantly consistent shifts in infrasound source, in degassing activity in between the craters during <8 months of observations (June 2017 - January 2018). Finally, **Chapter 6** is focused on the study of two major explosions that occurred at Stromboli on 1 November 2017 and 24 April 2018. Three main goals are presented in this Chapter: (i) measurement of the first SO_2 budget for two major explosions at Stromboli; (ii) estimations of the degassing magma volume feeding Strombolian and major explosions at Stromboli; (iii) understanding the relation between ordinary and major explosions.

– Chapter 2 –
"State-of-the art"

2.1. Stromboli volcano: geology, eruptive and degassing behavior

Stromboli is one of the most active volcanoes on Earth. Since ancient times, Stromboli is known as "the lighthouse of the Mediterranean" for the glow of its frequent explosions, visible from a great distance. Indeed, Stromboli has been steadily erupting for more than 2000 years (Rosi et al., 2000), Aristotele was the first to describe its activity, which has persisted for perhaps as much as 5000 years (Allard et al., 1994).

The volcano began to develop about 100 thousand years ago on 18 km thick crust (Pasquaré et al., 1993). Stromboli is a composite cone located at the northern end of the Aeolian island arc in the Tyrrhenian sea of the southern coast of Italy. The island rises about 3000 m from the seafloor and stands 924 m above sea level, reaching its highest altitude in the Vancori peak. The surface of the island (12.5 km^2) is estimated to be 25 times smaller than the submarine base area of the entire volcano (Kokelaar and Romagnoli, 1995), thus giving a total conical volume of ~ 25 x 10^4 km^3.

The present edifice is the result of several growth stages and eruptive Cycles, with 30 stratigraphic units documented (Hornig-Kjarsgaaredt al., 1993) (Figure 2.1). The correlation between major geochemical and petrological variations in the composition of erupted products, and the inferred occurrence time of main volcano-tectonic events, suggests a strong structural control on the evolution of eruptive activity (Hornig- Kjarsgaarde t al., 1993). Individual growth stages all appear to be controlled by a zone of structural weakness striking NE-SW, as evidenced by the predominance of lineaments, dikes, and brittle structures along this particular direction (Pasquarè et al., 1993). The morphology of the N-NW flank of the volcano is dominated by the Sciara del Fuoco whose formation is attributed to a sequence of sector collapses and landslides occurred in the last 13,000 year (Pasquarè et al., 1993; Tibaldi, 2000).

The currently active vents are located within a 250-m-long and 150-m-wide crater terrace (Chouet et al., 2003). Stromboli degasses from the three active craters (North-East crater, NEC; South-West crater, SWC; Central crater, CC) that are located at an elevation of ~750 m above sea level. The three craters are characterized by distinct degassing and explosive regimes (Ripepe et al, 1994; Harris and Ripepe, 2007; Ripepe et al, 2008), and are therefore likely to contribute differently to the degassing budget.

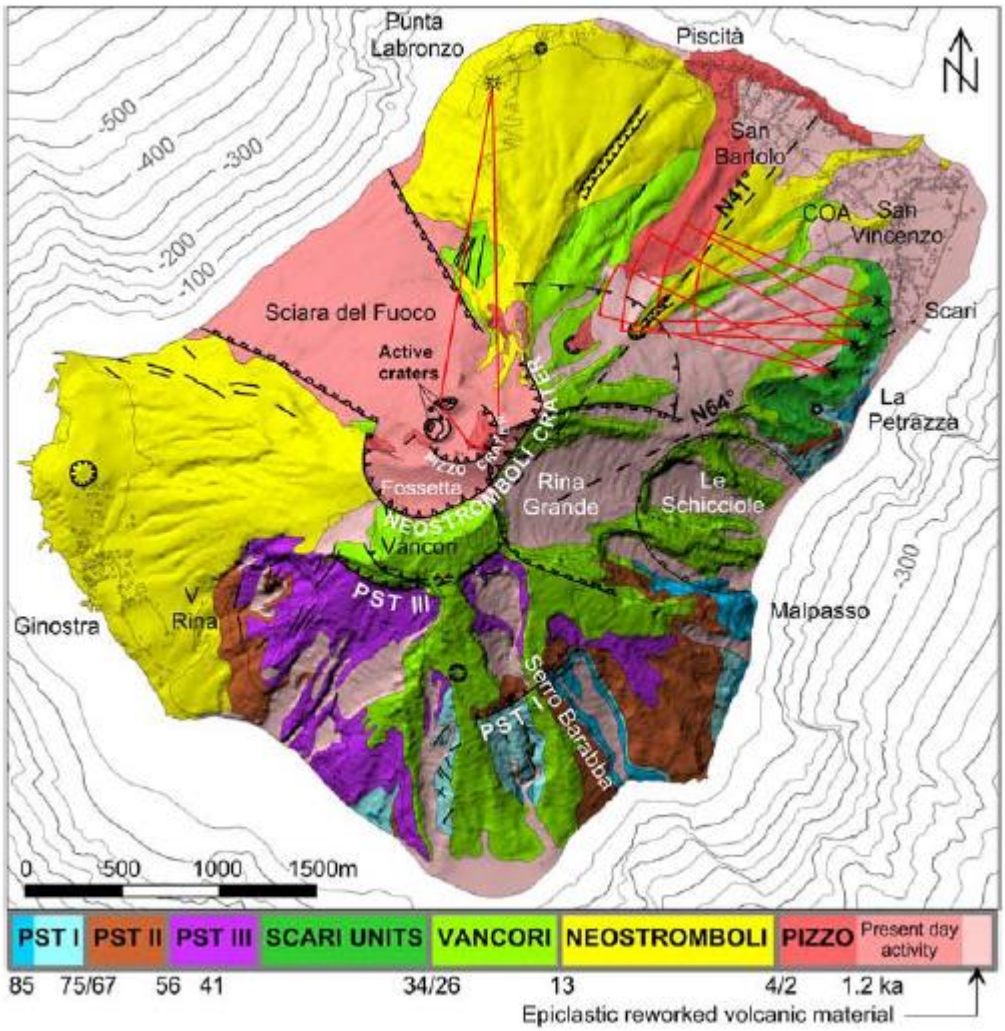

Figure 2.1 *Simplified geological map of Stromboli volcano showing the different stages constituting the evolution of the edifice (modified from Keller et al., 1993; Francalanci et al., 2013). (after Nappi et al., 1999; after Keller et al., 1993; after Romagnoli et al., 2009; after Finizola et al., 2002) (from Linde et al., 2014).*

Given the explosive frequency and ease of access to the summit area, Stromboli is one of the most widely studied basaltic volcanoes. These studies include petrological (e.g. Pichavant et al., 2009, 2011, 2013; Metrich et al. 2001, 2010; La Felice and Landi, 2011a), seismic (e.g. Chouet et al. 1999,2003; Ripepe et al., 2005), infrasonic (e.g. Ripepe et al. 2002, 2007), and thermal (e.g. Patrick et al. 2007; Delle Donne and Ripepe, 2012) information. Work also has been done on explosion dynamics (e.g. Taddeucci et al. 2012; Gaudin et al., 2014), on the dynamics of slug generation (e.g. Jaupart and Vergniolle, 1988; Wilson, 1980; Parfitt and Wilson, 1995), modelling (e.g. James et al. 2004; 2006; 2008; Suckale et al. 2010b; Del Bello et al. 2012; 2015) and degassing (e.g. McGonigle et al. 2007, 2009; Mori and Burton, 2009; Burton et al. 2007; Tamburello et al. 2012; Delle Donne et al., 2017). Moreover, interdisciplinary studies are carried out (Harris and Ripepe, 2002; Marchetti et

al., 2008; Landi et al., 2011; Delle Donne et al., 2017). This is by no means an exhaustive list but gives an overview of the importance of Stromboli as a volcanic target of study.

These studies over the past few decades allowed a better understanding of the complex feeding system (or plumbing system) sustaining Stromboli's activity (Harris and Ripepe, 2007; Pichavant et al., 2009; Métrich et al., 2010; Aiuppa et al., 2009, 2010) (Figures 2.2 and 2.3). Isotopic geochemistry and analysis of Stromboli's recent products are consistent with the presence of a multi-reservoir polybaric system, which includes at least three different reservoirs (Francalanci et al., 2005). The most superficial magma storage zone is located at a depth of ~ 300 m, and consist in a dyke-conduit system located by seismic events associated with Strombolian activity (Chouet et al., 1999, 2003; Marchetti and Ripepe, 2005). Below this, fluid and melt inclusions suggest the presence of two reservoirs at ~ 3.5 km, and 7-11 km (Bertagnini et al., 2003; Vaggelli et al., 2003; Mètrich et al., 2001, 2010).

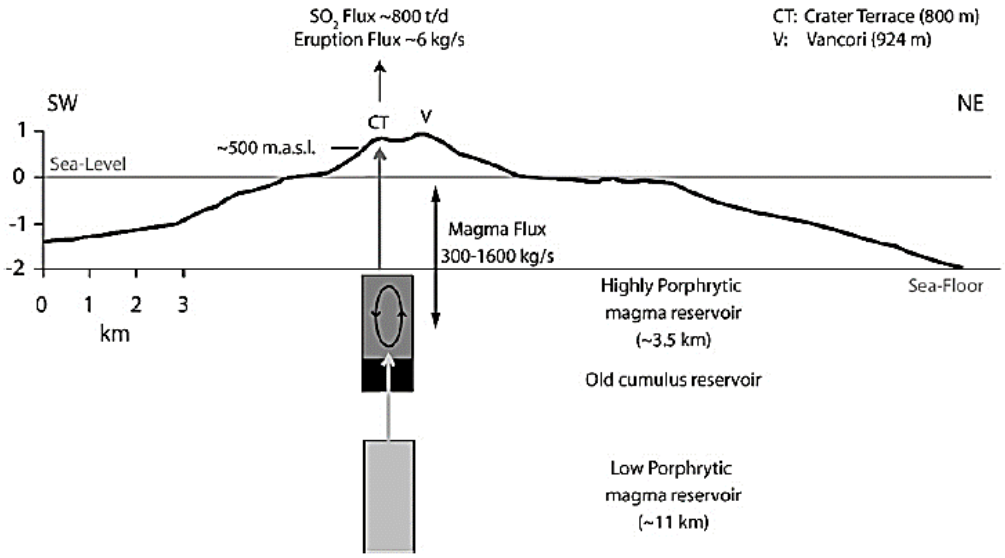

Figure 2.2 *Stromboli sub-volcanic plumbing system model. SO_2 flux data from Allard et al. (1994) and Harris and Stevenson (1997b). At 500 m b.s.l is localized the shallow system, VLP waves source (from Harris e Ripepe, 2007).*

Stromboli erupts two main types of products. Each can be associated with a different parent magma (Corsaro et al., 2005; Francalanci et al., 2005; Bertagnini et al., 2003): a magma with low porphyricity (LP) and a magma with high porphyricity (HP). While the HP magma is erupted during normal Strombolian activity and includes degassed glasses with high contents, the LP magma (or so-called 'golden pumice') is only erupted during the most energetic eruptions, is rich in volatiles, with has low phenocrysts content (Corsaro et al., 2005; Francalanci et al., 2005). According to the model of Francalanci et al. (2005), and Mètrich et al., (2001, 2010), the LP magma reservoir is located in the

deepest level, and feeds the most superficial reservoir containing the HP magma. HP magma derives from LP magma from a continuous process of crystallization of plagioclase, clinopyroxene and olivine, to which is added a repeated mixing that feeds the LP magma (Francalanci et al., 1999, 2004; Bertagnini et al., 2003).

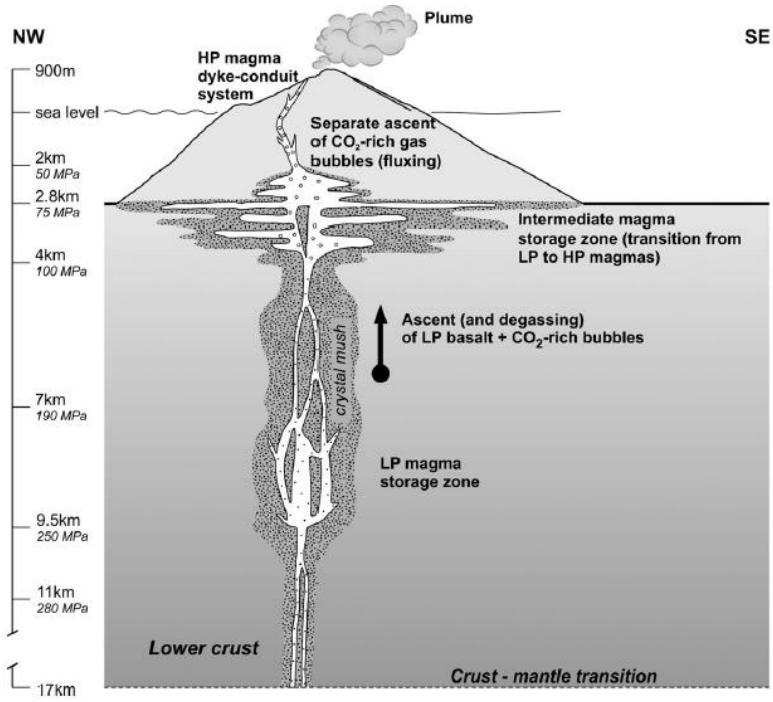

Figure 2.3 *Schematic cross-section showing the main features of Stromboli's crustal plumbing system. Stromboli's quiescent and syn-explosive gas emissions result from the mixing of gases persistently sourced by (i) degassing of dissolved volatiles in the HP magma filling the upper (<1 km) dyke-conduit system; and (ii) CO_2-rich gas bubbles, originated at depth (at depths >4 km) in the plumbing system. shallow and deep gas contributions are concur to determine gas discharges. Temporal gas fluctuations are at the base of the variability in Stromboli's gas emissions. The signatures of phases characterized by CO_2-enriched surface emissions reflect an increasing of gas-rich deep bubbles supply. Hence, plume emissions CO_2-rich are potentially being precursory to large scale deeply-sourced paroxysms (from Aiuppa et al., 2010).*

Stromboli exhibits a wide range of degassing regimes from passive degassing to explosive dynamics. Strombolian-type volcanic activity was first defined at Stromboli volcano, Italy (Mercalli, 1881). Strombolian activity consists of continuous non-explosive degassing interrupted by rhythmic, short-lived, mild explosions of gas and incandescent magma (e.g. Houghton and Gonnermann, 2008, for review) (Figure 2.6 b). Explosions can be divided into ash-free and ash-rich types depending on the grain size of the ejected materials (Chouet et al., 1999; Ripepe and Marchetti, 2002; Patrick et al., 2007).

Subject to the level of activity, explosions can further be less or more frequent and/or intense (e.g. Harris and Ripepe, 2007a; Ripepe et al., 2008). *Ordinary Strombolian explosions* at Stromboli are characterized by emissions lasting seconds to tens of seconds and occurring at a typical rate of 8-17

events per hour (Calvari et al., 2008; Chouet et al., 1974; Ripepe et al., 2008; Taddeucci et al., 2012a). Persistent Strombolian activity varies in style and intensity. Strombolian explosions eject well-collimated jets of gas, laden with molten lava fragments and mm- to m-sized pyroclasts, expelled up to several hundred meters high (between 0.01 and 10 m^3; Chouet et al., 1974; Ripepe et al., 1993; Barberi et al., 1993), at typical velocities of 10–50 $m \cdot s^{-1}$, falling within 100 m from the vent (Chouet et al., 1974; Ripepe et al., 1993). Gas and ejecta masses are estimated in the range 0.4–1550 kg (Vergniolle and Brandeis, 1996; Mori and Burton, 2009; Taddeucci et al., 2012b) and 8–32000 kg (Chouet et al., 1974; Ripepe et al., 1993; Taddeucci et al., 2012b; Gaudin et al., 2014), respectively. Recent measurements of SO_2 explosive masses, obtained with UV camera technique, range between <1 to 200 kg (Tamburello et al., 2012; Delle Donne et al., 2017).

Few volcanoes have contributed more to our understanding of magma-gas interactions during volcanic explosions than Stromboli (Ripepe et al., 2005). Many studies have been conducted to understand this complex interaction in the conduit, which is at the origin of the Strombolian activity (Chouet et al., 2003; Gaudin et al., 2017; Jaupart and Vergniolle, 1988; Ripepe et al., 2001, 2002, 2008). The persistent Strombolian explosions are thought to result from the burst of large over-pressurized gas 'slugs' (large bubble of magmatic gas) at the top of the magma column (Chouet et al. 1974; Blackburn et al., 1976; Wilson et al., 1980; Patrick et al., 2007; Ripepe et al., 1993, 2008; James et al., 2009; Taddeucci et al., 2012b; Colò et al., 2014; Del Bello et al., 2012, 2015; Beckett et al., 2014; Gaudin et al., 2014; Leduc et al., 2015; Capponi et al., 2016b). Slugs are generated at ≤3 km depth and rise rapidly to the surface (Burton et al., 2007a; Métrich et al., 2010). The actual mechanism of slug formation is however still a point of debate (see Parfitt, 2004, for review). Two models have been derived from mathematical modeling and/or laboratory experiments. According to the rise speed dependent (RSD) model, bubble coalescence leads to the formation of larger bubbles which ultimately coalesce into a slug (Wilson and Head, 1981; Parfitt and Wilson, 1995); in the second model (CFD) slugs originate from the accumulation and collapse of a foam layer at geometrical discontinuities within the plumbing system (Jaupart and Vergniolle, 1988, 1989) (Figure 2.4). In both cases gas slugs rise at much faster rates than melt to cause Strombolian explosions at the surface. In principle, both models are thus consistent with Strombolian behavior.

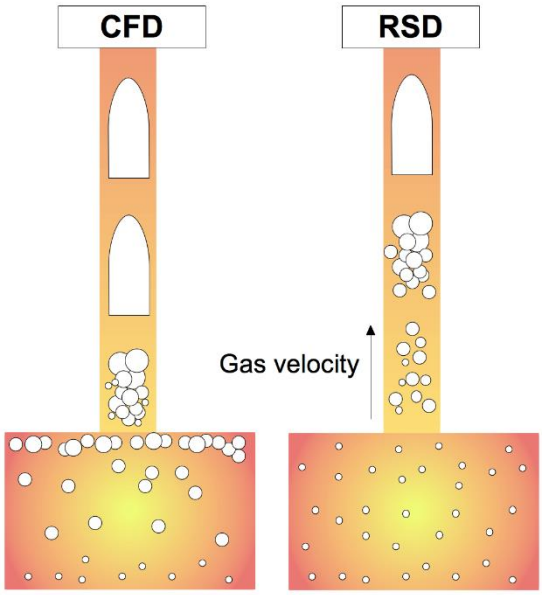

Figure 2.4 *Schematic sketch illustrating the current models of slug formation. In the rise speed dependent model (RSD),the differential rise speed of various-sized bubbles in the conduit leads to coalescence, and thus to the formation of larger bubbles which ultimately coalesce into a slug. In the foam collapse model (CFD) small bubbles accumulate below a structural boundary in the conduit, e.g. below the top of an intercalated magmatic reservoir, until a critical bubble layer thickness is reached. The bubble layer then collapses into a slug.*

In this regard, James et al. (2004) showed that inclined conduits, with respect to vertical ones, promote a shift from bubbly to slug flow, where the increase in the size of gas pockets occurs at the expense of their release frequency. A volcanic conduit will rarely be perfectly cylindrical (e.g. Seyfried and Freundt, 2000), and at Stromboli there is strong evidence for a kinked conduit (Chouet et al. 2008). Stromboli explosion frequency and intensity are strictly related: when slugs form more frequently, they also tend to incorporate greater masses of gas, thus feeding stronger explosions (Taddeucci et al., 2013).

Persistent Strombolian activity is sustained by continuous magma overturning in the shallow conduits (Gilberti et al., 1992; Allard et al., 1994, 2008; Harris and Stevenson, 1997; Chouet et al. 1974) and is accompanied by *continuous passive degassing* (Allard et al., 1994, 2008; Burton et al., 2003, 2009) and *"puffing"* (small amounts of gas are emitted without pyroclasts) every few seconds (Ripepe et al., 1996; Ripepe & Gordeev, 1999; Ripepe et al., 2002; Harris and Ripepe, 2007; Tamburello et al.,2012; Gaudin et al., 2017a, 2017b) (Figure 2.6 a). Passive degassing is the result of non-pressurized (quiescent) gas release from volcanic conduit. It is linked to magma recycling and to raise of small gas bubble released into atmosphere without generating seismic or infrasonic activity (Ripepe et al., 1996; Ripepe et al., 2002). Puffing activity can be accompanied by an infrasonic signal and occurs over longer repose periods.

Persistent degassing by magma residing in the Stromboli's shallow conduits feeds a volcanic plume that persists between and during explosive emissions. Degassing levels vary with volcanic activity, with periods of low and high activities corresponding with SO_2 fluxes of <150 t/d and >>500 t/d,

respectively (Burton et al., 2003, 2009; Tamburello et al., 2012; Delle Donne et al., 2017).

Ongoing research at Stromboli volcano has left a puzzling set of observations. In fact, there is some controversy concerning the characteristics of Strombolian behavior. The relationship between explosive style and explosive degassing is poorly constrained and subject of contradictory observations (Lautze and Houghton, 2007; Patrick et al., 2007). Conversely, long-standing research has created a convincing general model to explain quiescent activity. Today, it is widely agreed that the particular modes of gas release reflect different mechanisms of gas segregation (Parfitt, 2004; Burton et al., 2007b; Namiki and Manga, 2008). Open-system degassing is associated with non-explosive behavior as gas escapes through permeable pathways inside the conduit (Allard et al., 1994; Polacci et al., 2008). Burton et al. (2007b) stressed the important role of gas percolation in this context. Using constraints from literature data on the petrology and texture of erupted material and geochemical measurements of gas emissions, together with a model of gas solubility, they developed a conceptual model for quiescent degassing (see Figure 2.5).

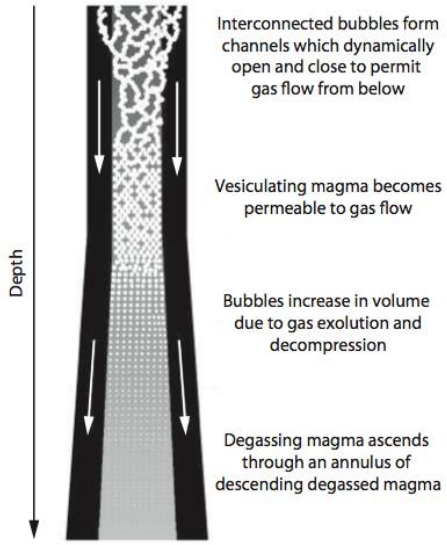

Figure 2.5 *Schematic sketch of the current model for quiescent degassing (modified after Burton et al. (2007b)). Juvenile magma ascends from depth through an annulus of descending degassed magma. During ascent the void fraction of the magma increases due to gas exsolution and decompression. At a vesicularity of ~0.5 the magma becomes permeable to gas flux, and interconnected bubbles start to form pathways permitting efficient degassing from below.*

In their model steady-state gas release is sustained via magma circulation of ascending vesiculated and descending degassed magma in the conduit (compare Kazahaya et al., 1994; Stevenson and Blake, 1998; Palma et al., 2011). Continuous vesiculation drives ascending magma towards the percolation transition, above which it becomes permeable to gas flux. In this way, transition from closed- to open-system conditions allows for quiescent gas escape without the eruption of magma.
The eruptive activity of Stromboli also includes explosions of higher energy, called “major explosions”, whose recurrence time is of months/years (Barberi et al., 1993; Bertagnini et al., 1999; Andronico and Pistolesi 2010; Pioli et al., 2014; Rosi et al. 2006; Giudicepietro et al., 2019), and

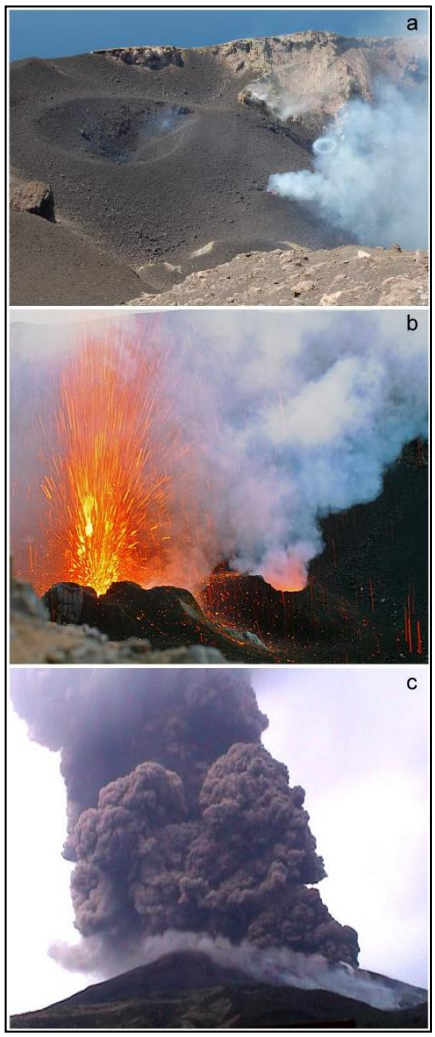

Figure 2.6 *Main types of Stromboli eruption. (**a**) A panoramic view of part of the Stromboli crater terrace. 'Puffing', visible on the right side of the image; (**b**) A typical Strombolian explosion from a vent (on the left side) with simultaneous degassing with the adjacent vent (on the right side) in the SW crater; (**c**) A still picture of the paroxysmal explosive event of 5 April 2003 captured ~ 1 sec after the beginning of the eruption (09h13m local time). The vertical height of the image is ~ 2 km (from Del Bello et al. 2012)*

rarer large paroxysms (Bertagnini et al., 2003; Métrich et al., 2005; Calvari et al., 2006; La Felice and Landi, 2011b; Ripepe & Harris, 2009; Aiuppa and Federico, 2004; Aiuppa et al., 2010, 2011; Bonaccorso et al., 2012; Andronico and Pistolesi, 2010; Pistolesi et al. 2011; Rosi et al, 2013) (Figure 2.6 c).

This type of explosions is associated with the greatest risk, given the projection of bombs up to a few kilometers away and the large volume of erupted material compared to ordinary activity. Even more energetic and hazardous "paroxysmal events" have recurrently been observed on Stromboli volcano, in the order of >25 in the last two centuries (Barberi et al. 1993; Rosi et al., 2013). The plume generated by these events has reached 4 km in height (Rosi et al., 2006, 2013; Barberi et al., 1993, 2009; Pioli et al., 2014).

Two main alternative models have been proposed to explain the generation of paroxysms at Stromboli. Bertagnini et al. (2003) and Métrich et al. (2010), based on the evidence that low

porphyritic and highly vesicular pumice fragments are systematically erupted during paroxysmal eruptions, first proposed that such events are triggered by the fast (in a few hours or days) ascent of volatile-rich (~2 wt. % CO_2 and 2.5–3.5 wt. % H_2O) basaltic magma blobs from a 7–10 km deep reservoir. Instead, Allard (2010) argued that Stromboli paroxysms are caused by the catastrophic release of CO_2-rich gas blobs, deriving from collapse of a previously accumulated bubble foam layer. Although these models are divergent in some aspects, they do clearly suggest that the magmatic gas phase is a driving force for these deeply sourced explosions. A third model has proposed by Calvari et al. (2011). The authors suggest that intense effusive activity and removal of the associated magma-static load can cause a decompression of the plumbing system, capable of triggering paroxysmal eruptions.

Ordinary explosive activity is occasionally (1985, 2002–2003, 2007, 2014, 2019) interrupted by lava effusions in the northwest Sciara del Fuoco (SdF) slope of Stromboli's edifice (Ripepe et al., 2005, 2009, 2017, 2019; Burton et al., 2009; Rosi et al., 2006, 2013; Calvari et al., 2011; Valade et al., 2016; Delle Donne et al., 2017; Di Traglia et al., 2019). These events may even cause tsunamigenic landslides (La Rocca et al., 2004; Tinti et al., 2005, 2006; Chiocci et al., 2008; Pino et al., 2004, 2009; Pistolesi et al., 2020) with a direct impact on the Tyrrhenian Sea islands, as lastly occurred in December 2002.

2.2 Previous studies on SO_2 degassing at Stromboli

2.2.1 SO_2 flux measurements before the advent of UV cameras

The traditional approach to volcanic SO_2 measurements involved direct sampling at fumaroles and vents (Symonds et al. 1994). Direct sampling methods did not allow SO_2 flux (sometimes referred to as emission rate $kg \cdot s^{-1}$) to be derived, and there were a multitude of associated issues, including poor time resolution, the potential for contamination in transport of samples to the laboratory for analysis .and the potential dangers or inaccessibility to sampling areas/volcano summits (Tamburello, 2011a).

In light of these difficulties, the benefits of using remote sensing techniques to measure gases became soon more apparent, including both airborne (i.e. satellites, not discussed here) and ground based measurements. One of the earliest of these techniques was the use of Correlation Spectrometers (COSPECs; Newcomb and Millan, 1970; Moffat et al. 1971; Moffat and Millan 1971; Stoiber et al. 1983). This technique is based upon the solution of the Lambert-Beer Law:

$$I(\lambda) = I_0(\lambda) \cdot e^{-\sigma(\lambda) \cdot N \cdot L} \quad \text{(Eq. 1)}$$

where I(λ) is light intensity after passing through the plume (or target area), I_0 (λ) is light intensity before passing through the plume, σ(λ) is the absorption cross-section for the particular gas of interested (e.g. SO_2), N is the number of molecules in the optical path and L is the plume width. SO_2 was quickly identified as an ideal target gas for these observations relative to the other major plume volatiles e.g., CO_2 and H_2O, due to its comparatively low background concentration and strong absorption features (Tamburello, 2011a).

The ability to measure SO_2 emissions remotely, even for erupting volcanoes, was an important step forward for Volcanology, and despite potential difficulties in interpreting SO_2 flux data (Oppenheimer et al., 1998a; Symonds et al., 2001), COSPEC has played an important role in many eruptive crises, including Kilauea in 1979, Pinatubo in 1991 (Hoff, 1992; Daag et al., 1996; Sutton et al., 2001), Mount St. Helens in 1980 (Casadevall et al., 1983) and Montserrat since 1995 (Young et al., 1998). COSPEC was then succeeded by Differential Optical Absorption Spectroscopy (DOAS) (Platt and Stutz, 2008). DOAS involved the use of smaller and less expensive USB spectrometers that were easier to use in volcanic setting and involved analysis across the entire UV spectrum (McGonigle et al. 2002; Galle et al. 2003; Tamburello, 2011a). There are several differing DOAS techniques including: traversing DOAS, scanning DOAS and the cylindrical lens DOAS. Traversing DOAS involves travelling beneath a plume (by car, boat or foot) with a vertically pointing USB spectrometer collecting scattered skylight. An integrated column amount (ICA) can then be determined over the length of the traverse by integrating overhead concentrations over the plume width. This reading can then be used to determine SO_2 fluxes from knowledge of the plume transport speed (Tamburello et al. 2011a). Scanning DOAS involves an instrument at a fixed position; it can be particularly useful for permanent stations and offered a marked improvement in time resolution (a measurement every few minutes).

The first measurements of total SO_2 fluxes emitted from Stromboli craters date back to 1975 and were elaborated using the a ground-based Correlation Spectrometer (COSPEC, Stoiber et al., 1978; Caltabiano and Romano, 1988). SO_2 fluctuated between 130–1,500 tons per day (t/d), with mean values of ~300 t/d (Malinconico, 1987; Allard et al., 1994; Weibring et al., 1998, 2002; Burton et al., 2003). Based on COSPEC data collected during 1980-1993, Allard et al. (1994) obtained an average SO_2 flux during quiescent periods that varied between 300 and 1200 t/d, depending on the intensity of activity, with an SO_2 flux of 800 t/d during moderate activity. During explosive events, the flux

reaches values of 430-1640 t/d (Allard et al., 1994). In good agreement with flux-based heat estimation, these measurements require degassing of magma at a rate of 790-1580 kg/s or 0.3-0.6 m^3/s (Allard et al., 1994). This requires that 0.01-0.02 km^3/year of magma be degassed, of which only ~ 7 x 10^{-5} km^3/year have erupted (Allard et al., 1994; Harris and Stevenson, 1997b). This leads to an imbalance, whereby the erupted magma is less than the degassed one. Taking ~ 1500 years of activity into account, this un-erupted volume is substantial: 15-30 km^3. In conclusion, it is thought that Stromboli stores most of its degassed mass either inside or, more likely, below its volcanic building, at a fairly slow rate of ~ 6 kg/s, of which only a small portion is erupted at the surface (Allard et al., 1994; Francis et al., 1993; Harris and Stevenson, 1997b). After then, and during 2002-2003 and 2007 eruptions, SO_2 fluxes were measured by mini-DOAS spectrometers (Galle et al., 2003) and varied within the same range indicated for the past (e.g., Burton et al., 2009).

2.2.2 Application of UV cameras to volcanic degassing

More recently, UV cameras have been increasingly used in Volcanology to image SO_2 flux emissions at high spatial and temporal resolution (Burton et al., 2015a). The principles of the technique are fully described in Chapter 3.

The main application of the UV camera to explosive basaltic eruptions, has been to Strombolian activity due to issues with ash making gas remote sensing impossible in other classes of explosion, whose eruption plumes are more ash rich (Tamburello, 2011a). Dalton et al. (2010) used a ≈ 4 s resolution dataset to quantify the amount of gas released during a single Strombolian eruption in combination with infrasonic data. This built on earlier work by Vergniolle and Brandeis (1996) and Vergniolle et al. (1996) who developed a method for assessing gas release using infrasonic measurements. Mori and Burton (2009) focused their UV camera measurements to estimate SO_2 gas mass from single Strombolian eruptions at Stromboli (15–40 kg). Basing on five discrete explosive events occurred in one day, the authors demonstrated that in terms of gas flux Strombolian explosions are a second-order phenomenon compared with quiescent degassing. Furthermore, they found that the acoustic method under-estimates the size of gas mass.

Gas mass is an important feature in understanding degassing. It can unlock details about the exsolution source depth and potentially reveal information regarding the shallow plumbing system beneath volcanoes, particularly when using a multi-dataset approach. In general, there has been a lot of work into the mechanisms and the processes affecting the explosive aspects of basaltic volcanism. However, a very recent finding concerning passive degassing, which is discussed in Tamburello et al. (2013), Pering et al. (2014a) and Chapter 4 and 5 of this work, highlights the great importance of

this rather less spectacular degassing style. Tamburello et al. (2013) and Pering et al. (2014a) proposed that a periodic SO_2 degassing activity, which is observed on timescales of 40-250 s at the North-East crater of Mt. Etna, is caused by waves of bubbles rising within the conduit and bursting at the surface producing the oscillating flux signal captured with the UV camera. This short-period degassing is referred to as "puffing" in the literature. Tamburello et al. (2013) also noted the presence of a longer period >2000 s flux modulation, however, they did not explore this feature further due to the relatively short duration of their dataset. In addition, a 2000 s degassing cyclicity is mentioned in Nadeau et al. (2011). These authors proposed that the short-term variation is likely caused by waves of bubbles rising in the conduit, in line with an earlier model detailed in Manga (1996), and further suggested that the cause may be related to time-dependent changes in bubble size and magmatic vesicularity. The process is likely limited to the upper 1 km of the conduit due to the lack of correlation with the seismic signal, which is generated at greater depth. Peters et al. (2014a), Girona et al. (2015) and Ilanko et al. (2015a, 2015b), have all identified a periodic structure to degassing at Erebus over a ≈ 10 min window in SO_2, H_2O and gas ratios. This cyclic degassing process therefore warrants further research. Aiuppa et al. (2007) further signify the importance of studying passive degassing as it may prove useful in eruption forecasting.

Developments such as these have come about because of the high temporal resolution capabilities of the UV camera. SO_2 flux data can now reveal aspects of basaltic degassing in much more detail than possible hitherto. Due to the low time resolution of collected SO_2 data in the past, it had remained incomparable to seismic data. However, as sampling frequencies approached 1 Hz and faster, it became possible to compare SO_2 flux data to similarly high resolution seismic and infrasonic data (Ripepe et al., 2005; McGonigle et al. 2009; Dalton et al., 2010; Kazahaya et al., 2011; Tamburello et al., 2012; Waite et al., 2013; Nadeau et al., 2015; Delle Donne et al., 2016, 2017), and deformation (Saballos et al., 2014; Watson et al., 2000). There are several such examples of such work including Nadeau et al. (2011) at Fuego Volcano (Guatemala), who observed a correlation between SO_2 emission rates and volcanic tremor, indicating that the generation of the seismic tremor and the rise and fall of SO_2 flux rates originate from the same source process. This work (see Chapter 6) confirmed the long-held belief that there is a link between a rising gas slug and tremor as is discussed in Chouet et al. (2003). However, the mechanism is still highly unconstrained and Nadeau et al. (2011) conjecture that it could be caused by the oscillation of bubbles, a resonance in the conduit, the movement of the magma or the coalescence of bubbles. The high temporal resolution ability of the UV cameras allow the measurement of much more rapid Strombolian, on the order of seconds, a goal which has yet to be achieved.

Due to its ease of access and frequent eruptions, Stromboli has been a preferred target of study with the UV camera. A study by Tamburello et al. (2012) produced an in depth summary of both passive and active forms of degassing at Stromboli. The authors managed to extract the slug size and relate the size of the VLP (Very-Long Period) seismic signal to the amount of SO_2 released during an explosive eruption, similarly to McGonigle et al. (2009). This was key as it allowed the corroboration of the analysis by Chouet et al. (2003) which revealed that the source depth of tremor is at 300 m. However, the analysis by Tamburello et al. (2012) did more to highlight the small amount that explosive processes contribute to the daily SO_2 budget at Stromboli, a mere ≈ 7%. In total, active degassing (explosive events and puffing) was calculated to contribute ≈ 23% of SO_2 and passive ≈ 77% (Figure 2.7). This highlights the importance of further study into passive degassing and modeling of these processes.

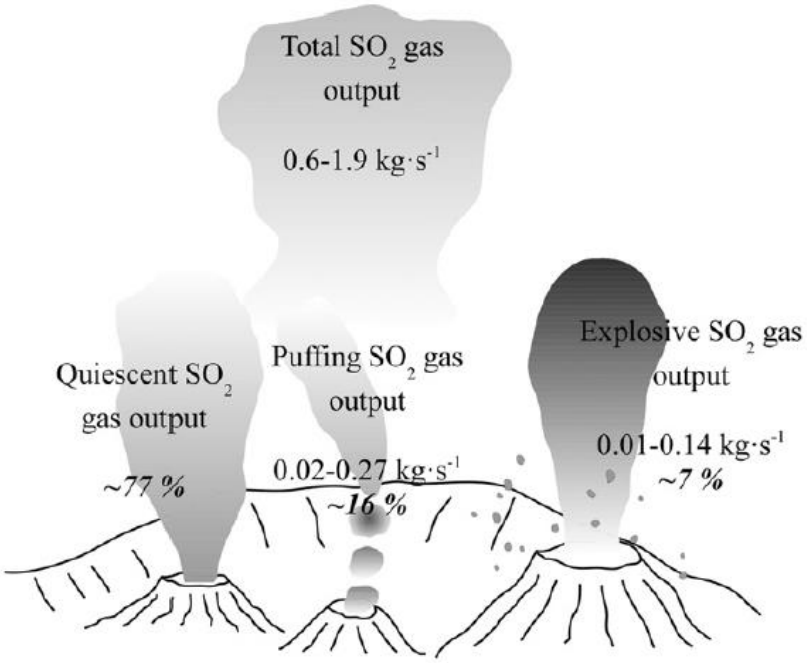

Figure 2.7 *Sketch diagram summarizing the relative contribution of passive and active (from Tamburello et al., 2012).*

Indeed, because Stromboli possesses such reliable activity it is an ideal location to monitor and collect a large number of observations of Strombolian activity.

The UV camera has also be used to investigate degassing of more viscous magmas such as those at Santiaguito volcano (Guatemala), where a rheologically stiff lava dome is in place. Holland et al. (2011) used the camera to investigate degassing processes during the extrusion of the dome which has occurred since 1922. The high time resolution SO_2 flux data allowed a full assessment of the mode of degassing, which would have been difficult with previous methods. This work highlights the

utility and adaptability of the camera to a variety of situations and further illustrates that volatiles are important in all varieties of volcanic settings.

2.2.3 SO_2 monitoring networks on Stromboli

SO_2 fluxes measured by mini-DOAS spectrometers (e.g., Burton et al., 2009) already prompted the installation of a permanent network of automatic scanning ultraviolet spectrometers (Burton et al., 2004). The development of these networks (Edmonds et al., 2003a; Burton et al., 2009; Salerno et al., 2009a; Galle et al., 2010) greatly improved the capacity of volcano observatories to perform SO_2 flux monitoring..

After the 2002/03 eruption of Stromboli, a network of scanning ultraviolet spectrometers was installed on the island, with the objective of automatically measuring SO_2 fluxes from the summit craters. The FLux Automatic MEasurement (FLAME) network (Burton et al., 2004; Salerno et al., 2009a) has been operational since 2004. The network consists of four ultraviolet scanning spectrometers (Ocean Optics S2000) placed near the coast of the island and intercepting the plume from a distance of ~2000 m for the summit craters of Stromboli . A single scan takes from 5 to 15 min depending on the integration time for each spectrum, which varies due to the intensity of scattered skylight. A control program running on a remote PC directly commands each scanner to alternately move the motor and then collect a spectrum. Each measurement from a scanner consists of one dark spectrum, collected when viewing downwards, followed by a user-defined number of spectra collected between a user-defined angle range. An analysis system uses an artificial clear sky spectrum to avoid any issues resulting from the plume occupying a wide part of the scan arc, and no clear sky spectra are available (Salerno et al., 2009b). FLAME automatically computes the SO_2 mass emission rate in real-time. Data are transferred using a wifi network on the island. Details and configuration of the network are described in Burton et al., 2009. Data reduction to SO_2 slant column amounts was performed using a custom-written program that utilized an artificial reference spectrum rather than a measured reference spectrum. The main advantage of using an artificial reference spectrum is that retrieved SO_2 amounts are in absolute units, even if the entire arc of sky visible to the instrument contains volcanic gas; a fairly common occurrence on Stromboli. Scans are converted in real-time to SO_2 slant column amounts, before being passed to a flux calculation program. On Stromboli, unfortunately, stable wind directions are a rarity. Relatively large errors on the flux determinations of 30–50% result from uncertainties in wind velocity over the FLAME station (Burton et al., 2015). Furthermore, short term phenomena produced by explosion degassing would be lost and not be revealed because the relatively slowly scanning.

Burton et al. (2009) measured the SO_2 fluxes emitted by Stromboli during the 27th February–2nd April 2007 effusive eruption using both by FLAME automatic network of scanning ultraviolet spectrometers and by traverse measurements conducted by boat and helicopter. During the eruption, the SO_2 flux was highly elevated, averaging 700 t/d, about four times normal degassing rates (~150 t/d). The authors propose that the observed deflation (Bonaccorso et al., 2008) was a response to a larger exiting magma flux from the intermediate reservoir compared with that entering the reservoir from below. Considering the lower SO_2 flux and the higher effusion rate of 2002-2003 Stromboli eruption compared with 2007, authors speculated that in Stromboli low effusion rate eruptions can take place longer durations than high effusion rate eruptions. Finally, they propose that the decrease in SO_2 flux on 15th March prior to the paroxysm was an indicator of the collapse of the permeable network, that produced gas-rich pockets of magma at depth that could then coalesce and produce fast rising gas slugs, leading to the explosion.

In May 2013 a permanent SO_2 camera system was installed by INGV-Catania, in order to complement monitoring of SO_2 flux emissions provided by the FLAME network, and in particular to better track the flux of gas associated with explosive activity. Burton et al. (2015) showed that in favorable conditions, i.e. when the plume is blown into the field of view of the camera, measured SO_2 fluxes agree well with those measured with the FLAME network.

One of the main challenges of the SO_2 camera is the robust and automatic imagery analysis. Only the recent permanent UV camera network, installed and run by Università di Palermo, based on a longer data set allows a more statistically robust fully automated analysis in Etna and Stromboli volcanoes (D'Aleo et al., 2016, 2019; Delle Donne et al., 2017). This networks answers to the key requirement for volcano observatories, in order for the data from the SO_2 camera to be used in a real-time monitoring capacity. Stromboli network is composed by two cameras, operative since June 2014 (UV1) and May 2017 (UV7), that are both located ~500 m away from Stromboli active vents and allow imagining the crater plume(s) from different viewing directions (Figure 3.1 and 5.1).

UV cameras exhibit larger spatial resolution than traditional (UV scanning spectrometer) UV remote sensing techniques. The high temporal (0.5 Hz) and spatial resolution of the camera makes it capable of capturing the explosion SO_2 flux emissions from Stromboli craters allowing also the correlation with seismic very long period, thermal, and infrasonic activity. Delle Donne et al. (2017) reported unprecedented long and continuous SO_2 flux record obtained using a permanent UV camera system and designed a novel methodology to quantify the SO_2 flux contributions and to identify variations of individual source's emission strength over time. Results obtained demonstrate that permanent UV camera networks can valuably contribute to monitoring volcano dynamics. Specifically, the authors characterized volcanic SO_2 flux regime in the period prior, during, and after Stromboli's August –

November 2014 effusive eruption. Understanding the mechanisms that cause effusive eruptions is the key to mitigating their associated hazard.

In conclusion, the use of the UV camera, to measure volcanic gases, in recent years has laid the foundations, not only for estimating SO_2 fluxes, but also for understanding the dynamics of degassing of magma and the role of volatiles in explosive dynamics. The combined ability to measure gas emissions, released degassing (puffing and Strombolian explosions) to the total SO_2 budget quickly and from different sources, allows the UV camera to distinguish and quantify the gas fluxes resulting from different styles of volcanic activity. This opens up the possibility for new insights relating to magmatic dynamics, such as the relative proportion of gas released during quiescent degassing compared to that released in explosions. Differences that reflect the degree of coupling between gas and melt.

The high temporal and spatial resolution (Smekens et al., 2015) combined with automatic processing permits to 'live' monitoring (Aiuppa et al., 2018) degassing activity, thus contributing to understanding (and potentially predicting) changes in volcanic activity style and offering novel insights into the degassing dynamics within the shallow conduit systems. This makes UV camera technique an important tool for volcanic monitoring. UV cameras are now at the stage where they can be used to begin to answer scientific questions concerning explosive and passive gas release. It is hoped that this thesis goes some way to demonstrating this.

–Chapter 3 –

Methods

3.1 UV Camera network

The SO_2 flux results discussed in this Ph.D. thesis are obtained from a permanent, fully autonomous UV camera network designed within the framework of the project BRIDGE (http://www.bridge.unipa.it/) funded by the European Research Council. Stromboli's current activity takes place within a NE–SW elongated crater terrace composed of three main vent areas (named northeast (NEC), southwest (SW) and central craters (CC)). The terrace is located at an elevation of ~750 m a.s.l. on the upper margin of the Sciara del Fuoco (SdF). Given of the geometry of the crater terrace described above, to separately resolve SO_2 flux emissions from NEC and central-southwestern (SWCC) sectors (see Chapter 5), we used an ad-hoc designed network of two stand-alone, permanent UV cameras, located at respectively Roccette (38°47'54" N, 15°12'56" E; NE upper flank of Stromboli, at 677 m a.s.l.; UV1 in Figure 3.1) and Valle della Luna (38°47'28" N, 15°12' 25" E; SW upper flank of Stromboli, at 750 m above sea level; UV7 in Figure 3.1). The two cameras, operative since June 2014 and May 2017 respectively, are both located ~500 m away from the active vents, but allow imagining the crater plume(s) from different viewing directions (Figure 5.1). UV1 camera system transfers data in real-time from the instrument module to the acquisition/processing module using a WiFi radio (see Section 3.3). The latter is remotely installed at the local volcano observatory to minimize power consumption at the remote site and ensures full operation during winter time, when bad weather conditions and reduced sunlight decrease performance of solar panels. UV7 camera system thanks to a mini-PC routine processes data automatically on board without transmission of raw data. These, saved on two HD inside the system, is taken periodically during field campaigns. Processed data transmission between instrumental and acquisition/processing modules occurs via wireless Transmission Control Protocol/Internet Protocol connection (TCP/IP).

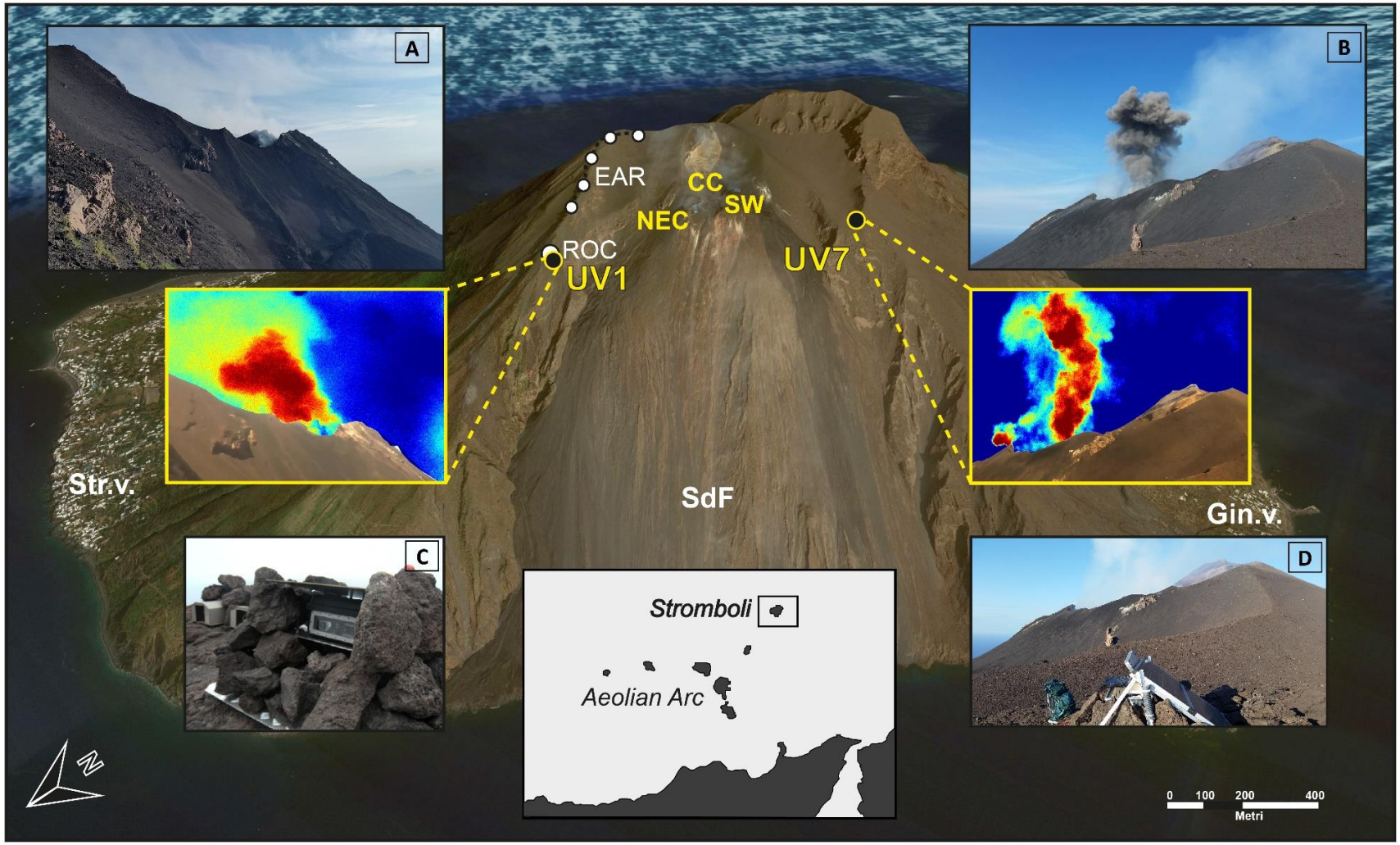

Figure 3.1. *3D view of Stromboli volcano from Google Earth showing the Roccette site (ROC+UV1) and Valle della Luna site (UV7) and where the UV camera network and the seismic station ROC are located, including field of view of crater areas (NEC, north-eastern crater; CC, central craters; SW, south-western craters), the position of the five-elements infrasonic array used for acoustic location of volcanic activity (EAR). UV1 and UV7 visible cameras (**figs. A-B)** and, UV instrumental details (**figs. C-D**). (Str. v.: Stromboli village; Gin. v.: Ginostra village; SdF: Sciara del Fuoco).*

3.2 UV camera Basic theory

The technique was first employed by Mori and Burton (2006) and Bluth et al. (2007) and has since been frequently used by others to determine the SO_2 flux. There are two main techniques for determining SO_2 flux based on these units. The first technique, which is recommended by Kantzas et al. (2010), uses two images from parallel mounted UV cameras (or by some authors, a single camera with rotating filters) and compares the images on a pixel by pixel basis. The cameras are fitted with bandpass filters, which permit transit of light at 310 nm and 330 nm, respectively, where SO_2 in the plume absorbs/does not absorb scattered skylight (Figure 3.2). This technique allows a very high time resolution, potentially at ≈ 0.5 s (≈ 4 s when a single camera is used (Mori and Burton, 2006)) and uses the following equation to calculate SO_2 absorbance:

$$A = -\log_{10}\left[\frac{\left(\frac{IP_\alpha}{IB_\alpha}\right)}{\left(\frac{IP_\beta}{IB_\beta}\right)}\right] \qquad \text{(Eq. 1)}$$

where IP is the image of the plume and IB is the background image, α refers to the filter which detects SO_2 absorption (310 nm) and β refers to the filter which does not (330 nm). It is important to note here that SO_2 absorption occurs in a window between 260-320 nm (Vandaele et al. 1994). The filters are usually centred between 300-320 nm for the absorption of SO_2 and 320-340 nm outside the absorption band. A final SO_2 concentration is achieved by calibrating the instruments prior to or during acquisition against cells of known SO_2 concentration (Kantzas et al. 2010; Tamburello, 2011a) (Figure 3.3). Calibration using a co-aligned DOAS instrument is preferred by some researchers (Kern et al. 2010a; 2010b). Use of these two filters method allows compensating for aerosol attenuation/backscattering while minimizing temporal mismatches associated with filter changes on a single camera (Bluth et al., 2007) and raising temporal resolution at up to 0.5 Hz or more (Kantzas et al., 2010).

Alternatively, the second method is based upon the use of a single filter, solely in the SO_2 absorption band (Bluth et al. 2007). This does not allow for resolution between the attenuation of gas and the attenuation of aerosols, which also absorb in the ultraviolet (Kantzas 2010; Tamburello, 2011a). The equation for determining SO_2 concentrations can be simplified as:

$$A = -\log_{10}\left(\frac{IP_\alpha}{IB_\alpha}\right) \qquad \text{(Eq. 2)}$$

omitting a direct comparison to a background image. However, whilst this is an intrinsically simpler approach, ignoring the aerosol absorption could, in practice, create larger errors.

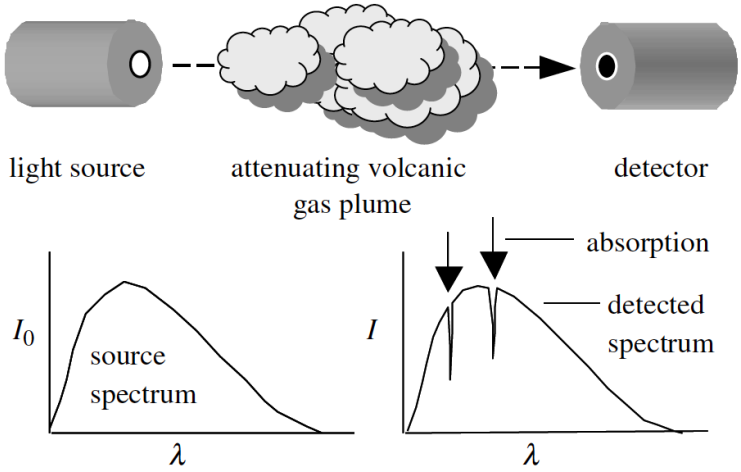

Figure 3.2 *Transmission of radiation (in this case from an artificial lamp) through a volcanic plume, before detection by a spectrometer. The emitted source spectrum $I_0(\lambda)$ and the measured spectrum $I(\lambda)$ differ depending upon the composition of absorbing species in the plume (McGonigle et al., 2005a).*

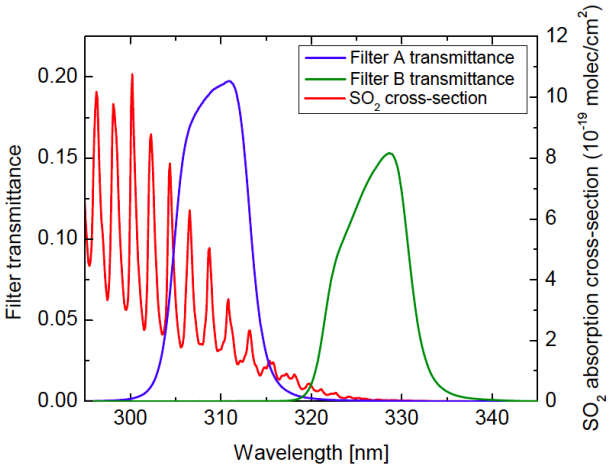

Figure 3.3 *The transmittance spectra of the two band-pass filters at a wavelength of 300 and 320 nm (from Kern et al., 2010).*

Despite the increasing popularity of this camera, there are still several challenges faced when using this approach. For instance, achieving an ideal location for acquisition can be difficult due to the location of the sun and the 'vignetting' issues that this results in: e.g., due to inhomogeneous solar illumination of the background sky (Kantzas et al. 2010). The light-dilution effect, with some recent attempts at quantification (Campion et al. 2015), where light intensity is effectively reduced by scattering amongst other light-paths can also induce large errors. In addition, climatic conditions can also play a part: if the plume is not visible due to fog or cloud cover, then the acquisition cannot be completed successfully. For a detailed discussion on the UV camera technique please see Kantzas et

al. (2010). In addition, Tamburello et al. (2011b) have devised a user-friendly program, Vulcamera, which enables the use of the two-camera two-filter set-up in the field with relative ease and subsequent processing SO_2 flux data. Recent advent of a permanent UV camera network at Etna e Stromboli, run by Università di Palermo, is paving the way to automatic processing in real-time allowing to measure a robust (with no interruption) dataset (D'Aleo et al., 2016, 2019; Delle Donne et al., 2017; Delle Donne et al., 2019).

3.3. Hardware

The fully autonomous UV camera system, described in Delle Donne et al. (2019), is conceived to grant high-rate (0.5 Hz) long-term SO_2 flux observations in continuous mode. Similar automated permanent networks of UV camera system prototypes are described in Kern et al. (2015) and Burton et al. (2015b). UV1 camera system is composed of (i) an instrumental module and (ii) an acquisition/processing module. The instrumental module is equipped with two JAI CM-140GE-UV cameras, sensible to UV radiation, and one Ocean-Optics USB2000+ Spectrometer (same as in Delle Donne et al. (2017)). Two different band-pass optical filters, with Full Width at Half Maximum (FWHM) of 10 nm and central wavelengths of 310 and 330 nm, respectively, are applied to the cameras to enhance differential UV absorption in the SO_2 bandwidth (Kantzas et al., 2010; Kern et al., 2010; Burton et al., 2015a) (Figure 3.3). Images (at 520 × 676 pixels and 10 bit resolution) are acquired with a frame rate of 0.5 Hz. Use of the UV spectrometer allows full UV spectra to be derived, which are processed by Differential Optical Absorption Spectroscopy (Platt and Stutz, 2008) fitting the theoretical SO_2 absorption cross section of Vandaele et al. (1994). Spectra are acquired every 5 s. The Ocean-Optic USB2000+ Spectrometer in use mounts a Sony ILX511B Linear Silicon CCD Array Detector at 2048 pixels, with a Wavelength Response of 200-1100 nm, a dynamic range of 8.5 × 108, and a signal-to-noise ratio of 250:1 at full signal.

The spectrometer is coupled to a telescope of rectangular, vertically oriented, field of view (FOV " 0.3° × 14°), and spatially filtered to match the "12° vertical width (same as in Delle Donne et al. (2017, 2019)). Column densities over the entire images are then obtained by integrating images achieved by the UV camera with information achieved by the spectrometer. The instrument module is powered with 12 V batteries and solar panels and requires a power of 15 W in fully operational mode (Figure 3.4). UV1 camera system transfers data in real-time from the instrument module to the acquisition/processing module using a WiFi radio to local volcano observatory. The presence of a mini-ITX PC (Jetway N2600), connected to the instrument module, allows to UV7 camera to acquire and process data automatically (e.g., without the need of the operator) (Figure 3.4).

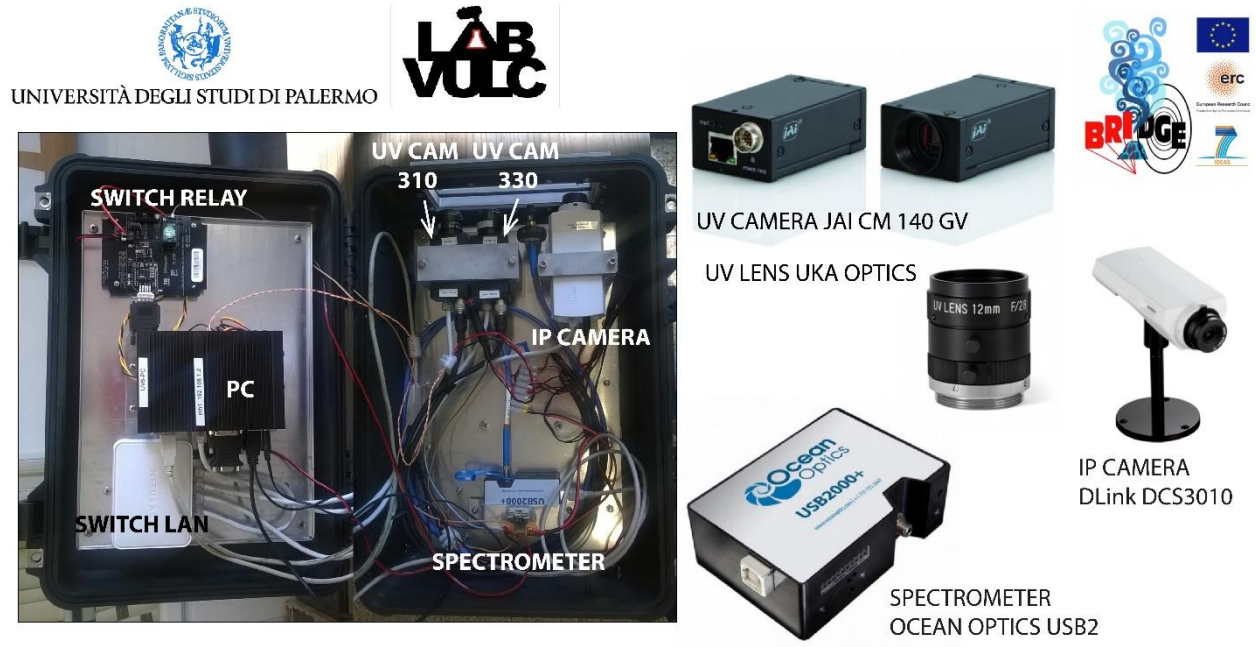

Figure 3.4 *UV camera is composed of two JAI CM-140 GE-UV cameras (29 × 44 × 75 mm) equipped with UV lens UKA Optics, an RS232-Ethernet MOXA converter, an Ocean Optics USB 2000+ spectrometer linked to an optical fiber (600 micron, 2 m), an VIS collimator, an IP camera Dlink DCS3010, a switch relay and a switch lan and a mini-ITX PC (these three latter components are present only in UV7 camera).*

The acquisition/processing module consists of an integrated data logging and image processing system specifically designed to gather the signal output from all hardware automatically and synchronously.

In order to control acquisition, processing parameters (including automatic tuning of exposure times of UV cameras and spectrometer) and automatic evaluation of optimal viewing condition are designed specific algorithms. Data transmission between instrumental and acquisition/processing modules occurs via wired or wireless TCP/IP, respectively for UV1 and UV7.

3.4. Acquisition and data processing

3.4.1. Derivation of SO_2 Column Densities

Processing of UV camera images allows quantifying relative absorption of UV radiation by SO_2 via the Beer-Lambert law (equ. 1). At this aim, sets of two images, synchronously acquired by the two cameras (mounting filters at 310 nm and 330 nm, respectively), are combined to obtain a single absorbance image (Mori and Burton, 2006; Kantzas et al., 2010). Absorbance is obtained from

$$A = -\log_{10}\frac{I^{310}}{I^{330}} - A_0$$

where A is absorbance, I310 and I330 are pixel intensities associated with cameras mounting the 310 or 330 nm filter (after normalization for exposure times), while A_0 is the absorbance level associated with a clear background sky subarea of the image (unaffected by SO_2 absorption). The background sky subarea is automatically selected for each image by the processing module (Figure 12).

Using data streamed from the co-located ultraviolet spectrometer, absorbance images are converted into SO_2 column density images (Figures 3.5 and 13a). The spectrometer points a known subarea within the camera field of view using the proportionality ratio between absorbance and SO_2 concentrations in a determinated region of the image, using the methodology described in McGonigle (2007). For calibration of UV camera images, see also Lübcke et al. (2013).

3.4.2 Plume Transport Speed

An accurate evaluation of the plume speed field is mandatory for robust SO_2 flux measurements (McGonigle et al., 2005; Williams-Jones et al., 2006; Johansson et al., 2009; Oppenheimer et al., 2010, 2011). In recent years it has been widely demonstrated that errors in plume transport speed contribute up to 40% of the total error in derived fluxes (Bluth et al., 2007; Burton et al., 2015a), especially where are assumed equal to wind velocity or when are obtained from atmospheric transport models. UV camera technology allows a real-time tracking of the moving gas plume upon its exiting from the vents (Peters et al., 2015). Hence, plume transport speed can directly be measured using UV camera. This minimizes errors in SO_2 flux time series. UV1 and UV7 camera system derives the plume velocity profile over the crater terrace (Figures 3.5 a and 3.5 b) by applying the Lucas and Kanade (1981) optical flow algorithm to sets of successive UV camera images. Specifically, absorbance images of UV camera contain gas-rich and ash-free portions of the plume that have higher absorbance relative to the background and/or ash-rich plume segments.

Lucas-Kanade subroutine, integrated in the acquisition/processing module, takes advantage of these characteristics to track gas moving fronts in consecutive frames and then to quantify plume transport speed at 0.5 Hz. Delle Donne et al. (2017) tested performance of this method by using artificial images with known particle velocities and obtained errors in estimated velocities of <5%.

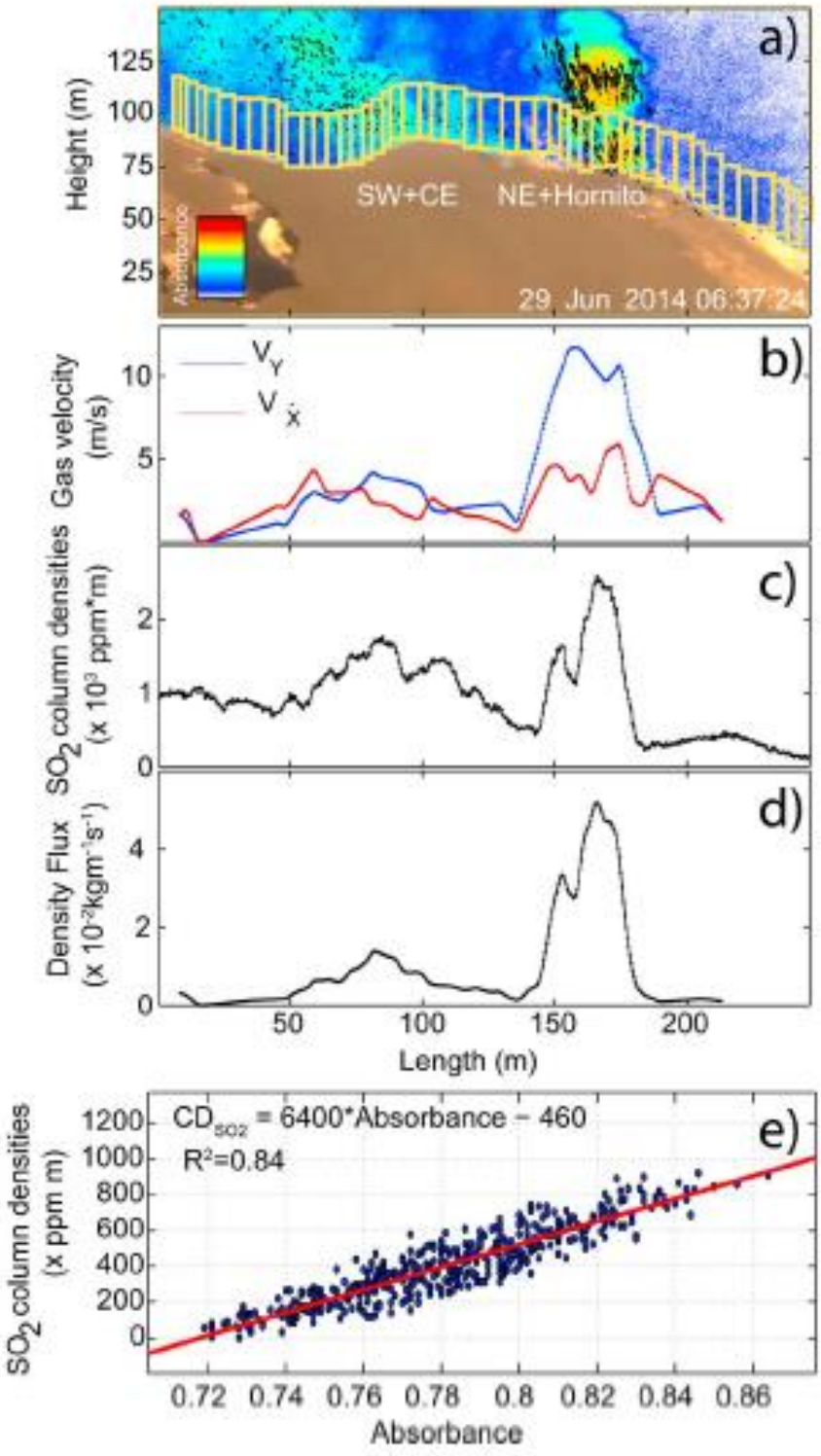

Figure 3.5 *(**a**) SO_2 column densities calculated on a 250 × 130 m area image encompassing the NE crater terrace (from UV1 camera). Gas velocity vectors, indicated with black arrows, arecalculated on high coherence regions of the images. (**b**) Gas velocities and (**c**) SO_2 column density distributions are calculated within the yellow boxes, in order to derive the (**d**) SO_2 density flux distribution along the entire crater area. SO_2 total flux for a given sector is then calculated by integrating the density flux over the total length of the image. (**e**) An example of calibration curve using co-located UV-scanning spectrometer allows to convert uncalibrated absorbance intensities into SO_2 column densities (from Delle Donne et al., 2017).*

3.4.3 Automatic Determination of Optimal Viewing Condition

Optimal viewing conditions of the plume and the presence of a clear sky are required for a reliable SO_2 flux measurements. However, weather conditions are extremely variable on Stromboli's summit and often prevent SO_2 observations. We then performed an algorithm aimed to recognize that images within the dataset have the requirements for a reliable SO_2 measurement through a calculation of two visibility indexes [Delle Donne et al. (2017)]. The first visibility index (Fog index) is obtained from the ratio between the mean pixel intensity in portions of the camera's FOV capturing (i) the sky and (ii) the ground (Figure 3.6a).

We tested that this ratio is sensitive to good visibility conditions. In particular, only images having visibility index higher than four (4), (i.e. pixel intensity associated with sky areas is 4 times higher than the intensity associated with ground area) are taken into account for SO_2 measurements.

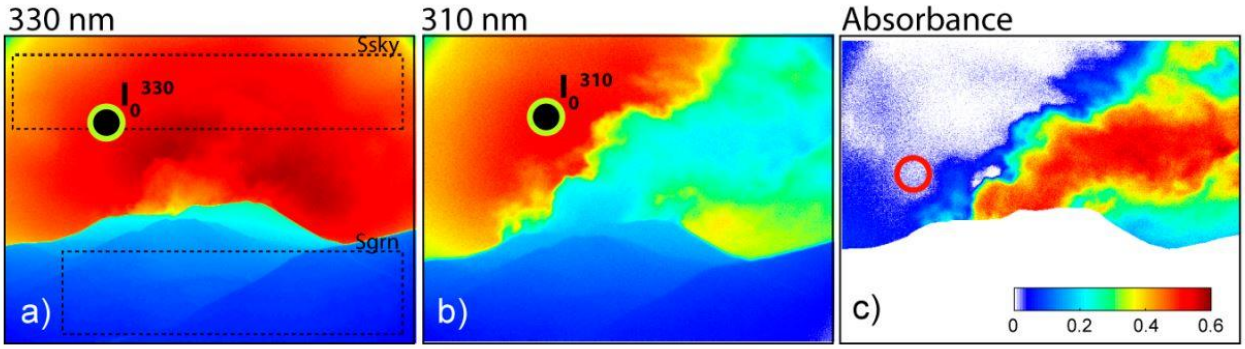

Figure 3.6 *Black rectangles (Ssky Sgrn) in* ***(a)*** *represent the areas used for calculation of the visibility index. Black circles in* ***(a)*** *and* ***(b)*** *represent the sky areas where absorbance is assumed to be SO_2 free.* ***c)*** *Absorbance image is obtained applying the Lambert-Beer equation after image normalization respect to background absorbance intensities. The red circle in* ***(c)*** *shows the FOV of co-located UV-scanning spectrometer used to convert un-calibrated absorbance intensities into SO_2 column densities.*

The detection of a "sky" signal well above the "ground" signal is required especially in presence of a highly condensed plume that can affect the SO_2 absorbance signal. In order to encompass this, the second visibility index allows us to select only images with a clear SO_2 signal above atmospheric noise combining absorbance and 310 nm images associated with the plume. An high enough SO_2 signal above the atmospheric noise is required for a reliable SO_2 measurement. A correlation index (Corr $_{IDX}$) between absorbance and 310-nm pixel intensities over a cross-section intersecting the plume able to distinguish this condition in real-time has been defined as the sub-routine designed for UV camera measuring Etna volcano plume (Figure 3.7b) (Delle Donne et al., 2019). Specifically, the correlation index is defined as

$$Corr_{IDX} = \sqrt{\left(\frac{Cov(i,j)}{Var(i,i) * Var(j,j)}\right)}$$

where Cov is the covariance matrix, i and j are pixel intensities over the cross-section of absorbance and 310-nm images, respectively. When the correlation index value is closer -1 means that the absorbance is more related to gas. Images having a Corr $_{IDX}$ < -0.5 are excluded by automatic calculation (Figure 3.8a).Images that do not satisfy this condition (e.g., that have a Correlation Index < -0.5) are discarded by the automatic computation (Figure 3.8b).

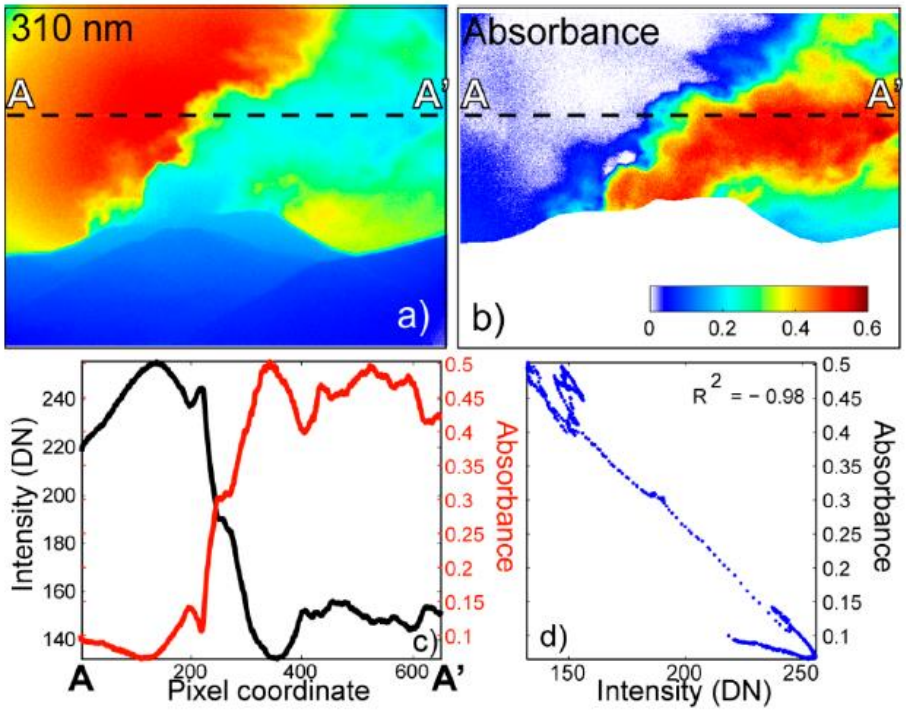

Figure 3.7 *The image quality calculation method using the correlation coefficient between the 310 nm filter image (**a**) and the corresponding absorbance image (**b**) applied on UV camera measurements of Mt. Etna volcano plume. An intensity profile associated with a section (dashed line) crossing the volcanic plume, for both the 310-nm filter and absorbance images, is obtained (**c**). Gas is visible within the plume if these profiles are negatively correlated with a high correlation coefficient (**d**) (from Delle Donne et al., 2019).*

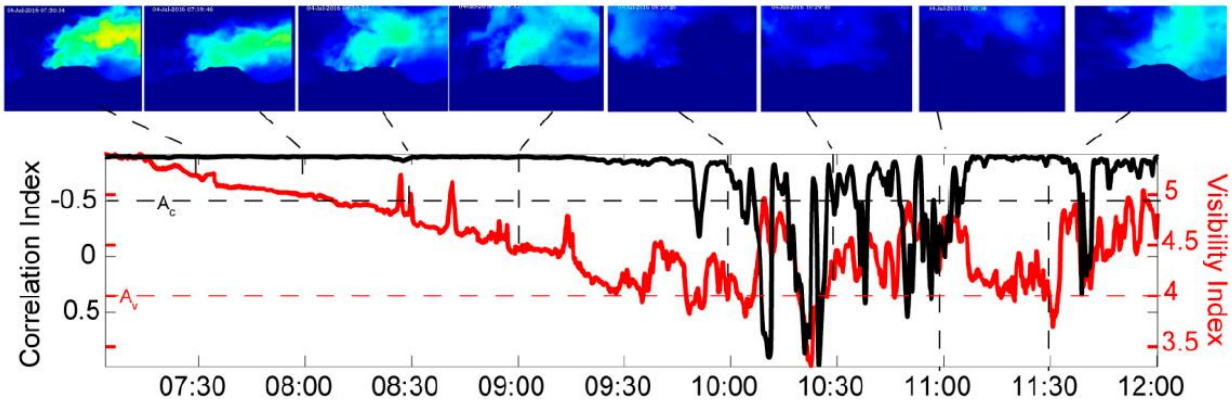

Figure 3.8 *Example of output of the quality indexes sub-routine on UV camera measurements of Mt. Etna volcano plume. The visibility (fog) and correlation indexes fluctuate through time as visibility conditions change (see snapshots on top of the figure). Gas is visible only when the fog index is greater than 4 and the correlation index is less than -0.5 (from Delle Donne et al., 2019).*

3.4.4 Automatic SO_2 Flux Measurements From UV Camera Images

SO_2 flux time series obtained from calibration and processing of UV camera images (Figure 3.5a) by the acquisition/processing module aforementioned. Image processing is conducted on a restricted image portion, capturing a sub-region located just above the crater rim (Figure 3.5). This minimizes atmospheric effects, such as air entrainment in the plume and complexities in the local wind field. Hence, in these near-vent image portions, the SO_2 absorption signal is maximized relative to the atmospheric background (Figure 3.5 a). The "near-vent" calculations are looked at measuring plume velocities more directly related to degassing internal dynamics, in order to better highlight changes in the volcano's regime (Figure 3.5 a).

A series of rectangular regions over the crater terrace are selected (Figure 3.5 a) and calculate time series of the plume velocity field (Figure 3.5 b) and SO_2 column density (Figure 3.5 c) inside each of these regions (delle Donne et al., 2017). From this, profiles of plume speed (Figure 3.5 b) and SO_2 column density (Figure 3.5 c) along a crater terrace transect are obtained. Plume speed is calculated by applying the Lucas and Kanade (1981) optical flow algorithm to sets of consecutive UV camera images. This implies an automatic selection of high intensity (i.e., high SO_2 column density) pixels within the plume showing high spatial coherence in consecutive frames. Plume speed profiles, in both horizontal and vertical directions of movement (Figure 3.5 b), are derived by averaging (in each rectangular region) the calculated two-dimensional velocity field and filtering out velocity points with low coherence. Standard deviation associated with the population of velocity vectors calculated within each monitored rectangular region at each time (2 s) are calculated to quantify plume speed

uncertainty along the profile (Figure 5.3a). This procedure is based on the idea that a highly coherent plume front will be characterized by consistent velocity vectors (resulting in low standard deviation), while a low coherent front will be characterized by more heterogeneous velocity population (and, thus, higher standard deviation).

A SO_2 flux density profile (in kg m^{-1} s^{-1}) is then obtained from combination of plume speed and SO_2 column density profiles (Figure 3.5 d). This SO_2 flux density profile is calculated along an ideal section linking the centers of the rectangles of Figure 3.5 a and by multiplying SO_2 column density profile by the normal component of the velocity profile (relative to this ideal section). Finally, the SO_2 flux for a desired portion of the profile is determined by 1-D integration over that desired portion. The total SO_2 flux is finally obtained by summation over all the integration cells (column densities) showing high spatial coherence in consecutive frames.

The SO_2 flux density profiles (in kg m^{-1} s^{-1}) are also used to locate the sectors, within the crater terrace, that mainly contribute to the total SO_2 flux (Figure 13a). Operatively, this can be achieved by peaking maxima in SO_2 flux density profile (Figure 13d). This procedure allows us to discriminate degassing among different vents and then to spatially resolve on a single vent degassing activity through time.

3.4.5 Picking Active SO_2 Degassing

High-rate SO_2 flux time series at Stromboli typically shows sudden and short-lived gas flux pulses that are overimposed over a rather constant background signal (McGonigle et al., 2009; Tamburello et al., 2012; Pering et al., 2016; Delle Donne et al., 2017). The largest SO_2 flux pulses correspond to the rapid ascent, within the camera field of view (FOV), of over-pressured gas jets released by Strombolian explosions (Tamburello et al., 2012). A nearly constant gas emission originated from quiescent degassing and an impulsive gas contribution (SO_2 flux pulses) related to explosions and puffing activity (active degassing) contribute to the Stromboli's SO_2 total flux.

To fully characterize these distinct degassing behaviors, we use here the automatic technique of Delle Donne et al. (2017) that identifies (and counts) the SO_2 pulses in the SO_2 flux time series. The peak-finder algorithm is designed to characterize duration and amplitude of every single pulse in the SO_2 flux time series (Figure 3.9). Such pulses can be identified in a time series as local maxima above a fixed threshold, having a fast ramp and a slower waning phase (Figure 3.9) (see also Delle Donne et al., 2017).

In order to resolve pulses with fast ramp (more likely related to gas burst at the magma free surface) from slower ones (related to fluctuation in passive degassing), the peak searching algorithm is

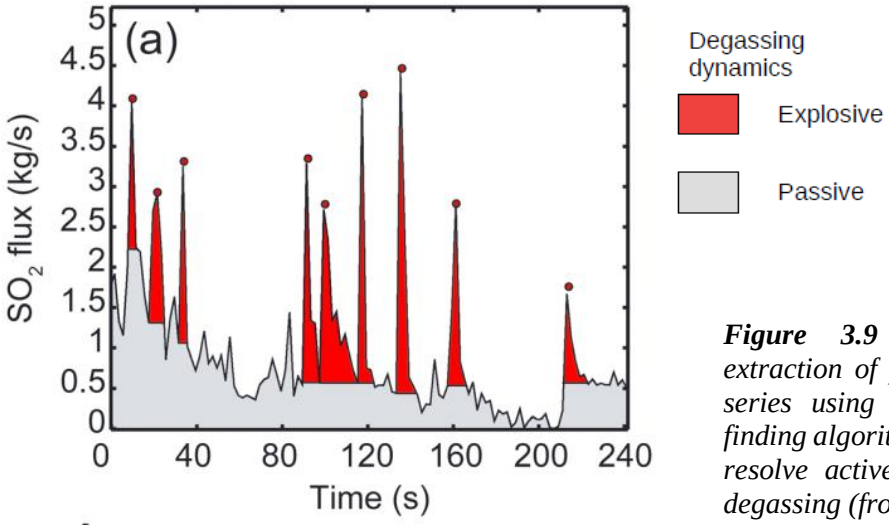

Figure 3.9 *Example of automatic extraction of pulses in the SO_2 flux time series using the calibrated local peak finding algorithm. The algorithm allows to resolve active (red) and passive (gray) degassing (from Delle Donne et al, 2017).*

applied to the first derivative of the SO_2 flux, using a fixed threshold of 2 kg/s^2. Then, amplitude and duration of all pulses are identified. Amplitude is calculated by subtracting, from each peak flux value in the pulse population, the background SO_2 flux value measured just (one sample) before the pulse peak time. Pulse duration is calculated as the time interval from pulse onset to termination (e.g., the time the flux time series returns back to its pre-pulse value). Pulse SO_2 mass is finally calculated by integrating the flux time series over the entire pulse duration.

3.5 VLP Seismicity, Thermal, and Infrasonic Activity

The geophysical network run by the Laboratorio di Geofisica Sperimentale (LGS) of the University of Firenze (UNIFI) provided infrasonic, thermal and seismic data. We compared the SO_2 fluxes with seismic signals registered by ROC station, co-located with the UV1 camera system, runned by the Laboratorio di Geofisica Sperimentale (LGS) of the University of Firenze (UNIFI) (Figure 10). Very Long Period (VLP) seismicity was detected by band-pass filtering the cumulative ground displacement in the 0.03–1 Hz frequency band. VLP signals recorded at ROC station (Figure 10) and evaluated on a daily basis were always clearly visible above the seismic noise, being this station located at very close distance (<1 km) from the inferred position of the VLP source (Chouet et al., 2003). ROC station is equipped with a broadband seismometer Guralp CMG-40 T, 800 V/m/s with an eigen-period of 30 s. The rate of occurrence of VLP signals is evaluated on a daily basis. Thermal

camera is located at ROC (Figure 10) in direct line of sight to the NE craters and at a slant distance of 345 m and thus with field of views of 218x153m. Forward Looking Infrared Radiometer (FLIR) cameras offer a unique view of explosive volcanism by providing an image of calibrated temperatures. Thermal images are recorded with a FLIR-A20 thermal camera. This thermal camera fitted with a 34° x 25° optical lens (9.2 mm), and 0.1°C thermal resolution. The sensor is an un-cooled micro-bolometer focal plane array of 160 x 120 pixels, which is electronically oversampled at 320 x 240 pixels, and sensitive in the 7.5–13 mm spectral range. Thermal images were collected at a frame rate of 50 Hz using Thermacam Researcher® acquisition software by Firewire connection (Delle Donne and Ripepe, 2012).

Furthermore, in Chapter 5 we coupled the UV Camera-based degassing source locations (Figure 3.1) with those resulting from the infrasonic array detections (Figure 3.1) derived from the EAR array (38°79'39'' N; 15°21'74'' E; elevation of ~870 m; Figure 10). Infrasound was recorded using an iTem prs-0100x differential pressure transducer with a sensitivity of 25 mV/Pa at 1 Hz and with a flat frequency response of 0.01–100 Hz at a full scale range of 250 Pa. Infrasound was digitized using a 24 bit Guralp CMG24 Digitizer at 100 Hz.). Infrasound data were processed following the methodology described in Ripepe and Marchetti (2002) to derive amplitude and direction of the provenance of infrasonic coherent wave fronts generated by active degassing dynamics. Thermal images and infrasound were synchronized using the same GPS clock with an accuracy of ~5 ms.

– *Results Chapter 4* –

"UV-Camera based Stromboli's SO_2 flux time-series during 2014-2018"

Abstract

Stromboli volcano is the archetype of Strombolian activity. Convection of ascending gas-rich magma into more degassed magma in the conduit activates the "degassing machine" that relentlessly operates to sustain this persistent explosive activity. This mechanism explains the longevity of Strombolian activity. Most studies are focused on this type of "explosive" gas release, albeit it represents only a minor fraction of the total gas output at Stromboli. Indeed, Stromboli exhibits a wide range of degassing regimes from passive degassing to effusive dynamics. Continuous passive degassing and 'puffing' combined represent the largest fraction of Stromboli's 'bulk degassing'.

No specific work has been devoted so far to studying the implications of UV Camera networks for understanding the Stromboli SO_2 flux behaviour during "regular" Strombolian activity. Here, we endeavor to fill this gap of knowledge by reporting on an unprecedentedly long (~ 4.5 years) UV camera-based SO_2 flux time-series from Stromboli volcano. Our observational period (June 2014–December 2018) not only encompasses the August 2014 effusive eruption, but a period of 4 years of "regular" Strombolian activity. Therefore, we examine data streamed by UV1 camera (installed since June 2014 on the north-eastern flank of Sciara del Fuoco, SdF) to estimate the total (active + passive) SO_2 flux from the North-East Crater (NEC), and to characterize SO_2 flux fluctuations over time. We also set quantitative thresholds discriminating between "regular", "effusive" and "pre-effusive" activity. Our SO_2 flux time-series reported here represent the longest and most continuous SO_2 flux record obtained with regular and automatic UV camera system.

Our results show that, in 4 years of observations of regular activity (2015-2018), the SO_2 flux never exceeded ~180 t/d at UV1, the instrument with the longest acquisition record (from June 2014). We therefore consider a <180 t/d SO_2 flux range as representative of regular activity and use this to set 'threshold-values' associated to periods of low (<70 t/d) and medium (70-177 t/d) degassing. Our 4-year long time-series also shows that higher SO_2 degassing levels have only been reached prior and during the 2014 effusive eruption. We consequently use these effusive phase (EP) records to manually set the thresholds of high (178-250 t/d) and very high (>250 t/d) SO_2-based volcanic activity levels.

We additionally present a SO_2 flux time-series from a second UV Camera system (UV7), deployed on the western outer summit crater area, to image emissions from the South-West (SWC) and Central (CC) Craters of Stromboli. The UV7 records, that are representative of a shorter acquisition interval (from May 2017), and miss the eruptive period, fully confirm that ordinary phase (OP) activity is consistently associated with SO_2 fluxes <177 t/d, and that the low (0-70 t/d) to medium (70-170 t/d) SO_2 flux levels are characteristic of the ordinary activity of Stromboli volcano. In summary, our

observations confirm that the regular degassing regime is associated to statistically lower SO_2 fluxes than pre- to syn-eruptive (2014) EP. Any future increase to high and very high levels is thus to be viewed as a statistically significant indicator of a likely resumption of effusive activity at Stromboli. Furthermore, our results allow us to quantify the relative SO_2 contributions from NEC (from UV1 records) and CC+SWC (from UV7 records). We find that, during the ~19 months covered by the study, the NEC and CC+SWC SO_2 degassing contributions to the total SO_2 emissions average ~64% and ~42%, respectively (?). These results confirm the NEC vent area as the prevalent degassing source at Stromboli.

Besides explosive activity, Stromboli is characterized by persistent and vigorous degassing of the magma column that is generally understood as a quasi-steady ‘‘non-explosive’’ passive mechanism. At Stromboli, the rate of the convective magma transport in the shallow (< 3 km) plumbing system controls the total (active + passive) SO_2 flux. The idea that degassing drives eruptive activity at Stromboli raises the question of why different eruptive regimes exist, and which factors determine the transition between those identified. The 2014 eruption offered a unique opportunity for deciphering the transition between different eruptive styles.

Hence, we convert the UV1 and UV7 SO_2 fluxes into a magma input (degassing) rate time-series. Derived UV1 magma input rates averaged 0.03-0.97 m^3/s during the EP and 0.01-0.31 m^3/s the during OP. The averaged magma input rates calculated for UV7 is almost constant around 0.07 m^3/s. Our results point to an increase in vesiculated magma input rate into the shallow conduit of Stromboli well before the onset of the effusive phase during a precursory (pre-effusive) phase (June-July 2014). This phase was characterized by escalating Strombolian activity, with a weaker magma supply rate in the CC-SWC crater areas, relative to the NEC vent area.

Overall, our findings support the short-term variability in explosions and puffing, indicating that the degassing activity of the magma column at Stromboli can be very sensitive to changes in the magma supply rate of the shallow feeding system.

Keywords: Volcanic degassing, Stromboli, passive degassing, UV camera, long-term SO_2 fluxes, volcanic monitoring

4.1 Introduction

Few volcanoes have contributed more to our understanding of conduit processes driving mild explosive volcanic activity of mafic volcanoes than Stromboli (Ripepe et al., 2005). Many studies have been conducted to understand the in-conduit interactions between magmas and gas bubbles that, upon their ascent, coalescence, expansion, and explosive discharge, originate Strombolian activity (Chouet et al., 2003; Gaudin et al., 2017; Jaupart and Vergniolle, 1988; Ripepe et al., 2001, 2002, 2008). Ironically, however, the "explosive" gas release, albeit the focus of most studies, represents only a minor fraction of the total gas output at Stromboli. Indeed, explosive activity is accompanied by continuous passive degassing (Allard et al., 1994, 2008; Burton et al., 2003, 2009) and puffing (Ripepe et al., 2002; Harris and Ripepe, 2007; Tamburello et al., 2012; Gaudin et al., 2017a, 2017b), which together combine for the largest fraction of Stromboli's 'bulk degassing' (Tamburello et al., 2012). Regular Strombolian activity is periodically (1985, 2002–2003, 2007 and 2014) interrupted by lava effusions (Ripepe et al., 2005, 2009, 2017, 2019; Burton et al., 2009; Rosi et al., 2006, 2013; Calvari et al., 2011; Valade et al., 2016; Delle Donne et al., 2017; Di Traglia et al., 2019). These effusive events may even cause tsunamigenic landslides (La Rocca et al., 2004; Tinti et al., 2005, 2006; Chiocci et al., 2008; Pino et al., 2004, 2009; Pistolesi et al., 2020) with a direct impact on the island and nearby coastal areas, as it occurred, for the last time, in December 2002. On 6 August 2014, Stromboli's typical persistent explosive activity was interrupted by an effusive eruption from a fissure on the outer slope of the summit crater. This followed a few months of increased Strombolian activity (Valade et al., 2016; Rizzo et al., 2015; Valade et al., 2016; Ripepe et al., 2019). Lava was along along the Sciara del Fuoco scar for nearly three months, while explosive activity at the summit was virtually absent. This effusive eruption involved a total volume of lava ejected estimated to be 7.4×10^6 m^3 (Valade et al., 2016). Regular explosive activity was re-established only after the effusive phase that ceased on 13–17 November 2014 (Rizzo et al., 2015).

The interplay between explosive and effusive activity represents a remarkable opportunity to understand the dynamics of the erupting volcanic system of Stromboli. Within the framework of a EU-funded ERC project (www.bridge.unipa.it), a novel UV camera system was deployed on Stromboli in the months approaching the onset of the 2014 eruption. Previous work (Delle Donne et al., 2017) has focussed on understanding the SO_2 flux behaviour at the Strombolian-effusive transition. This study has shown that long-term investigations of SO_2 degassing activity using permanent UV Camera networks can help capturing the escalating Strombolian activity that drives the volcano to failure, and ultimately to erupt effusively. However, no specific work has focused so far on studying the implications of UV Camera networks for understanding the Stromboli SO_2 flux

behaviour during “regular” Strombolian activity.

Here, we attempt at filling this gap of knowledge by reporting on an unprecedentedly-long (~ 4.5 years) UV camera based SO_2 flux time-series from Stromboli volcano. Our observation period (June 2014–December 2018) not only encompasses the August 2014 effusive eruption (data previously discussed in Delle Donne et al., 2017), but also a period of 4 years of “regular” Strombolian activity (Zakšek et al., 2014; Rizzo et al., 2015; Valade et al.,2016; Delle Donne et al., 2017; Di Traglia et al., 2018). Our aim here is to analyse the SO_2 flux time-series to fully constrain the volcano’s regular SO_2 degassing activity. One of our instruments (UV1; Figure 3.1), installed two months before the 2014 lava effusion activity, successfully recorded the entire effusive activity event, which was characterized by the transition from Strombolian explosions to lava effusion on the NE flank, and, finally, by the re-establishment of ordinary activity. Therefore, we examine data streamed by this UV Camera to characterise the total (active + passive) SO_2 flux from the North-East Crater (NEC), to analyze SO_2 flux and its fluctuations, and to set quantitative thresholds discriminating between “regular”, “effusive” and “pre-effusive” activity. Our long SO_2 flux time-series shown here represent the longest and most continuous SO_2 flux record obtained with regular and automatic UV camera systems. Such robust SO_2 flux dataset enables the study of ordinary and effusive activity phases at Stromboli, suggesting possible thresholds, indicators of volcanic activity, hence as significant tool for volcanic monitoring. We additionally report on the first SO_2 flux time-series from a second UV Camera system (UV7; Figure 3.1), deployed on the western outer summit crater area to image emissions from the South-West (SWC) and Central (CC) Craters of Stromboli.

4.2 Methods

The total (active + passive) UV1 and UV7 SO_2 flux time-series we report on here (Figures 4.1.1 and 4.1.2) are derived by applying an automatic processing algorithm (see Delle Donne et al., 2017) to data streamed by the two camera systems. For detailed information about hardware and data processing see Chapter 3.

We also compare the UV Camera-based degassing results with seismic signals registered by the ROC station, co-located with the UV1 camera system and managed by the Laboratorio di Geofisica Sperimentale (LGS) of the University of Firenze (UNIFI) (Figure 3.1). Very Long Period (VLP) seismicity was detected by band-pass filtering the cumulative ground displacement in the 0.03–1 Hz frequency band. The VLP occurrence rate at ROC station (Figure 3.1) is evaluated on a daily basis.

At ROC, VLP signals are always clearly detectable above the seismic noise, being this station located at very close distance (<1 km) from the inferred position of the VLP source (Chouet et al., 2003).

4.3 Results

4.3.1 UV1Camera time-series

Here, we report on long-term SO_2 flux time-series by our UV-camera system (UV1) during 2014 to 2018. Drastic changes in degassing regime and seismic signals concurrent with the 2014 effusive unrest (Delle Donne et al., 2017) allow to divide the observational interval in two different phases: the Effusive Phase (EP, 01/06/2014 - 30/12/2014), covering the entire period before, during and immediately after the 2014 effusive eruption, and the following Ordinary activity Phase (OP, 01/01/2015 - 31/12/2018).

We caution that i) owing to the position of our measurement site, the total SO_2 flux time-series from UV1 (Figure 4.1) fully includes gas contributions from the north-eastern segment of the crater terrace, but does underestimate emissions from the central (CC) and south-western (SW) craters, which are partially hidden by the NE crater's ridge (Delle Donne et al., 2017) (see following Chapter 5 for an expanded discussion on spatially resolved SO_2 emission rates at Stromboli); ii) due to poor visibility condition and/or cloud coverage on the summit, we report no successful SO_2 flux detection for 20%.

Considering the entire acquisition period (June 2014-December 2018), the total daily averaged SO_2 flux exhibits an arithmetic mean value of 69±51 t/d (range, 6-572 t/d) (Figure 4.1a). The daily averaged SO_2 fluxes during the EP (phase) is manifestly higher, 130±104 t/d (range, 18-572 t/d). Before the onset of the effusion, in June to July 2014, the SO_2 flux ranges between 76±13 t/d and 403± 45 t/d, with temporal fluctuations following those of seismic VLP (Figure 4.3a, 4.3b). Specifically, the SO_2 flux progressively escalates from early June to mid-July 2014, and peaks at 403±45 t/d (on 8 July) during some episodic lava overflow events (Figures 4.1 and 4.3a), when seismic (Figure 4.3b) activity is also particularly strong.

After a general activity decrement in the second half of July, that is consistently observed in the SO_2 flux and VLP record (Figure 4.3b), explosive activity increased again in early August. This intensification in activity (Figure 4.3b), which finally leads to NEC failure and the onset of lava

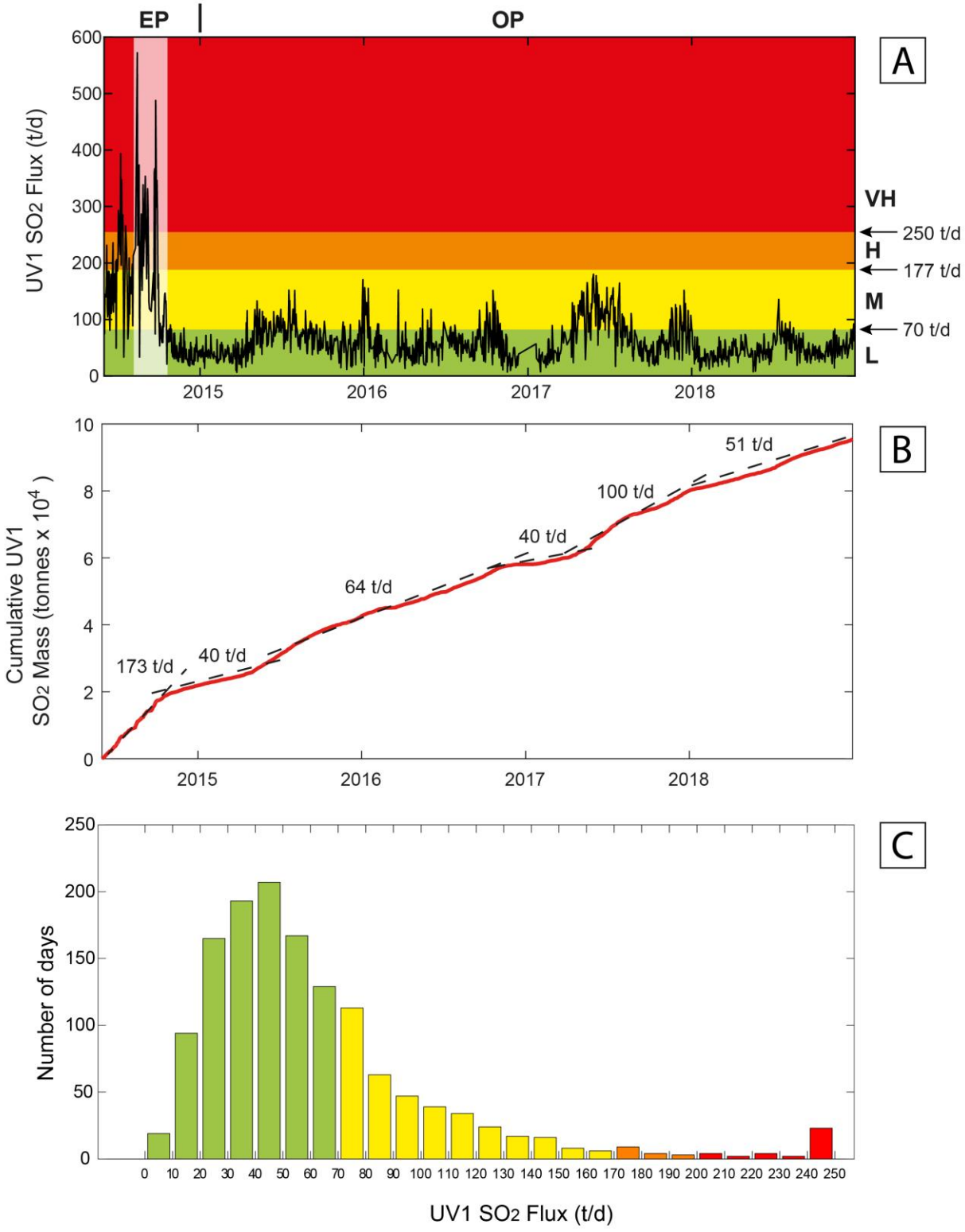

Figure 4.1 ***(a)*** *UV1 total daily averaged SO_2 fluxes during June 2014-December 2018 encompassing 2014 effusive eruption (EP) and 4 years of "regular" Strombolian activity (OP);* ***(b)*** *Cumulative SO_2 mass and* ***(c)*** *UV1 SO_2 flux histogram remarkably shows that the SO_2 flux remained at low levels for 974 day ('regular' activity) (L, M, H, VH indicate low, medium, high and very high activity levels, respectively in green, yellow, orange and red).*

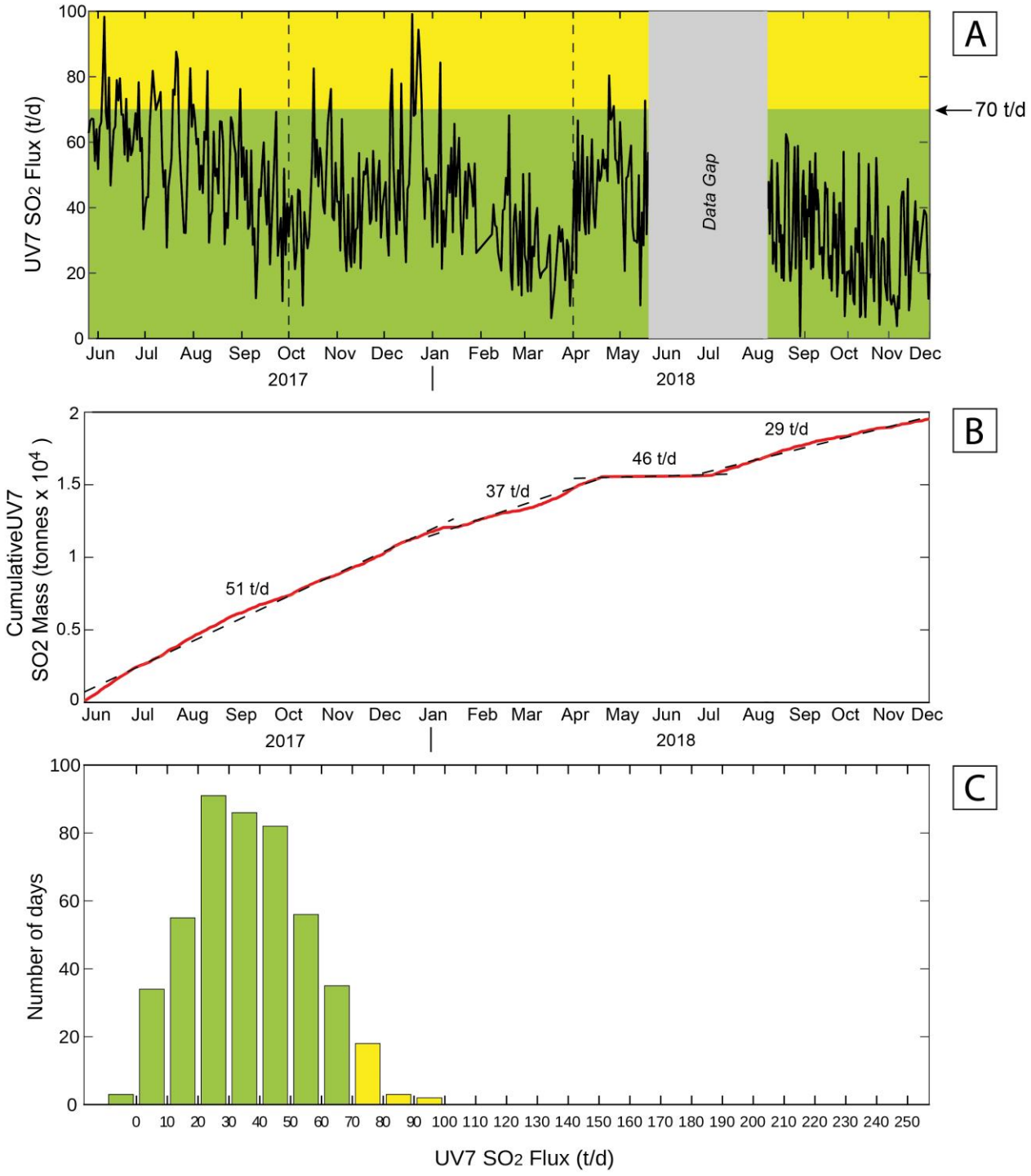

Figure 4.2 *(**a**)UV7 total daily averaged SO_2 fluxes during 2014-2018 encompassing 2014 effusive eruption (EP) and 4 years of "regular" Strombolian activity (OP); (**b**) Cumulative SO_2 mass and (**c**) UV7 SO_2 flux histogram highlight that the UV7 SO_2 flux remained at low levels during observational period.*

effusion, is not entirely captured by SO_2 flux observations, owing to poor visibility conditions from 6 August to 9 August (Delle Donne et al., 2017).

After the beginning of the effusive eruption, the SO_2 flux increases significantly, from 200±20 t/d to 572±66 t/d (Figure 4.1). Subsequently, moderate-to-high SO_2 fluxes (for Stromboli) and match the growing VLP seismicity (>20 events per hour; Figure 4.3b). An average of 25 VLP events per hour is detected during September. Since October 2014, however, as the effusive eruption is progressively waning, the SO_2 flux gradually decreases down to ~100 t/d, coherently with stable and low (<50 t/d) SO_2 fluxes that persist during the November 2014–April 2015 post-eruptive phase, period in which Strombolian activity is very weak (Figure 4.3b).

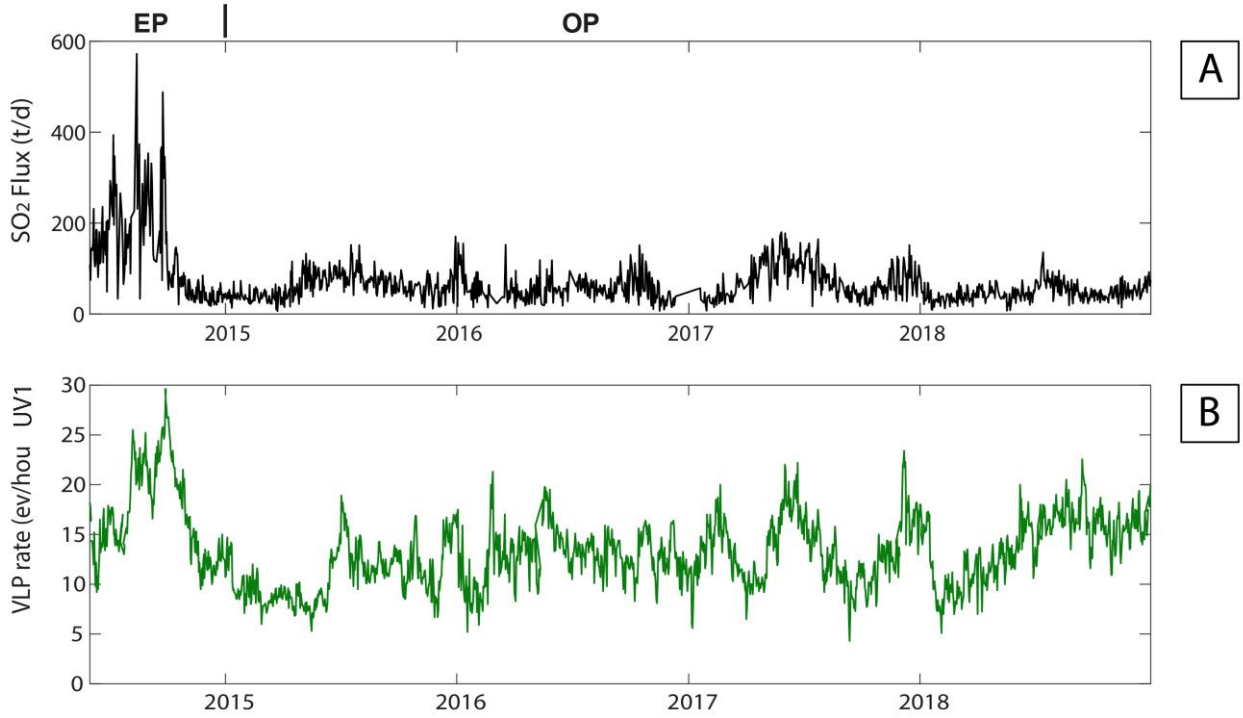

Figure 4.3 *(**a**) UV1 SO_2 flux compared to (**b**) VLP rate (ev/hour) registered by LGS.*

A mild SO_2 flux increase is observed after May 2015, simultaneously with a moderate increase in VLP seismic daily rate, and a progressive resumption of explosive activity at the summit craters (Figure 4.3a, 4.3b). From then onward, and until December 2018, the SO_2 flux remains at low levels (59±31 t/d; range, 7-180 t/d), far below those observed in the 2014 pre-effusion period. The 2015-2018 regular activity phase exhibits some mild fluctuations in SO_2 degassing regime (Figure 4.1). From January to October 2016, SO_2 fluxes fluctuate in the range 6-152±27 t/d, but then increase from February 2017 (15 t/d) and peak on June 2017 (180 t/d), matching well the increase in VLPs (>20 events/hour). SO_2 degassing then returns to very low values in November-December 2017, when low

activity is observed. Finally, a final SO_2 increasing phase is observed in summer 2018 (135 t/d). Overall, the OP SO_2 fluxes are about half lower than in the EP phase.

4.3.2 UV7 Camera time-series

The UV7 camera system was more recently put in operation, and here we report on long-term SO_2 flux time-series taken during 2017 to 2018. SO_2 flux fluctuations in degassing regime and seismic signals allow to divide the observational interval in three different phases: Phase 1 (26 May-30 September 2017), Phase 2 (1 October 2017-31 March 2018) and Phase 3 (1 April 2018-31 December 2018) (see Figure 4.2).

Owing to the position of measurement site, our SO_2 flux time-series from UV7, illustrated in Figure 2, fully includes gas contributions from the south-western (SW) and central (CC) craters, but do underestimate emissions from the north-eastern segment of the crater terrace (see following Chapter 5). We highlight that due to poor visibility condition and or cloud coverage on the summit, we report no successful SO_2 flux detection for 25%.

Considering the entire acquisition period (May 2017-December 2018), the SO_2 daily averaged flux exhibits an arithmetic mean value of 43±19 t/d (range, 1-99 t/d) (Figure 4.2a). The daily averaged SO_2 fluxes during Phase 1 is 55±17 t/d (range, 11-98 t/d). In Phase 2, the daily averaged SO_2 flux is slightly lower, 41±17 (range 6-99 t/d). In this phase, the SO_2 flux increases to ~82 t/d in mid-October, followed by a decrement until December, when the SO_2 flux increases again, reaching the highest SO_2 daily average of the entire period of study (~99 t/d). The SO_2 flux in subsequent months of Phase 2 progressively decreases in correlation with VLP record (Figure 4.4a, 4.4b). The SO_2 fluxes then fluctuate in the range 1-80 t/d, maintaining at low activity levels. The daily averaged SO_2 flux in Phase 3 is 37±17 t/d (range 1-80 t/d). This degassing phase is characterized by a progressive decrement of SO_2 fluxes that inversely correlate with a gradual escalation of VLP seismic rate afore in Section 4.3.1).

The UV7 SO_2 flux record is compared with the UV1 record in Figure 4.5a. Overall, the SO_2 flux sensed from the CC and SWC sectors (imaged by UV7) is at the lower range of that resolved by the UV1 camera (that images NEC emissions). To illustrate the UV1 to UV7 degassing fluctuations, we calculate the relative contributions of NEC and SWCC to the SO_2 budget using the dimensionless ratio R_Φ (Figure 5b):

$$R_\Phi = (\Phi_{NEC} - \Phi_{SW+CC})/\Phi_{TOT} \quad (1)$$

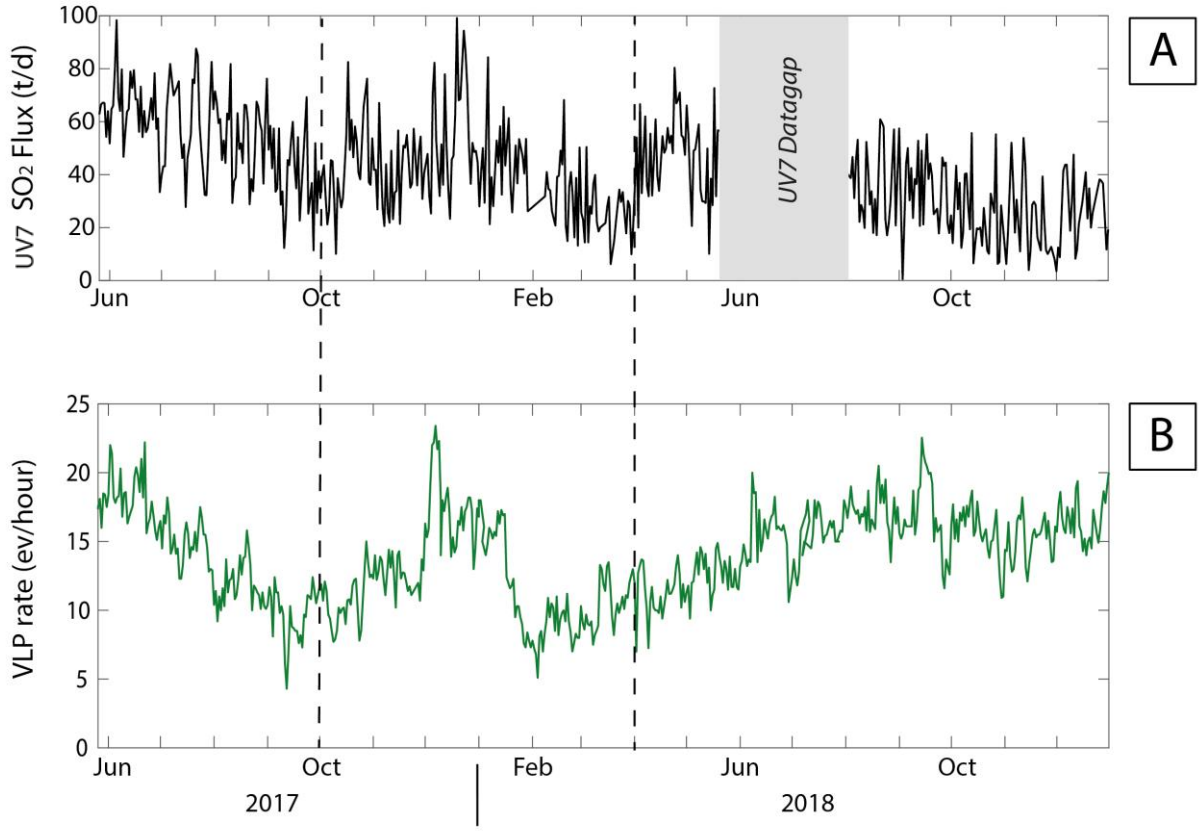

***Figure 4.4** (**a**) UV7 SO_2 flux compared to (**b**) VLP rate (ev/hour) registered by LGS*

where Φ_{NEC} is the daily average SO_2 flux from NEC, Φ_{SW+CC} is daily average SO_2 flux from SWCC, and Φ_{TOT} is the total daily averaged SO_2 flux between NEC and SW+CC. When the two crater areas contribute same amounts of gas, R_Φ approaches ~0. R_Φ values >0 and <0, respectively means that NEC emits more SO_2 than SW+CC, and vice versa (see Figure 4.5b).

4.4 Discussion

4.4.1 Establishing SO_2 threshold levels

SO_2 degassing varies with the level of volcanic activity, and at Stromboli ranges from <150 t/d to >>500 t/d (as registered during 2002-2003 effusive eruption) (Burton et al., 2003, 2009; Tamburello et al., 2012; Delle Donne et al., 2017). Our long and robust SO_2 flux dataset paves the way to characterising the background fluctuations in SO_2 emissions from the NEC (UV1) and CC+SWC (UV7).

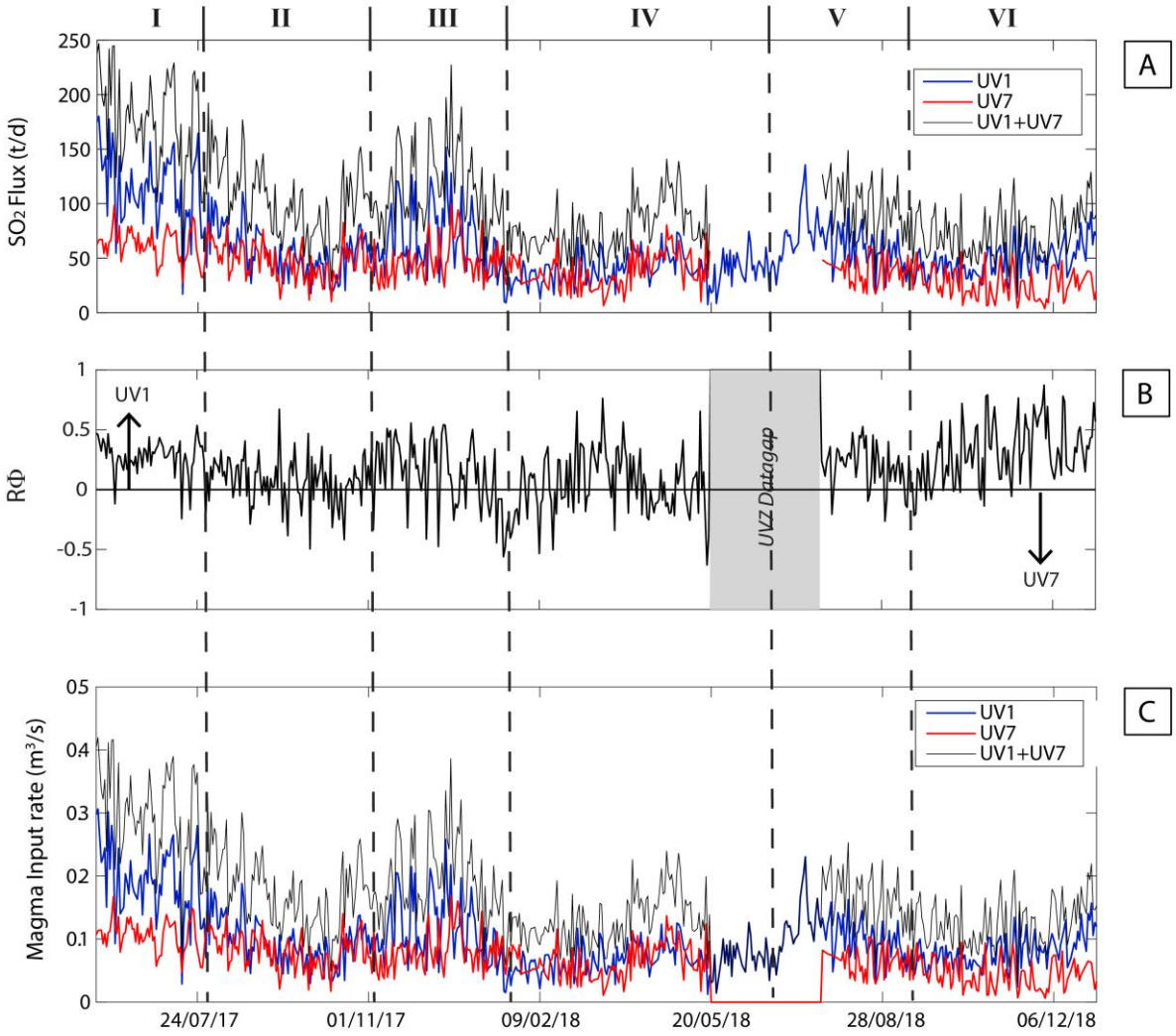

Figure 4.5 *(a) UV1, UV7 and UV1+UV7 SO_2 flux; (b) ratio RΦbetween UV1 and UV7 (see Text for details); (c) UV1, UV7 and UV1+UV7 magma input rate (m^3/s) during May 2017-January 2018 (see Chapter 5 for more detailed results).*

Our results show that, in 4 years of observations of regular activity (2015-2018), the SO_2 flux never exceeded ~180 t/d at UV1, the instrument with the longest record. We thus consider a < 180 t/d SO_2 flux range as representative of regular activity, and use this to set 'threshold-values' associated to periods of low (<70 t/d), and medium (70-177 t/d) degassing (Figure 4.1a). Our 4-year long time-series also shows that higher SO_2 degassing levels have only been reached prior and during the 2014 effusive eruption (see also the cumulative SO_2 plot of Figure 1b). We consequently use these EP records to manually set the thresholds of high (178-250 t/d) and very high (>250 t/d) SO_2-based volcanic activity levels. The histogram of Figure 1c remarkably shows that, from June 2014 to December 2018, the SO_2 flux remained at low levels for 974 day, at medium levels for 367 days, and high to very high levels for only 51 days (4%) of the observational period (1392 days).

The UV7 records, that are representative of a shorter acquisition interval, and miss the eruptive period, fully confirm that OP activity is consistently associated to SO_2 fluxes <177 t/d, and therefore the low (0-70 t/d; green bars) to medium (70-170 t/d; yellow bars) SO_2 flux levels are characteristic of the ordinary activity of Stromboli volcano (Fig. 4.2a,b,c). In summary, our observations confirm that the regular degassing regime is associated to statistically lower SO_2 fluxes than pre- to syn-eruptive (2014) EP. Obtained results allow to set a "background picture of degassing" at Stromboli. Precursory changes in SO_2 flux prior to eruptions may now be compared to these thresholds established.

4.4.2 Magma input budgets

Besides explosive activity, Stromboli is characterized by persistent and vigorous degassing of the magma column that is generally understood as a quasi-steady (Allard et al., 1994) ''non-explosive'' passive mechanism. As in other open-vent volcanoes (Shinohara, 2008), at Stromboli the rate of the convective magma transport in the shallow (< 3 km) plumbing system (Harris and Stevenson, 1997; Bonaccorso et al., 2008) controls the total (active + passive) SO_2 flux (Allard et al., 1994, 2008). Convection of ascending gas-rich fresh magma into denser, more degassed magma in the conduit activates the "degassing machine" that maintains Strombolian persistent explosive activity (Allard et al., 1994, 2008; Harris and Stevenson, 1997; Chouet et al. 1974). This mechanism explains the longevity of Strombolian activity (Rosi et al., 2013), the observed excess SO_2 degassing (Allard et al., 2008), and the overall homogeneity of magma chemistry (Bertagnini et al., 2008).

The dynamics of the volcanic conduit system are thought to be driven primarily by gas, as evidenced by the relative masses of erupted gas and pyroclastic rocks (Mori and Burton, 2009; D'Oriano e al., 2010). The idea that degassing drives eruptive activity at Stromboli raises the question of why different eruptive regimes exist, and which factors determine the transition between these regimes. The 2014 eruption offers a unique opportunity for deciphering the transition between different eruptive regimes, because normal activity ceased temporarily during the effusive phase of the eruption and because its re-establishment starting in November 2014 was recorded in detail by the UV camera station.

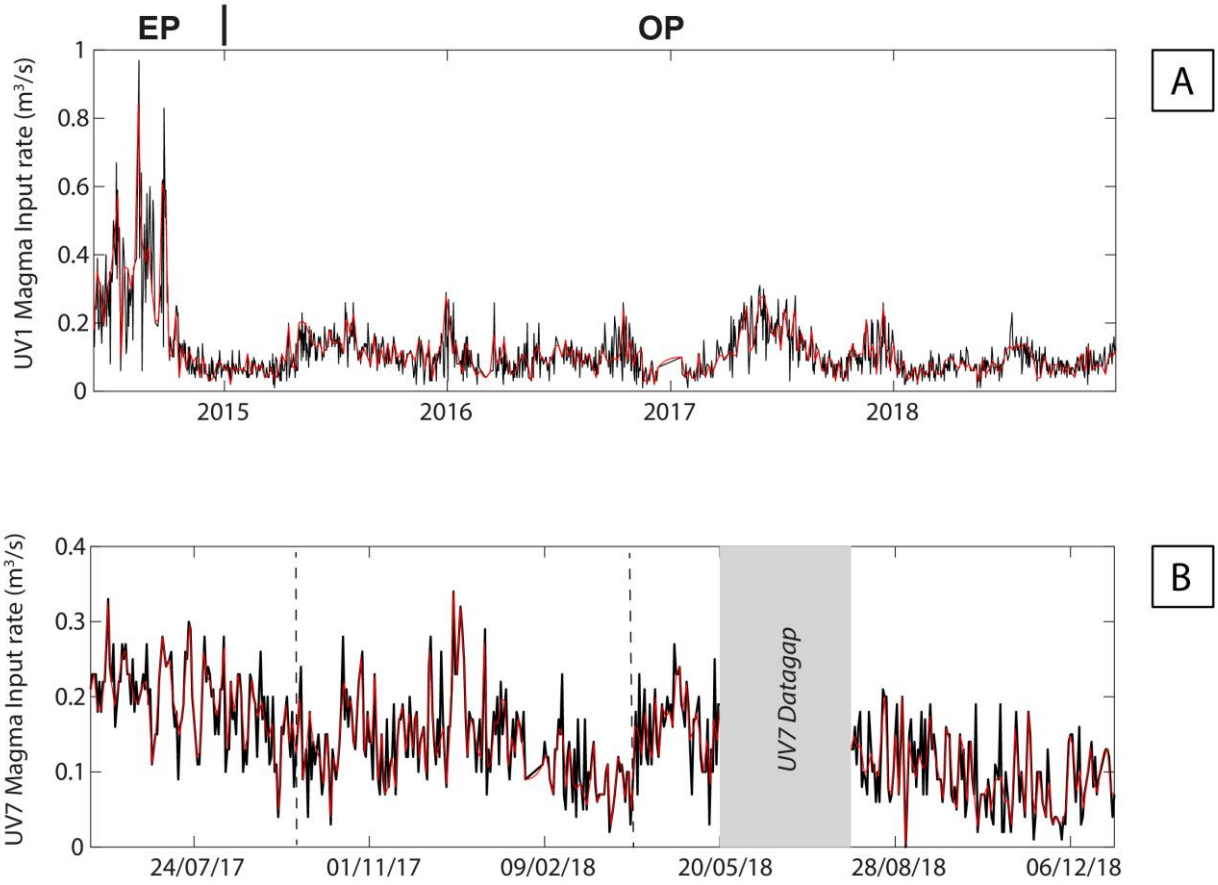

Figure 4.6 *(a) UV1 and (b) UV7 magma input rate (m^3/s) calculated for a period during June 2014-December 2018 and May 2017-January 2018, respectively (see Section* ***4.4.2****).*

As other recent (post-1985) effusive unrests at Stromboli, the 2014 eruption starts at the climax of a phase of escalating Strombolian activity, observed weeks prior to the effusive eruption, in which explosions became more frequent and intense than usual (De Fino et al., 1988; Barberi et al., 2009; Ripepe et al., 2005, 2009; Calvari et al., 2010). Detailed analysis of SO_2 flux time-series shows distinctive degassing variations, with significant SO_2 flux increase from July 27 to August 14, peaking up to ~573 t/d eight days before the onset of lava effusion.

Following the methodology of Allard et al. (1994, 2008), we convert the UV1 and UV7 SO_2 fluxes (Figures 4.1 and 4.2) into a magma input (degassing) rate time-series (Figures 4.6).

$$\text{MIR } [m^3/s] = \frac{\left(\frac{S_{[g/mol]}}{SO_{2\ [g/mol]}}\right) * SO_2 \text{ Flux } [kg/s]}{(S_0\ [\text{wt. \%}] * \rho\ [kg/m^3] * \text{ cristallinity } [\%])}$$

For that we use our measured SO_2 flux values, an initial sulphur content in Stromboli magmas of 0.18 wt.%, a density of 2700 kg/m^3 and 30% crystallinity (Métrich et al. 2010). Considering the UV1 dataset, our derived NEC magma input rates average 0.03-0.97 m^3/s during the EP and 0.01-0.31 m^3/s the during OP (Figure 4.6a). These results confirm the previously established magma supply rates during periods of regular explosive activity (0.1–0.3 m^3/s; Harris and Stevenson, 1997; Allard et al., 1994; Burton et al., 2007; Ripepe et al., 2005), and strongly implicate that effusive eruptions are systematically associated with higher magma ascent rates (> 0.3 m^3/s) (Figure 4.5c, 4.6a and 4.3b).

The UV7 dataset (Fig. 4.5c, 4.6b) is consistent with this scenario, as it shows that during 2017-2018, when regular activity prevailed, the magma input rate systematically remained below 0.3 m^3/s. The averaged magma input rates calculated for UV7 for the three Phases is almost stable around 0.07 m^3/s, though slightly higher in Phase 1 (0.068 m^3/s) compared to Phase 3 (0.058 m^3/s) (Figure 4.5c, 4.6b). These averages suggest a lower magma supply rate in the CC-SWC crater areas, relative to the NEC vent area (Figure 4.5c).

Our results (Fig. 4.6a) point to an increase in vesiculated magma input rate into the shallow conduit of Stromboli well before the onset of the effusive phase, during a precursory (pre-effusive) phase (June-July 2014) characterized by escalating Strombolian activity and generating into nine lava overflows (Valade et al., 2016; Delle Donne et al., 2017). From our results, we can therefore confirm that the effusive eruption trigger is the faster shallow circulation of gas-rich (buoyant) magma. SO_2 fluxes and seismic activity are geochemical and geophysical proxies for bubble gas-rich magmas. These parameters point to a change in the amount of gas provided by Stromboli. An increase in magma supply rate then drives the transition from regular explosive to effusion regimes (Ripepe et al., 2005, 2009, 2015; Calvari et al., 2010). This increased magma transport in the shallow feeding conduit(s) initially causes intensification of Strombolian activity and finally leads to onset of lava effusion opening a fracture in the gravitationally unstable SdF. The precursory acceleration of Strombolian activity is typically detected by large variations in geophysical parameters (Ripepe et al., 2009, 2015; Valade et al., 2016) but, as we show here, can also be identified in the gas flux record (Delle Donne et al., 2017).

Overall, our findings support the short-term variability the short-term variability in explosions and puffing (Kondo et al., 2019), indicating that the degassing activity of the magma column at Stromboli can be very sensitive to changes in the magma supply rate of the shallow feeding system.

4.4.3 Vent-resolved SO_2 emissions

Our results also offer the opportunity to spatially resolve where degassing activity is concentrated along the crater terrace. This topic is the main chapter of the following Chapter 5, but some preliminary results of the coupled UV1 and UV7 analysis of SO_2 flux datasets is illustrated here (Figure 4.5b).

Our results allow us to constrain the relative SO_2 contributions from NEC (from UV1 records) and CC+SWC (from UV7 records). We find that, during the ~19 months covered by the study, the NEC and CC+SWC SO_2 degassing contributions to the total SO_2 emissions average ~64% and ~42%, respectively These results confirm the NEC vent area as the prevalent degassing sources at Stromboli (Fig. 4.5b). These degassing fractions oscillate over time, however. In particular, the NEC (UV1) degassing accelerates over the CC+SWC (UV7) degassing in 3 different phases, when $R_\Phi > 0$ (Figure 4.5b): Phase 1 (relative contributions, ~64% and ~36% of bulk plume) and, less markedly in Phase 3 and Phase 5 (relative contributions of respectively 62% and 38% for UV1 and UV7). In contrast, the two source areas contribute roughly similar SO_2 amounts in Phase 2, Phase 4 and Phase 6 (57% and 43% for UV1 and UV7, respectively), when we observe R_Φ close to ~0. The implications of these vent-to-vent SO_2 degassing shifts are further explored in the next chapter.

4.4.4 Seasonality in "regular" SO_2 degassing

4.4.4.1 Periodicity in volcanic degassing

Persistent passive degassing is a common characteristic of active volcanoes. Distinct periodic components in composition and flux of volcanic gases have been widely identified over timescales ranging from seconds to months. The development and implementation of high temporal resolution gas measurement techniques, such as the UV camera, now enables the study of high frequency processes operating on timescales comparable to those detectable in geophysical datasets.

What are the drivers of the periodicities hitherto identified in volcanic outgassing is a source of debate. These include exogenous (e.g. atmospheric or neatly generated) and endogenous effects, the latter related to (i) shallow gas processes; (ii) shallow; and/or (iii) deep magmatic processes.

Volcano	Magma Type	Period (units)	Notes	Key References
Ambrym	Basalt	100–200, 480 s	Ratio data	Allard et al. (2016)
Cotopaxi	Andesite / Basaltic-Andesite	13.7 d	Ratio data	Dinger et al. (2018)
Erebus	Phonolite	100–600 s 600 s 10–360 min	Fluxes and Ratio data	Ilanko et al. (2015) Girona et al. (2015) Sweeney et al. (2008) GVP (2019) Oppenheimer et al. (2009)
Erta Ale	Basalt	1 h	Bubble volume	Bouche et al. (2010)
Etna	Basalt	40–340 500–1200 s	SO_2 flux and ratio data	Tamburello et al. (2013) Pering et al. (2014) Pering et al. (2017)
Fuego	Basalt	70–430 s	SO_2 flux	Nadeau et al. (2011) Pering et al. (2019)
Gorely	Basalt	60–510 s	SO_2 flux	Aiuppa et al. (2012) Pering et al. (2019b)
Kīlauea	Basalt	1–3600 s 1.6–7.8 h 4 m–15.8 h	Gas Pistoning; different ranges represent different time periods.	Johnson et al. (2005) Patrick et al. (2016)
Llaima	Basalt	14 d	SO_2 flux	Brenemeyer et al. (2014)
Masaya	Basalt	200–300 s 50–180 d	SO_2 flux	Pering et al. (2019a, 2019b)
Mayon	Andesite / Basaltic-Andesite	100–500 s 600–900 s 1200–1600 s 2000 s	H_2O flux	Girona et al. (2015)
Soufrière Hills	Andesite / Basaltic-Andesite	30–50 d 100–340 d	SO_2 flux	Flower et al. (2015) Nicholson et al. (2013)
Pacaya	Basalt	330–3000 s	SO_2 flux	Battaglia et al. (2018) Pering et al. (2019b)
Popocatépetl	Andesite / Basaltic-Andesite	250, 330 s	SO_2 flux	Campion et al. (2018)
Sabancaya	Andesite / Basaltic-Andesite / Dacite	240 s 120, 420 s	CO_2/SO_2 Ratio SO_2 flux	Moussallam et al. (2017)
Stromboli	Basalt	~1–5 s 5–40 m	Strombolian activity	Ripepe et al. (2002) Spampinato et al. (2012)
Turrialba	Andesite / Basaltic-Andesite	100 s 10–14 d	SO_2 Flux	Campion et al. (2012) Conde et al. (2014)
Ubinas	Andesite / Basaltic-Andesite	400–900 s 900–1200 s 1500–2500 s	SO_2 Flux	Moussallam et al. (2017) Pering et al. (2019b)
Villarrica	Basalt	None 30–50 s 340–710 s 14 d	SO_2 flux SO_2 concentration	Liu et al. (2019) Moussallam et al. (2016) Bredemeyer et al. (2014)
Yasur	Basalt	~10 s–10 m	Strombolian activity	Oppenheimer et al. (2006) Bani et al. (2007) Kremers et al. (2013)

Figure 4.7 *Table summarizes the literature associated with the full range of currently resolvable periodicities within volcanic degassing timeseries (modified from Pering et al., 2019)*

The longest identified timescale periodicities in volcanic outgassing are of the order of days to months, and it is generally accepted that these periodic components originate from deep processes related to large-scale magma movement (Rymer et al., 2005; Christopher et al., 2015; Flower and Carn, 2015; Pering et al., 2019).

Instead, high-frequency variations in volcanic degassing depend on a wide range of potential drivers such as, i) atmospheric processes (Pering et al., 2014, 2019) or tidal forces (Sweeney et al., 2008; Dinger et al., 2018), ii) bubble movement through the more constrained conduit geometries (Bouche et al., 2010), iii) bubble waves or bubble self-organization into layers (Tamburello et al., 2013), iv) turbulent effect caused by bi-directional magma mixing during ascent and descent within the conduit (Moussallam et al., 2016), v) turbulence atmospherically-generated at plume exit (Liu et al., 2019), v) puffing (i.e., the bursting of larger non-pressurized bubbles, Gaudin et al., 2017; Pering et al., 2018), vi) clusters of bubbles (or slug trains) (Pering et al., 2017), vii) rheological stiffening of the upper conduit (Nadeau et al., 2011), physical conditions within the conduit (Costa et al., 2007). The observed periodic behavior is not restricted to SO_2 flux measurements alone, and periodicity can also be identified in timeseries of molar gas ratios (e.g., Pering et al., 2014; Ilanko et al., 2015; Dinger et al., 2018).

The periodicities within volcanic gas datasets are quantified based on the principle of spectral analysis, or frequency analysis, whereby timeseries data are decomposed into a series of waves of known wavelength and amplitude, to determine the strength of different frequencies within discrete datasets. Recently, Pering et al. (2019) summarizes the literature associated with the full range of currently resolvable periodicities within volcanic degassing timeseries (Figure 4.7).

For instance, using a UV camera on Etna volcano, Tamburello et al. (2013) identified two sets of periodicities in an high resolution SO_2 flux time-series: short-period cycles of 40–250 s (centered on 150 s), and long-period cycles of 500–1200 s (centered on 600 s). The higher frequency periodicities were often sustained on timescales of tens of minutes. Similarly, Pering et al. (2014a) identified on Etna volcano short-period cycles of ~89 and ~185 s in SO_2 flux, but also identified a mid-range period of ~340 s. The authors neglected an atmospheric processes component because ~89 s cycle was observed also in CO_2/SO_2 molar ratio and, specifically, assert that no plausible mechanism exists for fractionating preferentially one gas species from another during short plume transport.

The explosive activity makes an important part of the degassing record and the resultant frequency characteristics at these volcanoes. Indeed, patterns in explosive events could be linked to the fluid dynamics of the bubbles that drive them (Gaudin et al., 2017; Pering et al., 2018). Spampinato et al. (2012) highlight the periodic characteristics of explosive activity on Stromboli and Etna in thermal

data (which would also manifest as changes in degassing). At Etna, the authors highlight distinct periods of 4–9 s, 23–45 s, and 1–10 min. The shortest timescale is attributed to puffing (the bursting of larger non-pressurized bubbles; Gaudin et al., 2017; Pering et al., 2018), while the latter timescales are associated with clusters of bubbles (or slug trains, see Pering et al., 2017) arriving periodically at the surface. Of particular interest is the correlation of these periodicities with phases in activity, whereby longer periods of 1–10 min are associated with stronger gas supply (Spampinato et al., 2012). At Stromboli, Ripepe et al. (2002) and Spampinato et al. (2012) focused on puffing activity showing a change in the vigor of activity, 1–2 s and 3–5 s during stronger and weaker phases respectively, with this activity occurring over periods of 5–8 and 5–40 min cycles, likely associated with overall gas supply from depth. Any consideration of periodic components in long-term passive gas flux on the order of seconds to hours would require deconvolution from the active degassing (i.e., the explosive Strombolian eruptions or puffing).

Longer-term variations in gas release over days to months (and years where datasets are available) can be broadly attributed to processes occurring deeper in the magmatic system, such as (a) the addition of new, volatile-rich magma to a storage zone and the rejuvenation of the resident magma body, or (b) deep volatile segregation, leading to recurring mush destabilization and upwards melt-decoupled volatile transport (Christopher et al., 2010, 2015;Bachmann et al., 2006). As shown in Figure 4.7, very few works studied long time-series, as to individuate days periodicities (Nicholson et al. 2013; Flower et al., 2015; Pering et al., 2019). Pering et al (2019) used NOVAC (Network for Observation of Volcanic and Atmospheric Change) data of Aiuppa et al. (2018), which spans over the period March 2014 to September 2016 (Galle et al., 2010), and conducted CWT and Lomb-Scargle analysis to highlight the presence of significant periodic components within the SO_2 flux dataset. In the Lomb-Scargle analysis, the dominant of these has a period of 178.9 days, which is similar to the duration of the solar semiannual tide of 182.6 days (the semiannual tide) (Agnew et al., 2007). Another cycle has a 23.6 day period, which appears too short to be linked to the lunar 27.6 day cycle (Dinger et al., 2018; Agnew et al., 2007). Further periodicities at 140, 121, 94, and 46 days could reflect the volcanic influence at Masaya, involving replenishment of magma into storage zones.

In the next paragraphs, we discuss the periodicities of the SO_2 flux time-series measured from the UV1 permanent camera at Stromboli (see Section 4.3.1).

4.4.4.2 Decomposition in trend and seasonality

In order to investigate UV1 SO_2 flux periodicity, we performed a spectral analysis using "pwelch" function in Matlab that allows to estimate Welch's power spectral density (Welch et al., 1967), a variant of Fast Fourier Transform (FFT). The method is based on the concept of using periodogram spectrum estimates, which is the result of converted signal from the time domain to the frequency domain. Welch's method is an improvement on the standard periodogram spectrum.

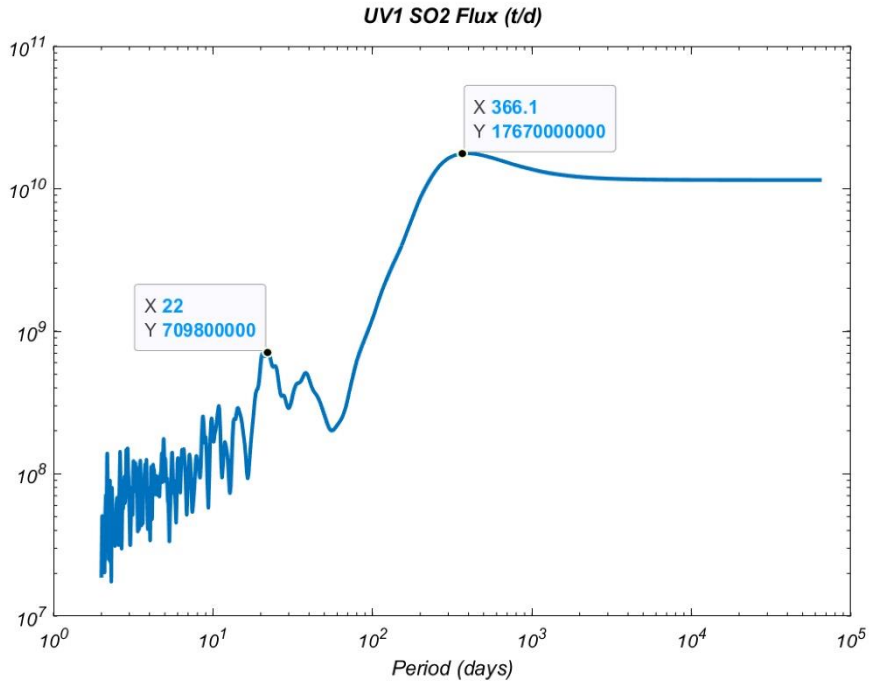

Figure 4.8 *Power spectral density (PSD) of UV1 SO_2 flux signal (measurement period: June 2014-December 2018).The periodogram highlights two main frequencies (22 days and 366 days)*

The FFT allows to write a time-dependent function in the frequency domain, thanks to the decomposition of it in exponential functions with a scalar product, a representation often called *spectrum*. Thus, it can be used to determine the strength of a periodic component at each frequency. Figure 4.8 shows the power spectral density (PSD) form, of UV1 SO_2 flux signal. Peaks in the periodogram, discernable above noise models (i.e., to determine at what point a peak should be considered noise), highlight frequencies which are manifested most strongly in the time-series, i.e., those which may be periodic. We infer an annual period (366 days) and a 22 days period that appears too short to be linked to the lunar 27.6 day cycle (Dinger et al., 2018).

In order to further investigate UV1 SO_2 flux periodicity and their possible contribution/influence on degassing dynamics, we decide to remove the seasonal variations in the SO_2 flux time-series to obtain the residual trend.

In this context, a time series can be thought as the sum of three components: i) a **trend** component that changes slowly over time and that essentially determines the level of the series; ii) a **seasonality** that is the same or almost at a fixed distance over time (ad example, in monthly series every 12 months, in quarterly series every 4 trimesters, in daily series, every 7 days); iii) an **irregular component** a more erratic component that determines in the series of typically short-term fluctuations.

We denote the three components with T_t, S_t and I_t respectively. The ways in which they can interact to "form" the observed time-series can be different. Some examples are the following composition "models":

additive: $y_t = T_t + S_t + I_t$;

multiplicative: $y_t = T_t \cdot S_t \cdot I_t$;

multiplicative with irregular component additive: $y_t = T_t \cdot S_t + I_t$.

There are some useful techniques to decompose a time series in its elementary components and , in particular, to estimate its seasonal component. One use of these techniques consists in the production of the so-called “seasonally adjusted series”, that is a series in which the periodic part can be removed.

The details of different techniques depend on the model of composition. For example, in the case of a model additive/multiplicative is sufficient subtract from/divide the original time-series for the seasonal component, normally assimilated to a stochastic stationary process.

Why “de-seasonalize/adjust seasonally”? The seasonal component often forms one part of the time-series whose existence is obvious and whose explanation it is known and, therefore, not particularly significant, but at the same time, however, it can be sufficiently "big" for disguise other trends.

To explain the seasonal decomposition techniques, we show as an example the monthly series of CO_2 measurements at Mauna Loa (a location in Haway) (from Cleveland et al., 1990).

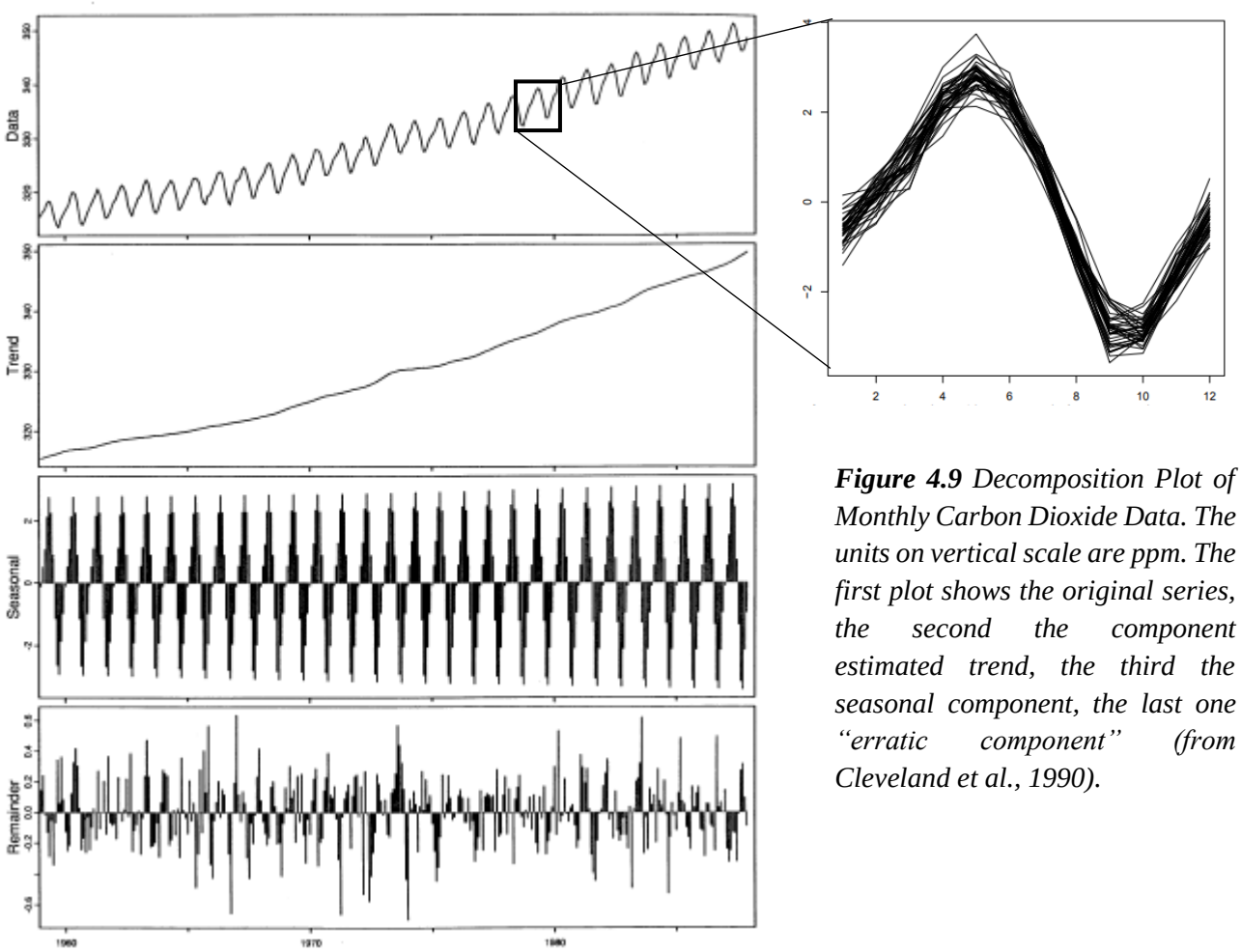

Figure 4.9 *Decomposition Plot of Monthly Carbon Dioxide Data. The units on vertical scale are ppm. The first plot shows the original series, the second the component estimated trend, the third the seasonal component, the last one "erratic component" (from Cleveland et al., 1990).*

They are evident:

- a sufficiently regular *trend* component (could be a second-order polynomial)

- a *seasonal component* which make the series non-stationary.

The plot has been created by the authors in the following way: (i) first, the average has been subtracted from each observation of the 12 (one for each month) observations of every year; (ii) then, separately for each year, the 12 squares have been drawn towards the order number of the month.

The upper-right plot in Fig. 4.9 shows that the seasonal profile has basically remained the same for all 39 years considered. This leads to think of a model of the type

Time series = (Trend) + (Seasonality) + (Remainder)

In order to analyze and “seasonally adjust” our long and robust dataset of UV1 SO_2 flux time-series since 2014 to 2018, we choose to use the function "STL" in R. STL is a procedure for the simultaneous estimation of the trend and the seasonality of a time series. The basic idea is common to most used decomposition procedures. STL is a versatile and robust method for decomposing time series. STL is an acronym for “Seasonal and Trend decomposition using Loess”, while Loess is a method for estimating nonlinear relationships. The STL method was developed by Cleveland et al (1990). STL has several advantages over the classical decomposition methods: (i) STL is handle any type of seasonality, not only monthly and quarterly data; (ii) the seasonal component is allowed to change over time, and the rate of change can be controlled by the user; (iii) the smoothness of the trend-cycle can also be controlled by the user; (iv) it can be robust to outliers (i.e., the user can specify a robust decomposition), so that occasional unusual observations is not affect the estimates of the trend-cycle and seasonal components. They, however, affect the remainder component. The seasonal component is found by loess smoothing the seasonal sub-series. The automatic procedure (by setting s.window="periodic") usually gives a good balance between overfitting the seasonality and allowing it to slowly change over time. The seasonal values are removed, and the remainder smoothed to find the trend. The overall level is removed from the seasonal component and added to the trend component. This process is iterated a few times. The remainder component is the residual from the seasonal plus trend fit.

We calculate two trends: *trend1* (green line on plots) is the one using default parameters which finds a good balance between not exaggerating too much in extracting seasonality (‘overfit’) and allowing a good variation of the trend over time; *trend 2* (red line on plots) is obtained by 'pushing' slightly with seasonality fit. As shown in Figure 4.10a, the trend is a bit more complex.

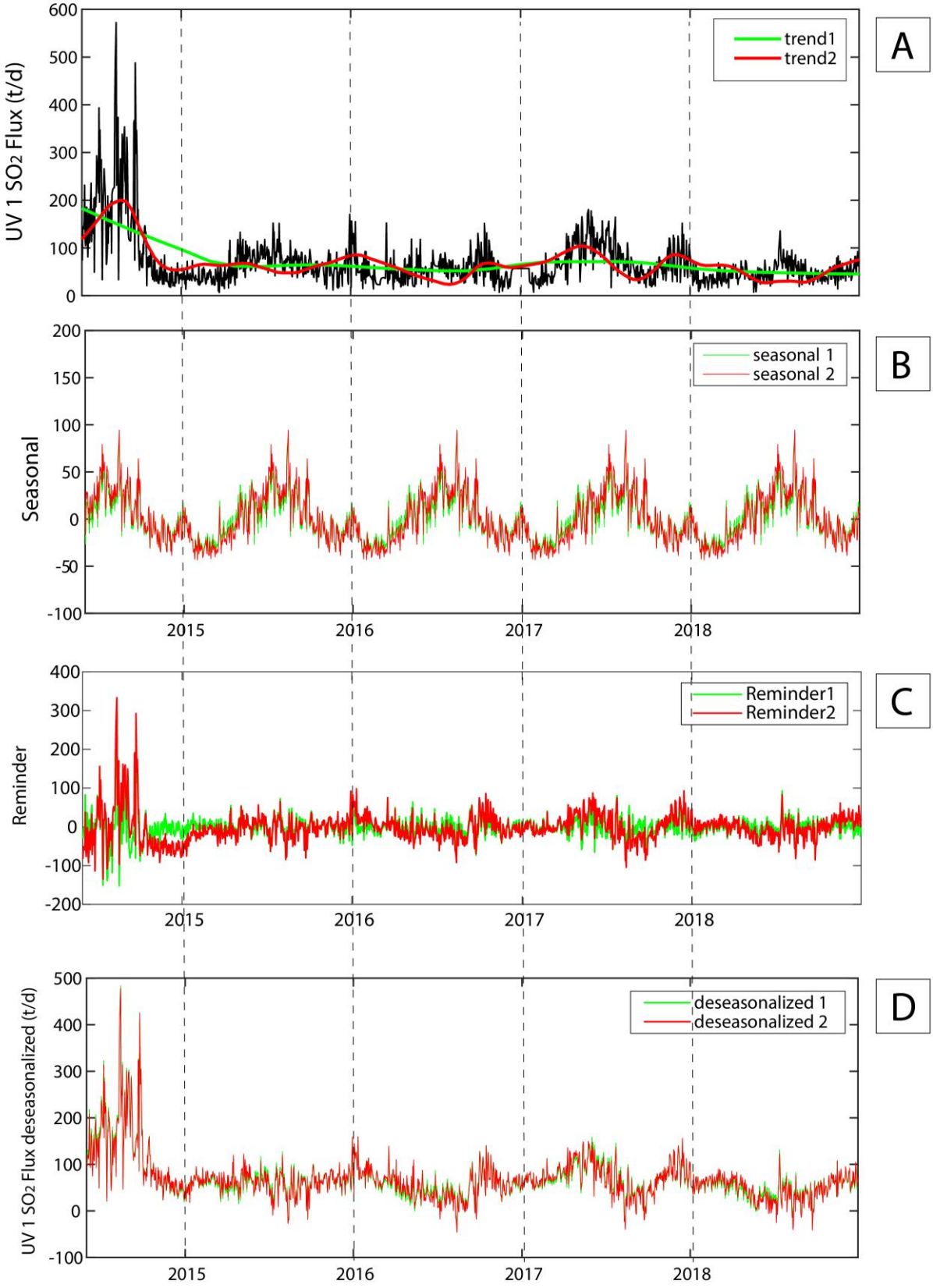

Figure 4.10 *(a) UV1 original SO_2 flux time-series with calculated trend 1 and 2, (b) seasonal 1 and 2 and (c) 'reminder 1 and 2 (green and red lines), using STL method (see Text for details); (d)UV1 SO_2 flux de-seasonalized points to an annual periodicity on Stromboli degassing during 2014-2018.*

The reminders in Figure 4.10c are obtained by subtracting from the original SO_2 time-series the trend and seasonal component. The reminder of the first trend still shows some fluctuations, suggesting an incomplete removal of the seasonality, which is,, instead, fully accomplished in the second trend (Figure 4.2.4c). However, both trends show that the 2014 effusive eruption was not influenced by seasonal cycles.

4.5 Conclusions

We analysed SO_2 degassing trends at Stromboli from June 2014 to December 2018. Our results are thus illustrative of the volcano's SO_2 degassing regime in the period prior to and during the effusive eruption that started on August 6, 2014. Importantly, our observations also characterise 4 years of degassing during "regular" Strombolian activity. Our results highlight large fluctuations in SO_2 flux behaviour that allow setting thresholds between different activity levels. High to very high levels are only observed prior and during effusive eruptions, when the magma input rate in the conduit accelerates to >0.3 m^3/s. During regular activity, SO_2 emissions and magma input rates are systematically lower (< 180 t/d and > 0.3 m^3/s).

Our results represent the first multi-year SO_2 flux time-series ever recorded in an active volcano with a UV-camera-based system. The UV1 dataset of Stromboli allows to investigate SO_2 degassing for a very long period, since 2014 to 2018. We identified with FFT analysis an important 1-year long periodicity in the time-series, probably linked to non-volcanic events. In order to remove such external component from the SO_2 flux time-series, we use the algorithm STL ('Seasonal and Trend decomposition using Loess') that is a procedure for the simultaneous estimation of the trend and the seasonality of a time series. The de-seasonalized trend highlights that the 2014 Stromboli eruption, during which variation remains strong in the trend, was not affected by seasonal cycles and, therefore, might be related entirely to endogenous factors, as magma replenishment inside the deep plumbing system of Stromboli. The origin of the seasonal component is probably related to different sunlight conditions between the winter and summer seasons that could influence UV camera measurements. The physical process that may cause this cyclicity, however, are beyond the scope of the present study.

– *Results Chapter 5* –

"Degassing dynamics of Stromboli volcano (Italy) inferred from vent-resolved SO_2 fluxes"

Lo Coco E., Delle Donne D., Bitetto M., Ripepe M., Tamburello G., and Aiuppa A., *"Degassing dynamics of Stromboli volcano (Italy) inferred from vent-resolved SO_2 fluxes"* (ready to be submitted)

Abstract

We report on high frequency (~0.5 Hz) automatic measurements of the SO_2 flux at Stromboli, obtained by a network of two permanent UV cameras that allow, for the first time at this volcano, to simultaneously resolve SO_2 emissions from the different active craters. Our results highlight substantial swings in degassing activity in between the craters during only <8 months of observations (June 2017 - January 2018). We find that whilst the SO_2 flux from the South-West/Central craters (SWCC) remains relatively constant at 51±16 t/d, the NEC (North-East crater) flux oscillates more widely (13-155 t/d). The NEC vs SWCC relative contributions to the total SO_2 flux thus vary between ~63% and ~37% (June-July 2017) to 54% and 46% (August-October 2017). Importantly, these crater-to-crater modulations in SO_2 emissivity correspond to consistent shifts in infrasound source (as recorded by a small-aperture infrasonic array), thus validating our spatially resolved SO_2 flux records. Clustering of degassing activity at the NEC corresponds to periods of heightened explosive activity, as demonstrated by SO_2 and seismic records. We interpret this as due to preferentially gas/magma channeling into the structurally weaker NE portion of the crater terrace as supply rate of buoyant, bubble-rich magma increases (up to ~0.3 m^3/s) in the shallow plumbing system. Robust SO_2 flux time-series, obtained from automatic processing of UV camera data, make it possible to resolve different degassing sources and active/passive degassing modes, thus becoming an important tool for volcanic monitoring.

Keywords: Volcanic degassing, Stromboli, Strombolian activity, UV camera, SO_2 flux, volcanic monitoring

5.1 Introduction

Stromboli volcano in the Aeolian Islands (Italy), a volcanic arc resulting from the subduction of the African beneath the European plate (Barberi et al., 1974), is known as the 'lighthouse of the Mediterranean' for its persistent eruptive activity word-recognized as "Strombolian" - historically documented since at least 1000 AD (Rosi et al., 2000). Ordinary explosive activity at Stromboli consists of about 8-17 mild, discrete explosions per hour (Calvari et al., 2008; Ripepe et al., 2008), sustained by continuous magma overturning in the shallow conduits (Giberti et al., 1992; Allard et al., 1994, 2008; Harris and Stevenson, 1997). This activity is accompanied by continuous passive degassing (Allard et al., 1994, 2008; Burton et al., 2003, 2009) and puffing every few seconds (Ripepe et al., 1996; Ripepe and Gordeev, 1999; Ripepe et al., 2002; Harris and Ripepe, 2007b; Tamburello et al., 2012; Gaudin et al., 2017a, 2017b). The persistent Strombolian explosions are thought to result from the burst of large over-pressurized gas slugs at the top of the magma column (Blackburn et al., 1976; Wilson, 1980; Patrick et al., 2007; Ripepe et al., 1993, 2001, 2008; James et al., 2009; Taddeucci et al., 2012b; Colò et al., 2010; Del Bello et al., 2012, 2015; Beckett et al., 2014; Gaudin et al., 2014; Leduc et al., 2015; Capponi et al., 2016b). The composition of the explosive gas and ejected materials indicate that slugs are generated at ≤3 km depth and rise rapidly to the surface (Burton et al., 2007a; Métrich et al., 2010). The eruptive activity of Stromboli also includes explosions of more vigorous intensity ("major explosions") that recur over timescales of months/years (Bertagnini et al., 1999; Andronico and Pistolesi 2010; Pioli et al., 2014; Rosi et al. 2006; Giudicepietro et al., 2019), and rarer large paroxysms (Bertagnini et al., 2003; Calvari et al., 2006; Ripepe and Harris, 2008; Aiuppa et al., 2010, 2011; Bonaccorso et al., 2012; Pistolesi et al. 2011; Rosi et al, 2013). Phases of escalating Strombolian activity are known to potentially trigger lava effusion along the Sciara del Fuoco (Ripepe et al., 2005; Burton et al., 2009; Rosi et al., 2006, 2013; Ripepe et al., 2009; Calvari et al., 2011; Valade et al., 2016; Delle Donne et al., 2017; Di Traglia et al., 2018), which may even cause tsunamigenic landslides (La Rocca et al., 2004; Tinti et al., 2005, 2006; Chiocci et al., 2008; Pino et al., 2004, 2009; Pistolesi et al., 2020) with a direct impact on the neighboring inhabited islands, as lastly occurred in December 2002.

Since magmatic gases are the fuel for volcanic eruptions, an improved understanding of volcanic degassing processes at Stromboli is of prime importance for developing robust volcano alert levels and early-warning procedures (Ripepe et al., 2018; Marchetti et al., 2019). Recent technological advancements have allowed monitoring SO_2 flux emissions with finer temporal and spatial resolution (Tamburello et al., 2012; Delle Donne et al., 2017) using the UV Camera technique (see Burton et

al., 2015a for a review; McGonigle et al., 2017). At Stromboli and other similar volcanoes, UV cameras have led to enormous progresses in understanding the links between SO_2 degassing, seismicity (Ripepe et al., 2005; McGonigle et al., 2009; Kazahaya et al., 2011; Tamburello et al., 2012; Waite et al., 2013; Nadeau et al., 2015), infrasound (Dalton et al., 2010; Delle Donne et al., 2016, 2017), and deformation (Saballos et al., 2014; Watson et al., 2000). UV cameras have not only allowed for the estimation of total SO_2 fluxes (Mori and Burton, 2006; Bluth et al., 2007) but have also contributed a better understanding of the various forms of degassing (Mori and Burton, 2009; Tamburello et al., 2012; Delle Donne et al., 2017). Tamburello et al. (2012) studied 130 explosions and 50 gas puffs, discriminating the relative contributions of quiescent (~77%), puffing (~16%) and explosive (~7%) degassing to the total SO_2 gas output, demonstrating that Strombolian explosions usually contribute little to the bulk gas discharge. Delle Donne et al. (2017) reported on a 2-year long SO_2 flux record obtained using UV cameras that, when combined with geophysical observations, allowed characterizing changes in the volcanic SO_2 flux regime prior, during, and after the Stromboli August–November 2014 effusive eruption.

One aspect that has received less attention is if/(and to what extent) degassing activity varies spatially over the Stromboli's crater terrace (see Figure 2.1), and what this spatial distribution can tell us on the geometry of the shallow plumbing system and on the modes/rates of gas and magma ascent in the feeding conduits. It is well known that degassing occurs simultaneously from several vents hosted within the three active craters (North-East crater, NEC; South-West crater, SW; Central crater, CC; Fig. 2.1), but the relative gas contributions from these sources are unconstrained. The three craters are characterized by distinct degassing and explosive regimes (Ripepe et al., 1994; Harris and Ripepe, 2007b; Ripepe et al, 2008), and are therefore likely to contribute differently to the degassing budget. Also, recent effusive eruptions on Stromboli have systematically been preceded by clustering of explosive activity on the more gravitationally unstable NEC (Ripepe et al., 2007; Calvari et al., 2005, 2010, 2011; Neri and Lanzafame, 2009; Valade et al., 2016). The shift of explosive activity and active degassing (puffing) is tracked by locating infrasonic sources (Ripepe and Marchetti, 2002) and it has been observed to anticipate by weeks the 2007 and 2014 flank eruption (Ripepe et al., 2007, 2009; Valade et al., 2016) and by hours most of the small magma overflows occurring from the summit craters (Valade et al., 2016). Ultimately, improving our ability to resolve degassing from different source regions separately is critical to monitoring, and may help to improve our ability to forecast effusive eruptions with direct implication on Civil Protection planning and early warning procedures. This task requires the use of at least two UV cameras located in strategic positions relative to the crater terrace.

Here, we report on SO_2 flux time-series recorded at Stromboli (in the period June 2017–January 2018) using a network of two fully autonomous, permanent UV cameras (Fig. 2.1) that, for the first time, allow resolving SO_2 flux emissions from the northern (NEC) and central-southwestern (SWCC) crater vents. We also use our results to discriminate active (explosions+puffing) vs. passive (quiescent) SO_2 emissions and, by integration with independent geophysical information (infrasonic activity and seismic VLP), to derive new information on gas-magma dynamics in the shallow conduits.

5.2 Instrumental network, data processing, and volcanic activity

Stromboli's current activity takes place within a NE– SW elongated crater terrace composed of three main vent areas (named northeast (NEC), southwest (SW) and central craters (CC)). The terrace is located at an elevation of ~750 m a.s.l. on the upper margin of the Sciara del Fuoco (SdF), a deep horse-shoe depression resulting from several lateral collapses (Fig. 2.1) (Francalanci et al., 2013; Rosi et al., 2013).

Given of the geometry of the crater terrace described above, to separately resolve SO_2 flux emissions from NEC and central-southwestern (SWCC) sectors, we used an ad-hoc designed network of two stand-alone, permanent UV cameras, located at respectively Roccette (38°47'53" N, 15°13'0.1" E; NE upper flank of Stromboli, at 750 m a.s.l.; UV1 in Figure 1) and Valle della Luna (38°47' 28" N, 15°12' 26" E; SW upper flank of Stromboli, at 750 m above sea level; UV7 in Figure 2.1). The two cameras, operative since June 2014 and May 2017 respectively, are both located ~500 m away from the active vents, but allow imagining the crater plume(s) from different viewing directions (Figs. 2.1, 5.1).

The cameras are designed to grant high-rate (0.5 Hz) long-term SO_2 flux observations in continuous mode for 6 hours per day (Delle Donne et al., 2017). The UV camera images are acquired, calibrated and processed automatically by an acquisition/processing module to obtain total SO_2 flux time-series, described in Delle Donne et al. (2017, 2019). A major advantage of these near-vent UV camera observations is that the plume transport speed can directly be derived at high (0.5 Hz) rate from image processing (for details and instrumental specifications, see Delle Donne et al., 2017).

Figures 5.1 A1, B1 show examples of two pseudo-color images of plume SO_2 column densities derived from the processing of UV images taken (in the same measurement day) from respectively UV1 (A1) and UV7 (B1). Visual inspection of the images shows that, for geometrical reasons related to the configuration of the network (relative to the crater area), images taken from UV1 capture well gas emissions arising from the NEC, while they do miss (or, at least, strongly underestimate) emissions from the SWCC, these being (at least partially) hidden by the NEC ridge (Delle Donne et al. 2017). In contrast, UV7 is rightly positioned to fully enclose in the cameras' Field of View (FoV)

the gas plume(s) issuing from the SWCC region, while mostly missing the NEC gas plume (see Fig. 5.1 B1).

The total (active + passive) SO_2 flux time-series we report on here (Fig. 3a) are derived by applying an automatic processing algorithm (see Delle Donne et al., 2017) to data streamed by the two camera systems. Thus, a pre-requisite for further analysis is to verify that these automatically derived SO_2 fluxes do successfully capture (and are thus representative of) emissions from NEC only (UV1) and SWCC (UV7), respectively. In order to validate the automatic processing algorithm, we manually processed, using the Vulcamera software (Tamburello et al., 2011a), image sequences acquired in a set of selected days characterized by optimal measuring conditions (clear sky and well-structured, visible plumes). While manually processing with Vulcamera, care was taken to calculate the SO_2 flux from individual craters by using an integration cross-section located right above each vent area (see Fig. 5.1). This comparison, illustrated for the May 28th example in Figure 5.1, demonstrates excellent agreement between automatically and manually processed data. The latter were deliberately calculated to include the only contributions from the plumes of either NEC (Fig. 5.1 A1) or SWCC (Fig. 5.1 B1). For these reasons, we are confident that the automatically derived fluxes (Fig. 5.2 a) are also representative of distinct crater regions, and can thus allow spatially resolving spatial shift in degassing activity. For example, in the specific May 28th examples, the UV1 automatic fluxes are only 0.2 times lower than the manually derived NEC fluxes, and a similar match (within ~7 %) is observed for UV7 (Fig. 5.1 A2, B2). See Tab. 1 in Appendix for more details.

In addition to the total (active + passive) flux for both NEC and SWCC (Fig. 5.2 a), we used an automatic technique (following Delle Donne et al., 2017) that identifies (and counts) in the SO_2 flux time-series the SO_2 pulses produced by over-pressured gas jets. This SO_2 impulse rate (Fig. 5.2 e) is a proxy for the rate of active SO_2 release via both explosions and puffing. In particular, the largest of these pulses correspond to individual Strombolian explosions, which are recorded by the UV camera

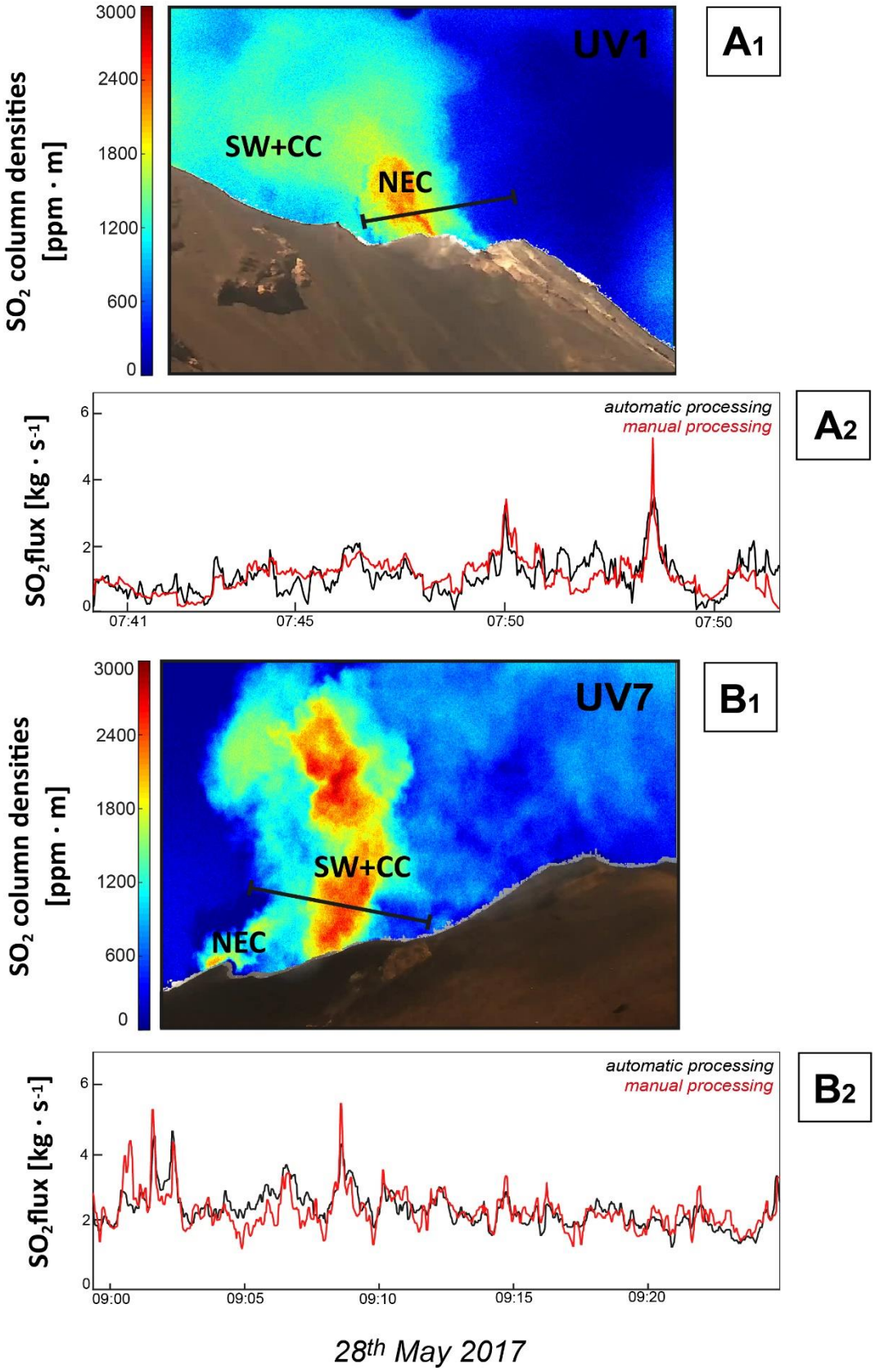

Figure 5.1 *Examples of two pseudo-color images of plume SO_2 column densities derived from processing of UV images taken (in the same measurement day) from, respectively, UV1 (**A1**) and UV7 (**B1**) stations. Images taken from UV1 capture well gas emissions arising from the NEC (**A1**); in contrast, UV7 is rightly positioned to fully capture, the gas plume(s) from the SW+CC region (B1). Plots A2 and B2 shows excellent agreement between automatically and manually processed data (for details see Chapter 2).*

systems as sudden bursts of gas rapidly passing through the cameras' FoV. The same algorithm allows quantifying the mass of each SO_2 impulse and, by combination with the SO_2 impulse rate, the active (explosions + puffing) SO_2 flux (Fig. 5.2 b). Here, we apply the peak-searching algorithm of Delle Donne et al., (2017) to the first derivative of the SO_2 flux, using a fixed threshold of 0.2 kg/s^2 for NEC and SWCC.

The geophysical network run by the Laboratorio di Geofisica Sperimentale (LGS) of the University of Firenze (UNIFI) provided infrasonic and seismic data. We compared the UV Camera-based degassing source locations (Fig. 3d) with those resulting from the infrasonic array detections derived from the EAR array (38°79'39'' N; 15°21'74'' E; elevation of ~870 m; Figure 1), and with seismic signals registered by ROC station (equipped with a broadband seismometer Guralp CMG-40 T, 800 V/m/s with an eigen-period of 30 s), co-located with the UV1 camera system (Figure 2.1). Infrasound is commonly used at Stromboli to locate active degassing, including both puffing and explosions (Ripepe et al., 2007, 2009). Infrasound irradiated during strombolian explosions is thought to be generated by the rapid expansion of overpressure gas at the magma-air interface, and hence is strongly linked to the dynamics and rates of active SO_2 release (Delle Donne et al., 2016). Infrasound data were processed (results in Fig. 5.2 d) following the methodology described in Ripepe and Marchetti (2002) to derive amplitude and direction of the provenance of infrasonic coherent wave fronts generated by active degassing dynamics. Very Long Period (VLP) seismicity was detected by band-pass filtering the cumulative ground displacement in the 0.03–1 Hz frequency band. The VLP seismic rate, reported in Figure 5.2 e, is evaluated by visual inspection of low-pass-filtered seismic records, and no automatic detection algorithm was applied. VLP signals recorded at ROC station (Figure 2.1) were always clearly visible above the seismic noise, being this station located at very close distance (<1 km) from the inferred position of the VLP source (Chouet et al., 2003). VLP signals were characterized by a typical waveform well distinct from other signals (ocean microseism, teleseismic events, etc.). The rate of occurrence of VLP signals is then quickly evaluated on a daily basis. We then used in this work the VLP seismic eventsrate derive fromreported in the LGS daily reports for the analyzed period (lgs.geo.unifi.ithttp://lgs.geo.unifi.it/index.php/reports/stromboli-daily).

During the time interval covered by our observations (June 2017–January 2018), volcanic activity has remained at the "ordinary" Strombolian activity levels, these persisting since the August-November 2014 effusive eruption (Zakšek et al., 2014; Rizzo et al., 2015; Valade et al., 2016; Delle Donne et al., 2017; Di Traglia et al., 2018). Ordinary activity has been temporarily (and suddenly) interrupted by four major explosions on July 26th, October 23th, November the 1st, and December 1st of 2017 (Giudicepietro et al., 2019). The latter event was followed by magma overflown on December 15th from the northern rim of the NEC crater (generating a lava flow that spilled over the

northern slope of the Sciara del Fuoco, SdF). No noticeable change associated with the major explosions was detected in the SO_2 flux record.

5.3 Results

Figure 5.2 a shows our time-series for the daily averaged total (active + passive) SO_2 fluxes, derived from automatic processing of UV1 (=NEC) and UV7 (=SWCC) datasets (data are listed in Supplementary Table S1). The daily averaged SO_2 fluxes exhibit mean values (June 2017–January 2018) of 72±16 t/d (range, 13-155 t/d) for NEC and 52±16 t/d (range 22-87 t/d) for SWCC (Figure 5.2 a). The mean NEC+SWCC daily averaged SO_2 flux is thus 122±16 t/d (range, 47-226 t/d).

Changes in degassing regime and geophysical signals allow dividing the observational interval in 3 different phases: Phase 1 (1 June-1 August 2017), Phase 2 (2 August-3 November 2017), and Phase 3 (4 November 2017-25 January 2018). Based on previous records (Allard et al., 2008; Burton et al., 2009; Delle Donne et al., 2017), we consider the derived SO_2 fluxes as typical of ordinary degassing periods (Phase 1 and Phase 3), intercalated by a phase (Phase 2) of low activity, as evidenced by reduced degassing (Fig. 5.2 a) and seismicity (Fig. 5.2 e) (the concomitant shift in infrasonic activity location - Fig. 5.2 d – is discussed further below). During Phase 1, the daily NEC+SWCC SO_2 flux averages at 170±18 t/d (range, 102-268 t/d), the NEC SO_2 flux averages at 108±8 t/d, and the SWCC SO_2 flux at 62±8 t/d. The NEC SO_2 flux is thus roughly twice as much as higher as the SWCC flux in Phase 1. The NEC (mean 54 t/d; range, 20-96 t/d), SWCC (mean 46 t/d; range, 23-71 t/d) and NEC+SWCC (mean 100 t/d; range, 47-162 t/d) SO_2 fluxes all decline in Phase 2. Interestingly, nearly equal SO_2 flux contributions are observed from NEC and SWCC in this Phase. Finally, degassing activity intensifies again (by a factor 10%) in Phase 3 at NEC (65±9 t/d) and less so at SWCC (46±9 t/d), with the NEC+SWCC SO_2 total flux averaging at 111±9 t/d (range, 47-181 t/d) (Fig. 5.2 a).

We illustrate the relative contributions of NEC and SWCC to the SO_2 budget using the dimensionless ratio R_Φ (Fig. 5.2 c):

$$R_\Phi = (\Phi_{NEC} - \Phi_{SW+CC})/\Phi_{TOT} \qquad (1)$$

where ΦNEC is the daily average SO_2 flux from NEC, ΦSW+CC is daily average SO_2 flux from SWCC, and ΦTOT is the total daily averaged SO_2 flux between NEC and SW+CC.

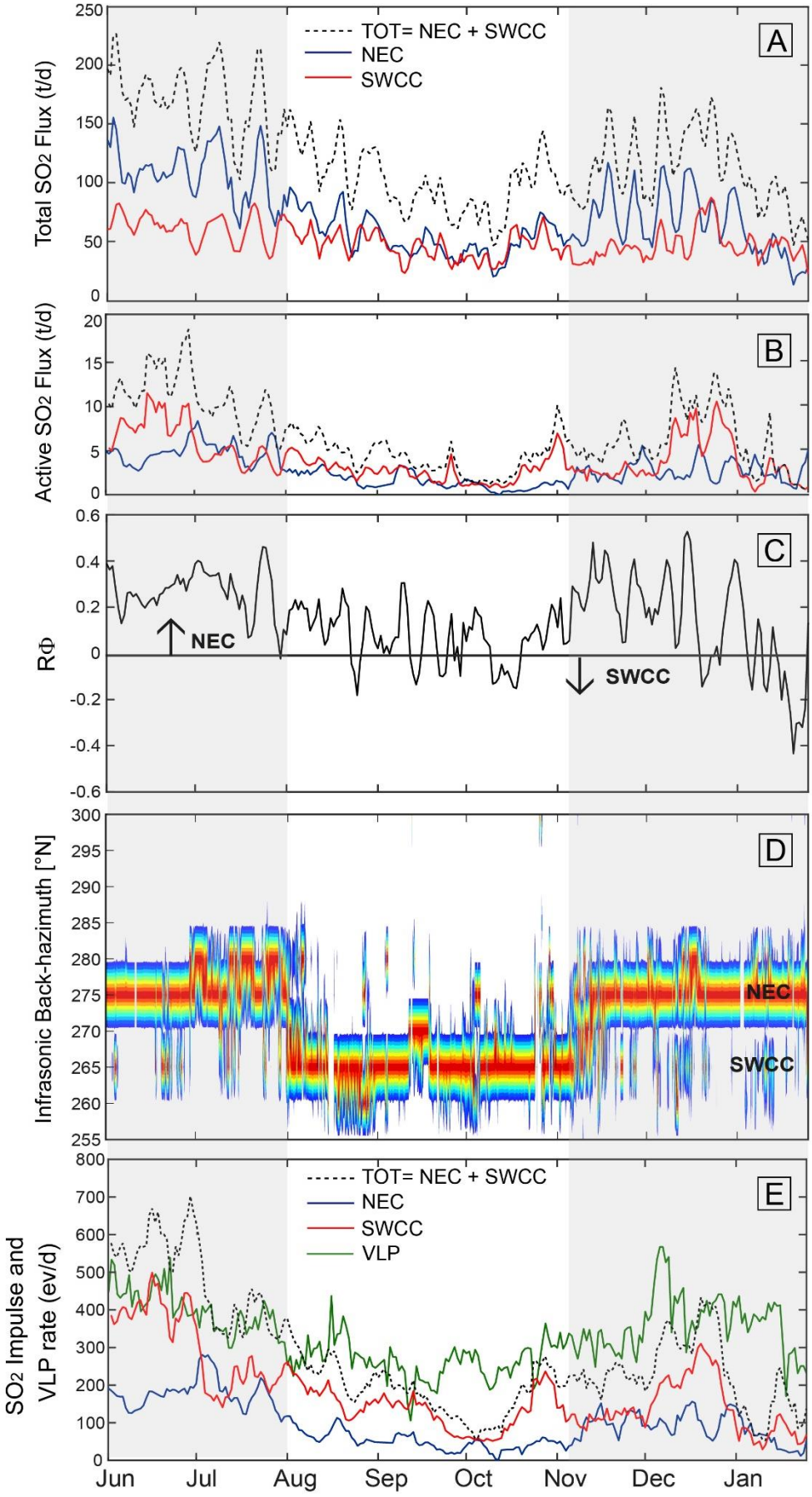

Figure 5.2 *(see Caption details on next page).*

Figure 5.2 *(**A**) NEC, SWCC and Total (NEC+SWCC) daily averaged total (active + passive) SO_2 fluxes time series (blue and red lines and black dashed line, respectively); (**B**) NEC, SWCC and Total (NEC+SWCC) daily averaged active SO_2 flux time series (respectively, blue and red lines and black dashed line); (**C**) Dimensionless ratio (R_Φ between NEC and SWCC: ratio is >0 if NEC emits more SO_2 than SWCC, and it is <0 when/if SWCC is the dominant gas source. R_Φ temporal evolution mimics the total SO_2 flux pattern and puffing location (D); (**D**) Infrasonic source location of puffing activity detected by EAR array; (**E**) NEC, SWCC and Total (NEC+SWCC) daily SO_2 impulse rate (blue and red lines and black dashed line, respectively) produced by over-pressured gas jets and daily VLP seismic rate (green line), evaluated from seismic signals registered by ROC, co-located with the UV1 camera. Changes in degassing regime and geophysical signals show 3 different phases: Phase 1 (1 June-1 August 2017) and Phase 3 (4 November 2017-25 January 2018), marked with gray boxes, higher degassing periods, separated by a Phase 2 (2 August-3 November 2017) of low degassing activity*

Equation (1) implies that R_Φ approaches ~0 when the two vent areas contribute same amounts of gas, it is >0 if NEC emits more SO_2 than SW+CC, and it will be <0 when/if SW+CC is the dominant gas source.

We find that the temporal evolution of R_Φ, Fig. 5.2 c) mimics the total SO_2 flux pattern (Fig. 5.2 a), e.g., $R_\Phi > 0$ (e.g., NEC dominates the gas budget) when the total SO_2 flux increases (e.g., in Phases 1 and 3). Even more importantly, we notice that the major temporal changes in R_Φ correspond to shifts in infrasonic activity source, as illustrated by Figure 5.2 d. Infrasonic activity is mostly irradiated by the NEC area in Phase 1 and 3, while during Phase 2 (when R_Φ~0) is shifted toward a SWCC source area.

The SO_2 impulse rate time-series (expressed as the daily number of SO_2 pulses) is shown in Fig. 5.2e. In total, we identify 12,369 pulses throughout the study period, 3,657 from the NEC and 8,712 from the SWCC. These correspond to mean impulse rates of 227 and 239 pulses for NEC and SWCC, respectively. The SO_2 impulse rate varies widely during the acquisition period, between 1 and 96 impulses/day for NEC and between 1 and 169 impulses/day for SWCC (Fig. 5.2 e). These variations parallel those of the total SO_2 flux (Fig. 5.2 a) and VLP seismicity (Fig. 5.2 e), e.g., the impulse rate is higher in Phases 1 and 3 when the total SO_2 flux and VLP rate are consistently higher.

The daily averaged SO_2 impulse rate (Fig. 5.2 e) is multiplied by the SO_2 mass released daily by the pulses (methodology of Delle Donne et al., 2017) to quantify the active SO_2 flux, in tons/day (see Fig. 5.2 b). We derive active SO_2 flux averages (June 2017-January 2018) of 0-8 t/d (NEC) and 0-11 t/d (SWCC). These results imply that the active SO_2 flux is higher at SWCC than at NEC, but yet substantially lower than the total (active + passive) SO_2 flux (Fig. 5.2 a). We infer that the contribution of active degassing to the total (active + passive) SO_2 budget is 5% on average (Phase 1, 6 %, Phase 2, 5%, Phase 3, 6%), and peaks at values of >15 % during June, October, December 2017 and January 2018 (maximum, 33% during October 3, 2017).

The active/passive degassing ratio:

$$R_{a/p} = \sum_{MASSES=1}^{n} \quad / \quad \sum_{n=1} \quad active\ mass\ /\ \Phi\ mean\ *\ T \qquad (2)$$

in which, Σ *active mass* is the summation of active SO_2 masses, Φ *mean* is the mean SO_2 flux, and T is acquisition duration, consistently averages at 0.04 and 0.08 for NEC and SWCC, respectively, and is overall stable at both craters throughout the entire period of acquisition (Fig. 5.3).

5.4 Discussion

5.4.1 Locating the source of degassing: SO_2 goes with infrasound

At the numerous volcanoes globally that comprise more than one simultaneously active crater, ongoing degassing/eruptive activity is successfully located using infrasound (see for review Johnson and Ripepe, 2011; Fee and Matoza, 2013). This is traditionally achieved by processing data streamed by small aperture infrasonic arrays, that detect the back-azimuth direction of infrasonic wavefronts and, thus, can resolve even closely spaced (tens to hundreds of meters) sources (Ripepe and Marchetti, 2002). At continuously degassing open-vent volcanoes with persistent mild Strombolian activity, such as Stromboli, shift in infrasonic source are explained as due to shifts in magmatic gas bubble flow into, and surface bursting from, the shallow conduits that feed the different active vents/craters (Ripepe et al., 2007, 2009; Marchetti et al., 2009). Infrasound is generally interpreted as an indirect way to monitor the increase in gas flux and where this is located in the crater areas (Ripepe et al., 2008, 2009). However, no direct gas observation exists to corroborate this hypothesis, primarily because traditional networks for remote SO_2 flux sensing (e.g., scanning UV spectrometers) lack the required spatial resolution. The advent of UV camera systems of much improved spatial resolution now paves the way to obtaining this information (e.g., D'Aleo et al., 2016; Delle Donne et al., 2019). Here, we show for the first time that our network of two fully autonomous UV camera stations allows imaging plume emissions on Stromboli from two distinct viewing directions (Fig. 5.1), thus outputting real-time, vent-resolved SO_2 flux emissions over the entire crater terrace (Fig. 5.2 a), and allowing for quantitative understanding of where degassing activity concentrates (Fig. 5.2 c).

Our results (Figs. 5.2 a, c) reveal substantial swing in SO_2 source area in only 8 months of observations (June 2017-January 2018). We find that the NEC and SWCC contributions to the total SO_2 emissions detectably oscillate around the averages of ~64% and ~43%. In particular, the NEC accelerates over the SWCC in Phase 1 (relative contributions, ~63% and ~37% of bulk plume) and, less markedly in Phase 3 (relative contributions of respectively 57% and 43% for NEC and SWCC).

In contrast, the two source areas contribute roughly similar SO_2 amounts in phase 2 (54% and 46% for NEC and SWCC, respectively) (Fig. 5.2 a, c).

Importantly, we show that the relative oscillations in SO_2 emissivity between NEC and SWCC correspond well to shifts in the source of infrasound. Our array records (Fig. 5.2 d) demonstrate a dominant NEC origin for infrasound in Phase 1 and 3, and a shift toward the SWCC source area in Phase 2 (when the NEC SO_2 fluxes consistently drop; Fig. 3a). This good match with well-established infrasonic source location techniques validates our spatially resolved SO_2 flux records (Fig. 5.1; Fig. 5.2 a, c).

The observed correspondence between SO_2-based (Fig. 5.2 c) and infrasound-based (Fig. 5.2 d) source locations, apart from validating further the use of UV cameras in Volcanology (Burton et al., 2015), also opens puzzling questions. The source mechanisms that irradiate infrasound are still not entirely understood, but it is well accepted that excess pressure at source is required to generate the signal (see for a review Johnson and Ripepe, 2011). At Stromboli, this implies that the source mechanism must relate to an active degassing mode (either explosions or puffing; Ripepe et al., 2002, 2007; Harris and Ripepe, 2007b; Delle Donne and Ripepe, 2012). This seems conceptually in contrasts with UV camera records that point to a dominant passive (non-over-pressured) degassing mode (Fig. 5.2 a, Fig. 5.3 a).

One possible explanation is that UV camera time-series underestimate the SO_2 contribution from puffing activity. Puffing at Stromboli is described as the rhythmic (rapid and repeated) emission of small, slightly over-pressurized, discrete gas packages that produce small infrasonic pulses at a rate of one every 1–2 s (Ripepe et al, 1996, 2002; Ripepe and Goordeev, 1999; Harris and Ripepe, 2007a). Although an initial (< 2m high) basal gas trust with ascent velocities of ~8-12 m/s is typically associated with each puff, rapid cooling upon further ascent leads to deceleration and dispersion by buoyancy (at speeds < 4 m/s) after ~2 s from emissions (10 m height above vent) (Harris and Ripepe, 2007a).

Therefore, considering (i) that our UV camera-derived SO_2 emissions are typically retrieved in plume portions some tens of meters above the vent (Fig. 5.1), and (ii) that the identification of active degassing is based upon detecting rapidly rising gas pockets (at speeds well above buoyancy; Tamburello et al., 2012; Delle Donne et al., 2017), we caution that a non-negligible fraction of our passive SO_2 flux corresponds to the upper buoyant (stagnating/slowly dispersing) portion of the puffs. The correlation between the temporal fluctuations of total (passive + active) and active SO_2 flux (Fig. 5.2 c) corroborate this hypothesis.

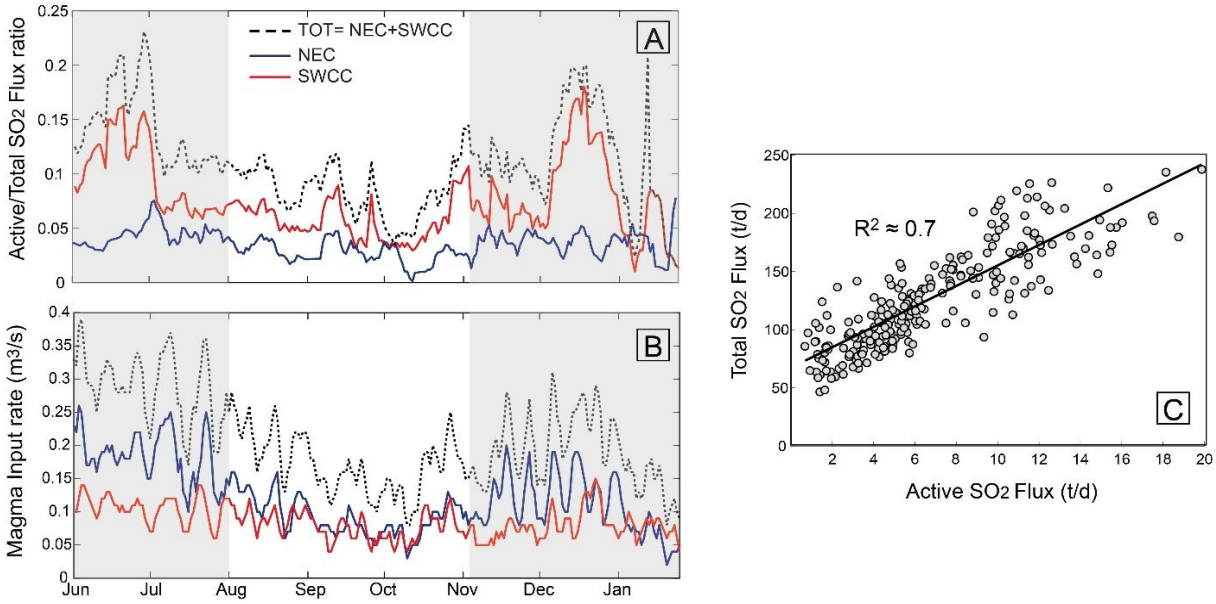

Figure 5.3 *(**A**) NEC, SWCC and Total (NEC+SWCC) active/total SO_2 flux ratio (respectively, blue and red lines and black dashed line). See text for details. Gray boxes marked Phase 1 and Phase 3, typical of ordinary degassing periods, interrupted by a Phase 2 of low degassing activity; (**B**) NEC, SWCC and Total (NEC+SWCC) daily magma input rate (m^3/s) (blue and red lines and black dashed line, respectively) calculated following the methodology of Allard et al., (1994, 2008); (**C**) Scatter plot of total (NEC+SWCC) daily averaged total (active + passive) SO_2 flux time-series vs. total (NEC+SWCC) daily active SO_2 flux time-series that highlights statistically significant correlation (R^2 ~0.7) during the observational period implying passive and active degassing are linked.*

5.4.2 Active vs. passive degassing activity

One major advantage of UV cameras is that, because of their high temporal resolution, allow identifying the rapid, transient SO_2 burst produced by active degassing (explosions and puffing). Our results imply a minor contribution of active degassing to the total (active + passive) SO_2 budget on Stromboli (Fig. 5.2 a, e; Fig. 5.3 a), and are the first to resolve active vs. passive emissions at the scale of individual craters. We find that active degassing during June 2017-January 2018 contributes ~5% of the emitted SO_2 on average, and is more critical at the SWCC (~9 %) than at the NEC (~4 %) (Figs. 5.2 e and 5.3). This larger SWCC "explosivity" is further corroborated by the higher and more oscillating SO_2 impulse rates at this crater (Fig. 5.2 e). We caution, however, that a) the data series of SWCC is much shorter than that of NEC, so the higher percentage of explosivity of the former should be further evaluated; b) our automatic processing may only be accounting for the largest SO_2 pulses (Fig. 5.2 e), e.g. from those arising from the Strombolian explosions and the most massive puffs. At the same time, they may fail in resolving the majority of the puffs from the background passive plume (cfr. Fig. 5.3 a). For example, the manually processed results of Tamburello et al., (2012), yet based on a far smaller dataset, imply a larger active flux contribution

(23%, 16% of which from puffing and 7% from explosions). Our temporal trends in the SO_2 impulse rate (Fig. 5.2 e) match well the seismic (VLP) rate (Fig. 5.2 e), again supporting a dominant modulation from the explosions and the interpretation of the seismic VLP activity as controlled by the gas flux (Ripepe et al., 2005; Delle Donne et al., 2017).

One important aspect we bring here to light is the statistically significant (R^2 ~0.7, Fig. 5.3 c) correlation between the total (active + passive) and active SO_2 flux during the observational period. This correlation implies that passive and active degassing are commonly modulated. For istance, active degassing forms (explosions and puffs) become more frequent (Fig. 5.2 d, e), and contribute more SO_2 (Fig. 5.2 a), when the passive SO_2 flux increases, as in the case of Phases 1 and 3 (Fig. 5.2 a). The non-zero intercept is perhaps a further hint for the active SO_2 flux being under-estimated, especially at low total SO_2 fluxes. The active/passive ratio (Fig. 5.3 a) thus remains constant at both NEC (~0.04) and SWCC (~0.08): an explosivity increase corresponds to an equal passive flux increase.

The total (active + passive) SO_2 flux on Stromboli (Allard et al., 1994, 2008), and at any other open-vent volcano (Shinohara, 2008), is thought to be controlled by the rate of convective magma transport in the shallow (< 3 km) plumbing system (Harris and Stevenson, 1997; Bonaccorso et al., 2008). This degassing-driven shallow magma convection process is operated by fresh (gas-rich) magma ascent that continuously replaces viscous and degassed magma sinking back into the conduit (Shinohara, 2008). This mechanism helps to explain the observed excess SO_2 degassing (Allard et al., 2008), the longevity of Strombolian activity (Rosi et al., 2013), and the overall homogeneity of magma chemistry (Bertagnini et al., 2008). We follow the methodology of Allard et al. (1994, 2008) to convert the total (NEC+SWCC) SO_2 flux (Fig. 5.3 a) into a magma input (degassing) rate time-series (Fig. 5.3 b).

$$\text{MIR } [m^3/s] = \frac{\left(\frac{S_{\,[g/mol]}}{SO_{2\ [g/mol]}}\right) * SO_2 \text{ Flux } [kg/s]}{(S_0\ [\text{wt. }\%] * \rho\ [kg/m^3] * \text{cristallinity } [\%])}$$

Where MIR indicates the magma input rate in m^3/s, S and SO_2 are atomic and molecular weights, SO_2 flux in kg/s, S_0 is initial sulfur content (0.18 wt. %), ρ is magma density (2700 kg/m3) and crystallinity (30 %) in Stromboli.

To this aim, we use our measured SO_2 flux values (120-180 t/d), an initial sulfur content in Stromboli magmas of 0.18 wt. %, a density of 2700 kg/m^3 and 30% crystallinity (Métrich et al. 2010). Our derived magma input rates range between 0.3 and 0.2 m^3/s (Fig. 5.3 b), and are highest in Phases 1 and 3, when active degassing and VLP seismicity are also more intense (Figs. 5.2 e). In a constant geometry (conduit radius) scenario (likely in the "stable" Stromboli 2017 conditions), any change in

magma input (convection) rate would mainly be controlled by changing magma rheology, and especially by varying the density difference between non-degassed (ascending) and degassed (sinking) magmas (Stevenson and Blake, 1998; Shinohara, 2008). This latter in turn mostly depends on the gas bubble content of the non-degassed magma, an increase of which would drive to both faster convection and escalating explosivity (Fig. 5.4), therefore explaining the relationship between total and active flux, observed here (Fig. 5.3 c). In this interpretation, Stromboli swings in between high (Phase 1 and Phase 3) and low (Phase 2) activity periods, depending on the bubble-rich or bubble-poor nature of the ascending magma (Ripepe et al., 2002).

5.4.3 Degassing activity clustering at the NEC

Our results also point to a mechanism in which periods of total SO_2 flux increase (Phases 1 and 3) correspond to escalating degassing activity at NEC, while the SWCC flux exhibit a more stationary behavior (Fig. 5.2 a, c). The concomitant shift in infrasound back-azimuth directions toward the NEC (Fig. 5.2 d) fits well with a process of gas bubble channeling toward the NEC, since infrasound source is thought to coincide with the section of the feeding conduit more fluidized by gas (Ripepe et al., 2007, 2009; Landi et al., 2011). These combined observations thus suggest that any increase in shallow magma transport is preferentially channeled toward the NEC (Fig. 5.4) as suggested also by the change in infrasound location occurring before the effusive eruption (Ripepe et al., 2009).

The northeastern portion of Stromboli's crater terrace corresponds to a prime structural weakness zone of the volcano, as testified by geological information (Francalanci et al., 2013), geo-structural constrains (i.e. Tibaldi et al., 2001; Corazzato et al., 2008; Acocella et al., 2016), slope failure and ground deformation data (Tarchi et al., 2008; Tommasi et al., 2008) and geophysical datasets (Chouet at al., 2003; Ripepe et al., 2005; Marchetti et al., 2008). Magma accumulation (Ripepe et al., 2015, 2017) and cone growth in the gravitationally unstable NE crater sector is know to trigger flank instability (Valade et al., 2016), opening of lateral vents, and onset of tsunamigenic lava effusion in the Sciara del Fuoco (Bonaccorso et al., 2003; Rosi et al., 2013; Di Traglia et al., 2014). As such, the ability of our UV camera permanent network to spatially (vent-to-vent) resolve any magma input rate increase (Fig. 5.3 b) adds to existing geophysical knowledge (Ripepe et al., 2008, 2009, 2015) that help forecasting transition from ordinary to effusive activity, with obvious implications for volcanic risk mitigation.

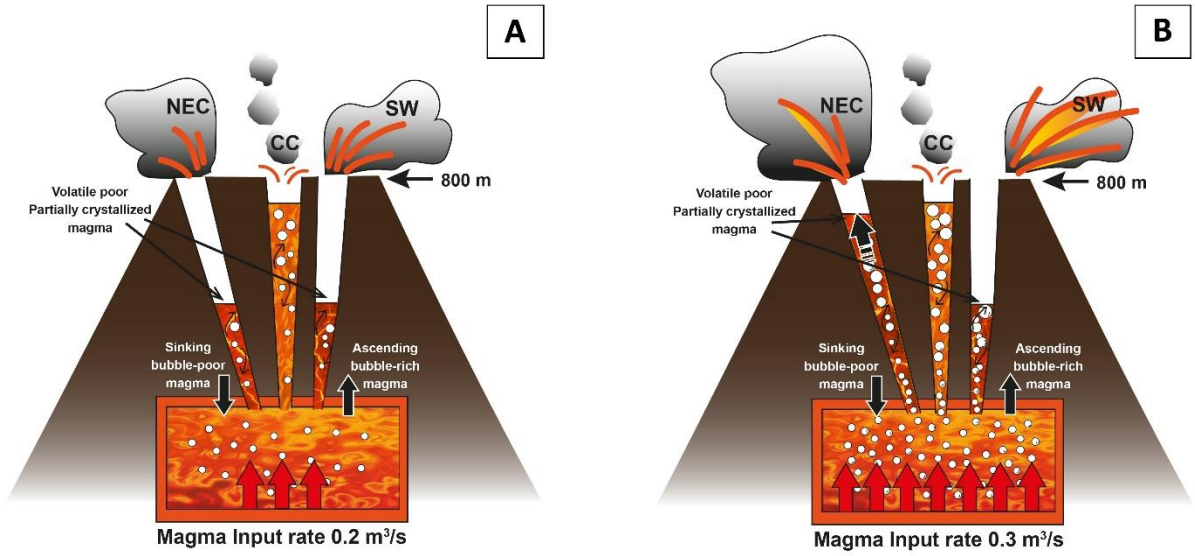

Figure 5.4 *Sketch of Stromboli degassing-driven shallow magma convection process in which changes in magma input rate is especially controlled by varying the density difference between fresh gas-rich ascending and degassed gas-poor sinking magmas. An increase in gas bubble content would drive to both faster convection and escalating explosivity (**B**). In this interpretation, Stromboli would swing in between low (**A**) and high (**B**) activity periods in agreement to low or high magma input rate. Moreover, our results point to a process of gas bubble channeling preferentially toward the NEC in periods of total SO_2 flux increase (Phases 1 and 3) that correspond to escalating degassing activity at NEC (see Figure 5.4), while the SWCC SO_2 flux exhibit a more stationary behavior.*

5.5 Conclusions

Our first vent-resolved SO_2 fluxes emissions at Stromboli, interpreted in tandem with infrasonic and seismic measurements, help better characterizing temporal shift in degassing along the crater terrace. Our results indicate that, at least in the studied period, the ordinary activity oscillates between (i) high activity phases, when both total and active SO_2 fluxes are higher, and concentrated at the NEC, and (ii) low activity phases, when SO_2 emissions are lower and equally distributed in between NEC and SWCC. We demonstrate that these fluctuations in the total SO_2 flux are driving most of the changes we observe in the parameters recorded on the volcano. We show how high SO_2 fluxes are related to higher VLP seismicity rate and thus to higher explosive rate whereas during lower SO_2 emission VLP seismicity decreases and explosions become less frequent and less SO_2-rich. These fluctuations likely reflect temporal changes in the gas bubble cargo of the feeding magma in the shallow conduits. Temporal records of SO_2 fluxes, captured at high spatial and temporal resolution by automated UV cameras, allows to "live" monitoring degassing activity, thus contributing to understanding (and potentially predicting) changes in volcanic activity style.

– *Results Chapter 6* –

"Understanding SO_2 behavior during Stromboli's major explosions"

Lo Coco E., Delle Donne D., Aiuppa A., Bitetto M., Ripepe M., Tamburello G. *"Understanding SO_2 behavior during Stromboli's major explosions"* (in prep.)

Abstract

As other persistent open-vent activity of basaltic volcanoes, strong and hazardous major explosions periodically interrupt Stromboli volcanic activity. The rapid transition from quiescence degassing/weak ordinary explosive activity to these kind of high energetic explosive eruptions poses a significant challenge for volcanic hazard evaluation and mitigation.

Here, making use of the high spatial resolution of UV-cameras, we resolve SO_2 emissions from Stromboli craters of two major explosions occurred on 1st November 2017 and 24th April 2018, respectively from CC and SW/CC craters. Here, for the first time, SO_2 budget and magma volumes of a major explosion are estimate. We measured SO_2 masses of ~2.6 x 10^3 kg and ~0.24 x 10^3 kg, corresponding to magma volumes of 382 and 36 m^3, for 1 November 2017 and 24 April 2018 major explosions, respectively. Moreover, for each major explosions, we detail the SO_2 flux of the explosive sequence from the beginning to final degassing coda and correlate it with thermal signal and volcanic tremor. Correlation between SO_2 degassing and volcanic tremor amplitude suggests shallow gas supply under over-pressurized conditions and constrains very shallow source location for volcanic tremor. We infer that degassing dynamic can be also an important source of tremor. Our inferences bring new achievements for understanding the seismic source process itself and the volcanic degassing system of Stromboli, and even infer some implications that may also apply to other open-conduit basaltic volcanoes. Our interdisciplinary analysis of SO_2 degassing and volcanic tremor highlights considerable constraints on degassing mechanism of gases ascending to the surface and producing seismic waves and brings new insights showing that the interdisciplinary correlation between geochemical and geophysical data is the key to a better understanding of the degassing dynamics.

The largest dataset ever measured before including 3655 ordinary explosions allowed to investigate the possible existence of a relation between ordinary and major explosions at Stromboli. We adopt a statistical approach by using SO_2 mass, as a parameter describing their magnitude, in function of the frequency of occurrence of the explosions. We notice that power law distribution of Strombolian ordinary explosions does not fit the two major explosions analyzed here. This suggests that ordinary and major explosions at Stromboli are not driven by the same magma degassing dynamics inside Stromboli conduit(s). Hence, we might infer that major explosions are something other than the Strombolian explosions. Our calculated SO_2 mass for major explosion implies a time occurrence of an explosion every ~94 days. Our results allow to understanding a challenging relation of low and high-energy explosive events in Stromboli with an important impact in terms of volcanic monitoring.

Keywords: Major explosions, Explosive degassing, Stromboli, UV camera, SO_2 flux, volcanic monitoring

6.1 Introduction

Stromboli has long puzzled volcanologists because of the persistence of its normal explosive activity over many centuries. Such a state reflects an unusual steadiness of the volcanic and magmatic plumbing system in which continuous cooling and degassing is somehow compensated by a supply of heat and gas from below. The fact that the lava level inside conduits remains unchanged through time also means that the mass of lava ejected by explosions is replaced by a corresponding supply of magma from below. The eruptive activity of Stromboli includes ordinary (Strombolian) explosions and explosions of more vigorous intensity (called "major explosions"). Ordinary activity consists about 8-17 mild, discrete explosions per hour (Calvari et al., 2008; Ripepe et al., 2008) yielding gas jets 100-200 m high (Barberi et al., 1993), and throwing out scoriae, lava lumps, ash and blocks up to heights of a few tens to hundreds of meters, which fall in the vicinity of the craters (Bertagnini et al., 2003). Major explosions recur over timescales of months/years (Bertagnini et al., 1999, 2003; Andronico and Pistolesi 2010; Pioli et al., 2014; Rosi et al. 2006; Giudicepietro et al., 2019) ejecting meter-sized bombs and blocks within a distance and height of several hundreds of meters from the craters and reaching a plume height >200 m (Andronico and Pistolesi, 2010; Barberi et al., 1993). Rarer large paroxysmal explosions also occur (Bertagnini et al., 2003; Calvari et al., 2006; Aiuppa et al., 2010, 2011; Bonaccorso et al., 2012; Pistolesi et al. 2011; Rosi et al., 2013). During such episodes, plume column can reach 4 km high (Rosi et al., 2006) and showers of incandescent scoriae and bombs, and meter-sized ballistic lithic blocks fall within a distance of several kilometers from the craters, eventually reaching the two villages, Stromboli and Ginostra, located on the coast (Bertagnini et al., 2003).

Detailed petrological investigations have led to the conclusion that Stromboli paroxysmal explosions were produced by the rapid ascent and decompression of batches of gas-rich, low porphyric (LP) basaltic magma, erupted at the surface as highly vesiculated "blond" pumice, from a 7–10 km (below summit vents) deep magma storage zone. In contrast, the source mechanism of the "major" explosions is not yet understood, even though these are far more frequent and, therefore, potentially even more hazardous than paroxysmal events.

Major explosions share the possibility of emitting not only High Porphyritic (HP) black scoriae but also brownish to yellow pumice clasts (commonly called 'golden pumice') associated with the rise of a deeper gas-rich, Low Porphyritic (LP) magma (e.g. Bertagnini et al., 2003; Métrich et al., 2005, 2010; D'Oriano et al., 2011).

According to Allard (2010), major explosions should be heralded by increasing leakage of CO_2-rich gas as the bubble foam approaches instability (Jaupart and Vergniolle, 1989), and the magnitude of each explosion should be proportional to its source depth or/and the stored gas amount (Aiuppa et al., 2011). Bubble coalescence at depth is required to generate the large gas pockets or slugs whose fast ascent, followed by bursting, drives the periodic Strombolian-type explosions (Burton et al., 2007a) and probably the intermittent major explosions as well (Allard, 2010).

Irrespective of the terminology and notwithstanding the recent studies having dealt with the volcanological, geophysical and petrological characterization of higher energy events at Stromboli (Bertagnini et al., 1999; Calvari et al., 2005; Carniel et al., 2006; D'Auria et al., 2006; Rosi et al., 2006; Andronico et al., 2008; Landi et al., 2008; Pistolesi et al., 2008; Ripepe and Harris, 2008), the classification of Stromboli explosive events in separate categories (i.e. ordinary explosions, major, small-to-large scale paroxysms) is still an open discussion, thus making fundamental the documentation of each single event. We believe that the study of paroxysmal and major explosions is the key to understanding the characteristics and dynamics of the feeding system. A full understanding of how Stromboli magmatic dynamic works is also of paramount importance. Achieving this goal, identifying the trigger mechanism of paroxysmal and major explosions, would improve the short-term forecasting capability of Stromboli's surveillance system. This has important implications in the mitigation of volcanic hazard because major and paroxysmal explosions represent the main threat for the numerous visitors to the volcano.

Although trigger mechanisms of major explosions are still unclear today, magmatic gas phase is the driving force for such events, as for ordinary and paroxysmal explosions. The recent advent of UV cameras is paving the way to direct observations and quantification of gas fluxes from individual gas explosions (see Burton et al., 2015, for a review). Nowadays, UV camera permanent network makes available a largest dataset ever measured before (Delle Donne et al., 2017; D'Aleo et al., 2019; Delle Donne et al., 2019). Here, making use of the high spatial and temporal (0.5 Hz) resolution of UVcameras, we resolve SO_2 emissions from Stromboli craters of 3655 ordinary explosions and analyze in detail the SO_2 fluxes of two major explosions occurred on 1st November 2017 and 24th April 2018, respectively from CC and SW/CC craters.

Gas release events, interpreted as a 'coda', could be due to the magma disturbance generated by the explosion (Capponi et al., 2016). At Stromboli, the South-West vents ('author' of 24th April 2018 major explosion) often produced longer and more complex infrasonic signals, with a low-amplitude compressional pulse followed a longer coda, modelled as the bursting of smaller bubbles at the surface or longer mass discharge processes (McGreger and Lees, 2004; Ripepe et al. 2008).

Volcanic tremor is observed worldwide on the majority of active volcanoes and is associated with eruptive processes (e.g. Chouet, 1996; Falsaperla, 1998, 1999). Tremor wavefield is quite stationary for long period of time and has been generally described as characterized by surface waves with low energy content, concentrated in a narrow frequency range (0.5-6 Hz) (McNutt, 1989).

Correlations between SO_2 outgassing and seismic amplitude were observed at several volcanoes: e.g. at Mt. Etna (Salerno et al., 2018), Soufrière Hills, Montserrat (Young et al., 2003), Villarrica (Palma et al., 2008), Yasur (Bani and Lardy, 2007), Kilauea (Nadeau et al., 2015) and Fuego Volcano, Guatemala (Nadeau et al., 2011).

Such studies indicate that, though tremor and degassing are somewhat coupled, the nature of their relationship, as well as the source mechanism for tremor, are still poorly understood. It is likely that several processes are involved in the generation of volcanic tremor from gas and magma flows making the unraveling of the tremor and degassing relationship challenging.

Specifically at Stromboli, analysis of seismic records combined to infrasonic signals revealed that shallow volcanic tremor could be associated to magma degassing. This process appears on infrasonic records as low pressure (< 1 Pa) pulses generated at 1-2 s rate, which have been considered a result of the bursting of small gas pockets at the magma free-surface (Ripepe et al., 1996).

Although magnitude–frequency distributions provide some of the most basic and important information to understanding explosive eruption processes, investigations of the statistical characteristics of volcanic explosions are limited in number (specifically, volcanic explosions earthquakes, Nishimura et al., 2016). Here, we present the first study of the magnitude–frequency distribution characteristics of SO_2 explosive masses of more than 3650 ordinary explosions, the largest dataset ever measured, and of the two major explosions aforementioned. This study allowed us to understanding a challenging relation of low and high-energy explosive events in Stromboli with an important impact in terms of volcanic monitoring.

6.2 Methods

SO_2 flux data belonging to 1 November 2017 major explosion are detected from UV7 camera station, sited on south-west upper flank of Stromboli, at 750 m above sea level (Figure 3.1), operative since May 2017 and located ~500 m away from the active vents. The Field of View (FoV) of UV7 camera station is focused on south-western crater plume(s). SO_2 flux data belonging to 24 April 2018 major explosion are detected from UV1 camera station, sited on north-east upper flank of Stromboli, at 750 m above sea level (Figure 3.1), operative since June 2014 and located ~500 m away from the active

vents. The FoV of UV1 camera station is focused on north-eastern crater plume(s) (Figure 3.1). For technical and processing data details see Sections 3.4. The reported SO_2 fluxes are compared with seismic and thermal signals. Volcanic tremor is detected by a network, run by the Laboratorio di Geofisica Sperimentale (LGS) of the University of Firenze (UNIFI), consisting of 5 seismo-acoustic stations (ROC, PZZ, STR, SCI, SDK) each equipped with broad-band seismometer (GMT-30T, 800 V/m/s and an eigen period of 30 s). Thermal signal is recorded by ROC station, run by LGS. Thermal data are derived from a FLIR-A20 thermal camera (for specific technical details see Section 3.5).

For both major explosions, we measured SO_2 flux time duration (s), explosive SO_2 flux (kg/s), and SO_2 mass (kg) (Figures 6.1 and 6.3). Furthermore, we used thermal signal ($T_{expl\text{-}th}$) recorded by ROC thermal camera (Ripepe et al., 2009) to measure total duration of solid ejection. Explosive time duration is expressed as temperature peak related to the emission of incandescent material (ash and bombs) detected by thermal camera lasting from explosion onset (t_0) to rapid cooling down to a background temperature.

We identified three phases within SO_2 flux record: pre-explosive, explosive and post-explosive (Figures 6.1 and 6.3). SO_2 fluxes sampled at 0.5 Hz allowed us to characterize time evolution of explosive degassing dynamics and also to obtain a cumulative mass associated with event. We measured explosion duration evaluating the time at which SO_2 fluxes return to pre-explosive levels. (Figures 6.1 and 6.3).

The SO_2 mass from each explosion is calculated by integrating the flux time series over the entire duration, after removing for the background SO_2 flux value (*BF, 'background flux',* the time the flux time series returns to its pre-pulse value).

We compared these SO_2 masses associated with these two major explosions with SO_2 masses associated with other 3655 weaker explosions occurred from June 2017 to January 2018, by the same UV1 station. These masses associated with ordinary explosions are calculated using an automatic technique that identifies (and counts) the SO_2 pulses in the SO_2 flux time series (Delle Donne et al., 2017). This algorithm is able to distinguish the largest SO_2 flux pulses corresponding to the rapid ascent, within the camera FoV, of over-pressurized gas jets released by Strombolian explosions, from a nearly constant gas emission originated from quiescent degassing and an impulsive gas contribution (SO_2 flux pulses) related to explosions and puffing activity. Then, we characterized duration and amplitude of these 3655 explosive events in the SO_2 flux record. Such pulses can be identified in a time series as local maxima above a fixed threshold, having a fast ramp and a slower waning phase (Delle Donne et al., 2017). In order to resolve pulses associated with explosions from other slower pulses ones rather related to fluctuation in passive degassing, we apply the peak searching algorithm

to the first derivative of the SO_2 flux, using a fixed threshold of 2 kg/s^2 which was identified by a trial and error technique aimed to retrieve the best signal to noise ratio within the time series. Once duration and peak flux are identified, explosion masses are then calculated by integrating flux time series over pulse duration and subtracting the background SO_2 flux value. Pulse duration is calculated as the time interval from pulse onset to termination (e.g., *BF, 'background flux'*) (Figure 3.6, Delle Donne et al., 2017).

We correlate SO_2 outgassing with volcanic tremor. Volcanic tremor amplitude is calculated from raw traces recorded at station, by averaging within a 1-minute length window the maximum RMS amplitude taken within a 1-second long-time window.

In order to investigate the possible existence of a relation between ordinary and major explosions at Stromboli, we adopt a statistical approach by using SO_2 mass, as a parameter describing their magnitude, in function of the frequency of occurrence of the explosions. To do this, we first evaluate if our data of daily explosions frequency in relation to their mass follows a power-law probability distribution. Hence, we divide the explosions masses in constant ranges (bins) of about 3.5 kg that are calculated considering the highest mass values (176 kg) divided for an established number of classes (in our case 50). Then, we counted the number of explosions occurred in each bin and plot in a histogram versus the average mass of each bin (Figure 6.1b). It has to be considered that the total number of explosions measured during our observation period (243 days) is 3655.

Then, we filter for the lowest values of mass that approximate to zero, and plot versus the average value of mass for each identified class in a linear and log-log plot (Fig. 6.1a and 6.1b). In the linear plot, we notice a high skew and asymmetry of the distribution (Fig. 6.1a). Once we defined the exponent b of the power-law distribution, we can calculate the constant C, and the p(x) for each bin. Then, we plot the bins (explosions mass ranges) versus p(x) in a semi-log scale and found a straight line (Fig.6.2).

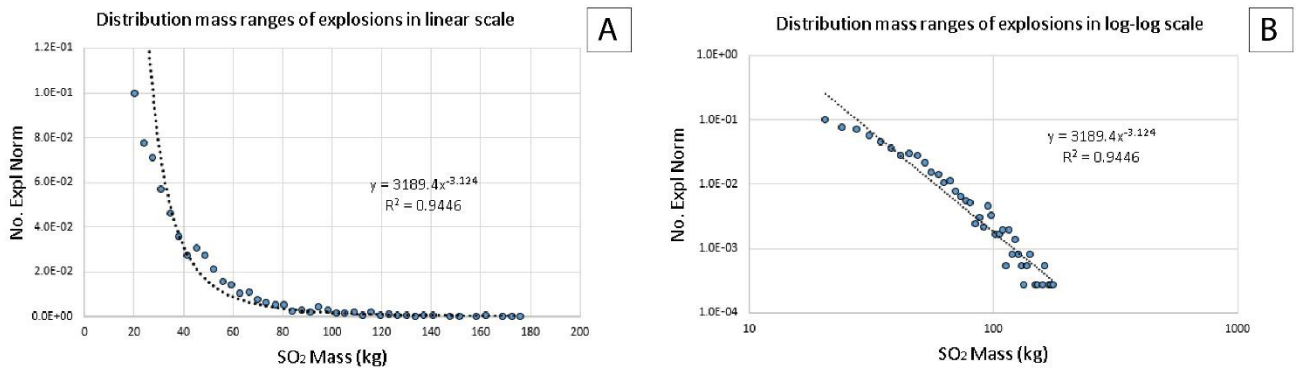

Figure 6.1 *Distribution of SO_2 explosive mass ranges of 3655 ordinary explosions divided in 50 bin (see Figure 6.1b) in linear scale (**a**) and in log-log scale (**b**).*

Finally, we summed the number of explosions counted for each bin and then divide for the observation period and consider that explosions are now grouped in 50 bins of mass range. We obtain the daily number of explosions for a mass > x (Daily events M>Mx), which can be plotted versus the SO_2 mass (Figure 6.9).

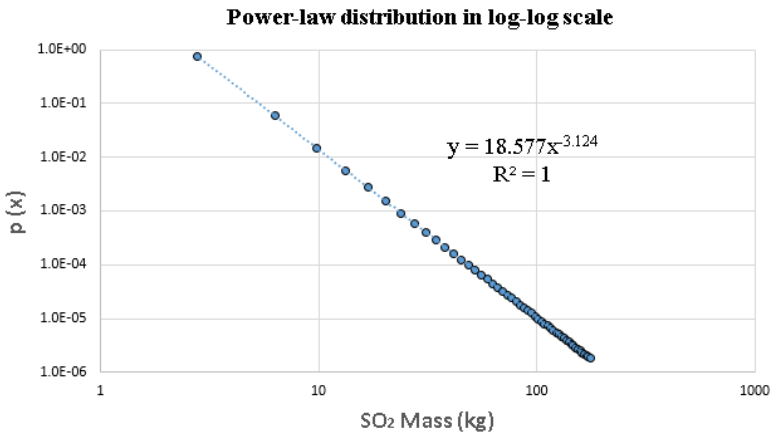

Figure 6.2 *Power law distribution of SO_2 masses of ordinary explosions (see Text for details).*

6.3 Results

Major explosions of 1st November 2017 and 24th April 2018 caused an abundant emission of incandescent material that escaped from the field of view of the UV camera and then fell outside the crater terrace.

SO_2 fluxes recorded during these two major explosions allowed us to calculate total emitted SO_2 masses of ~2.6 x 10^3 kg and ~0.24 x 10^3 kg, respectively (Figures 6.3 and 6.5).

SO_2 flux peaks at the onset of the explosions of 1st November 2017 and 24th April 2018, reaching ~12 kg/s and 2 kg/s and returns to pre-explosive value after 1129 and 953 seconds, respectively. SO_2 gas speed of 1st November 2017 major explosion is measured of ~11 m/s on the average during the explosion and remained far above pre-explosive levels of 2 m/s for the entire duration of the explosion (Figure 6.3).

We found that duration of SO_2 degassing is ~16-18 minutes longer than duration of solid emission, captured by thermal record (Figures 6.4 and 6.6).

Pre- and post-explosive SO_2 flux speed of ~0.74-2 m/s (Figures 6.3 and 6.5) suggests an enhanced degassing process associated with major explosions continuing also far after the end of main solid emission (Figures 6.4 and 6.6).

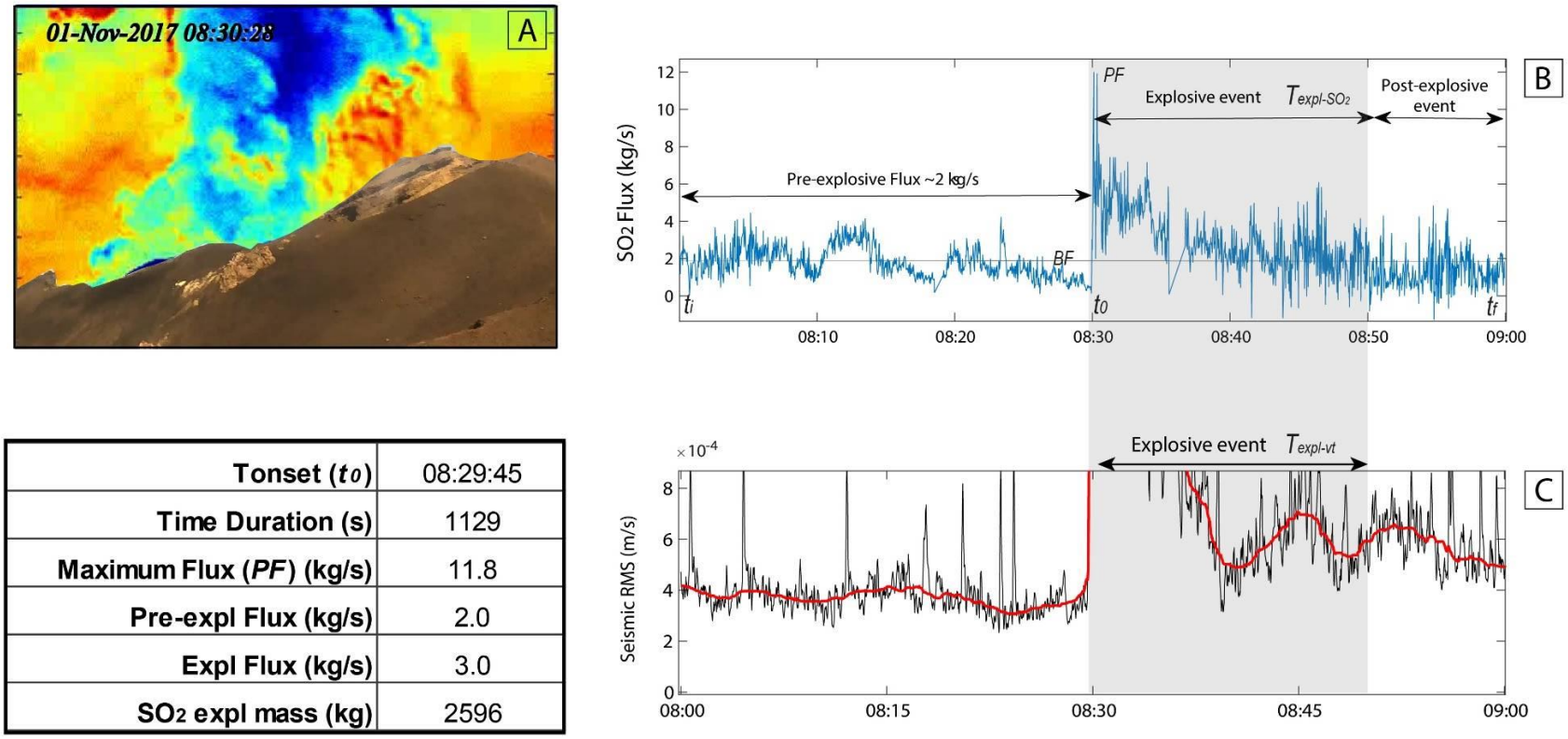

Tonset (t_0)	08:29:45
Time Duration (s)	1129
Maximum Flux (*PF*) (kg/s)	11.8
Pre-expl Flux (kg/s)	2.0
Expl Flux (kg/s)	3.0
SO_2 expl mass (kg)	2596

Figure 6.3 *(**a**) Absorbance image of the onset of 1 November 2017 major explosion; (**b**) SO_2 flux measurements distinguished into pre-explosive, explosive and post-explosive event. Time evaluation in which SO_2 fluxes return to pre-explosive levels (BF) allows to measure the explosion duration ($T_{expl-SO2}$). Pre-explosive event is characterized by persisting SO_2 flux around 2 kg/s from initial time (t_i) to explosion onset (t_0). Post-explosive SO_2 flux event returns to background value measured on pre-explosive event. Explosive SO_2 mass (2596 kg) is calculated by integrating the flux time series over $T_{expl-SO2}$ after de-trending it for the background SO_2 flux value (BF, 'background flux'). (Enhanced SO_2 degassing duration is also associated with a relatively high amplitude tremor phase (**c**). The very long SO_2 flux explosive event ($T_{expl-SO2}$) of 1 November 2017 explosions is related to continuing volcanic tremor lasting the same time duration ($T_{expl-vt}$).*

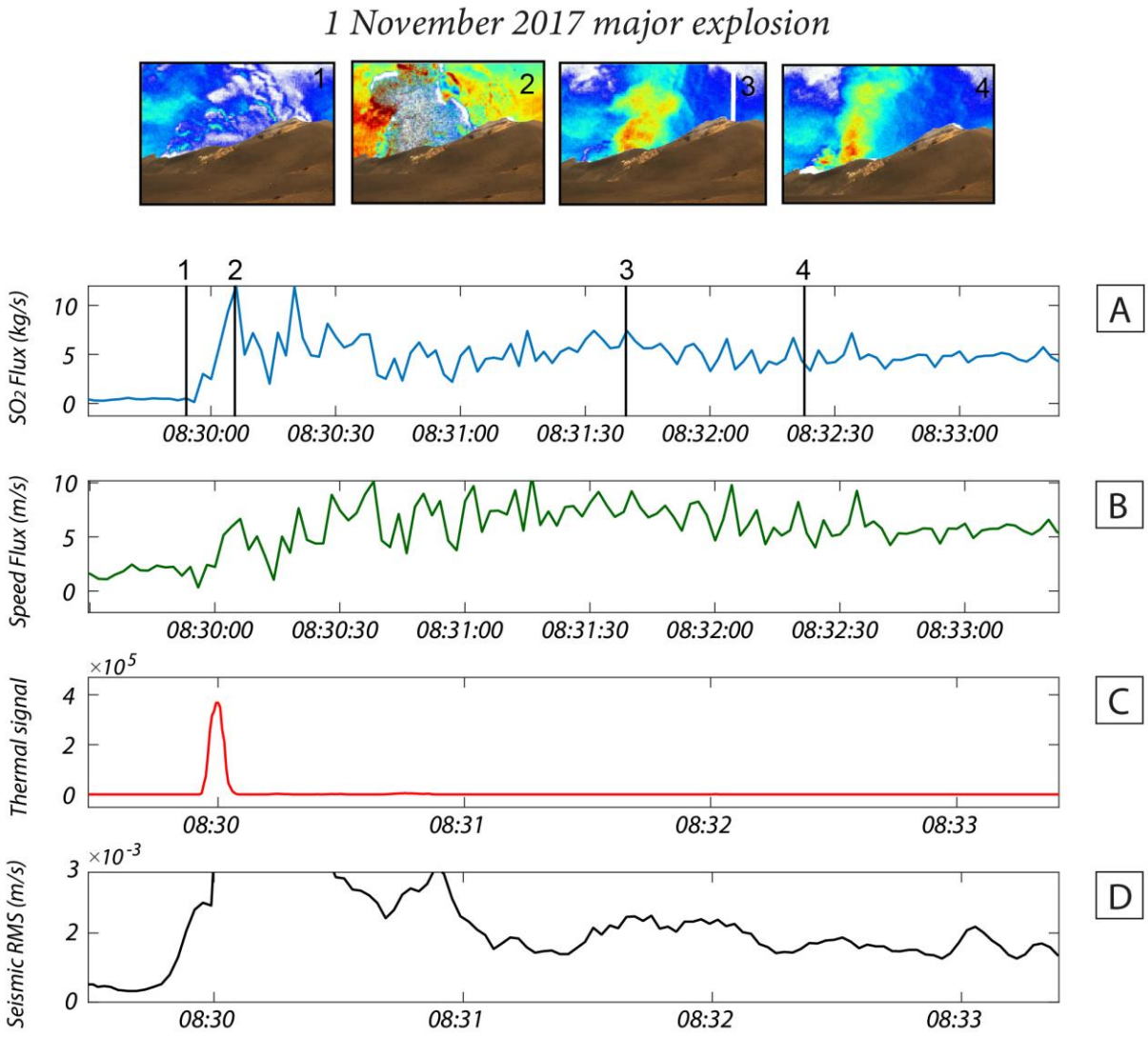

Figure 6.4 *(**a**) 1 November 2017 zoom of SO_2 flux (kg/s) during explosive phase correlated with thermal signal (**c**) and seismic RMS (m/s) (**d**). Explosive time duration measured by UV camera ($T_{expl\text{-}SO2}$) is much longer than thermal duration (T_{th}) of ~9-10 s related to the emission of incandescent material detected by thermal camera. Pre-and post-explosive SO_2 flux speed (**b**) suggests an enhanced degassing process associated with major explosions continuing also far after the end of main solid emission producing a thermal signal (**c**) implying a not necessarily association of active degassing to the emission of juvenile material. Elevated gas release (**a**) for several minutes after the main blast occurs in overpressure condition and is associated with elevated tremor amplitude (**d**), implying that SO_2 active degassing was still ongoing after the blast although the emission of juvenile material (**c**) was apparently ceased.*

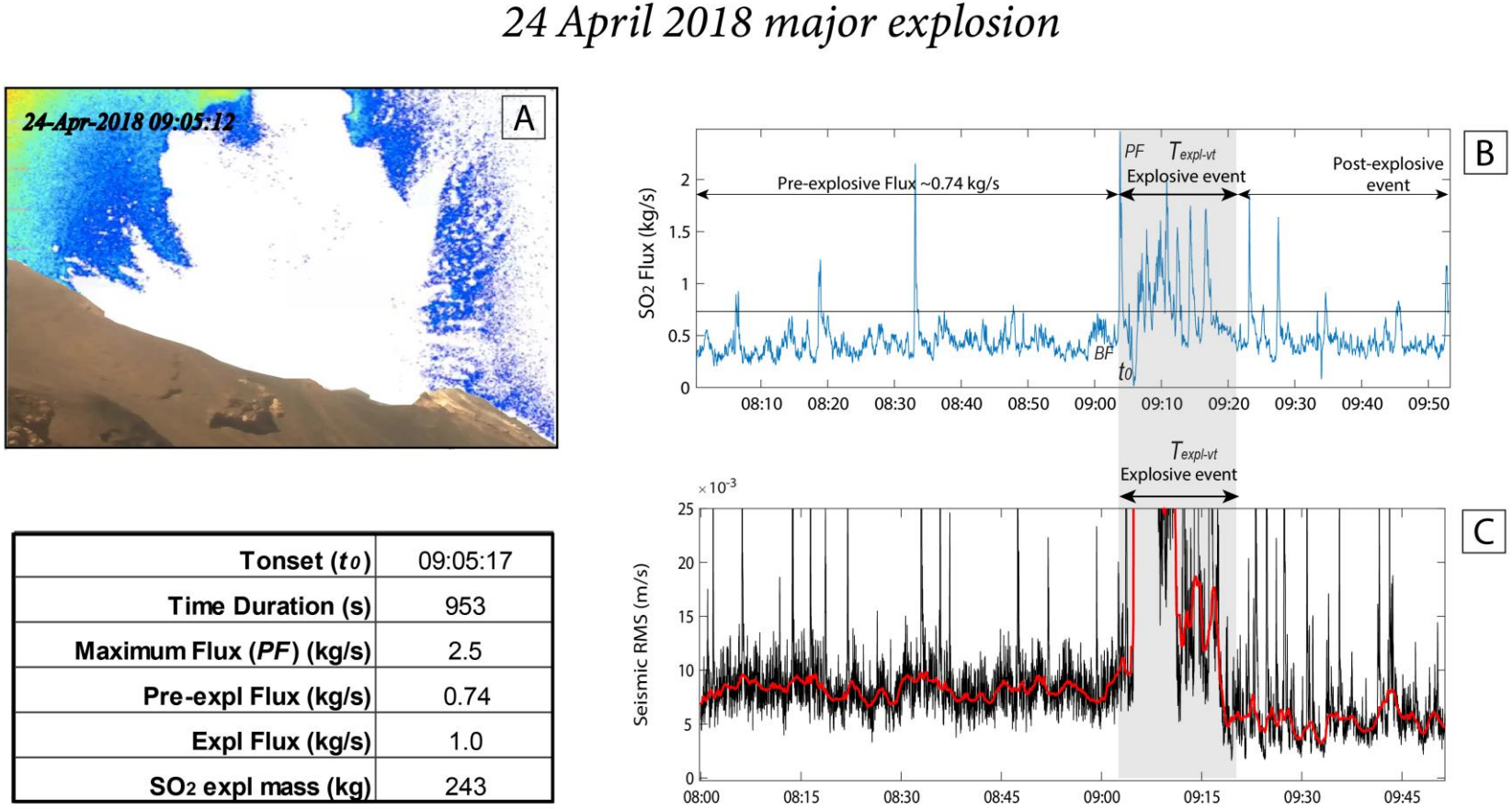

Tonset (t_0)	09:05:17
Time Duration (s)	953
Maximum Flux (*PF*) (kg/s)	2.5
Pre-expl Flux (kg/s)	0.74
Expl Flux (kg/s)	1.0
SO_2 expl mass (kg)	243

Figure 6.5 *(**a**) Absorbance image of the onset of 24 April 2018 major explosion; (**b**) SO_2 flux measurements distinguished into pre-explosive, explosive and post-explosive event. Time evaluation in which SO_2 fluxes return to pre-explosive levels (BF) allows to measure the explosion duration ($T_{expl-SO2}$). Pre-explosive event is characterized by persisting SO_2 flux around 0.74 kg/s from initial time (t_i) to explosion onset (t_0). Post-explosive SO_2 flux event returns to background value measured on pre-explosive event. Explosive SO_2 mass (358 kg) is calculated by integrating the flux time series over $T_{expl-SO2}$ after de-trending it for the background SO_2 flux value (BF, 'background flux'). Enhanced SO_2 degassing duration is also associated with a relatively high amplitude tremor phase (**c**). The very long SO_2 flux explosive event ($T_{expl-SO2}$) of 24 April 2018 explosions is related to continuing volcanic tremor lasting the same time duration ($T_{expl-vt}$).*

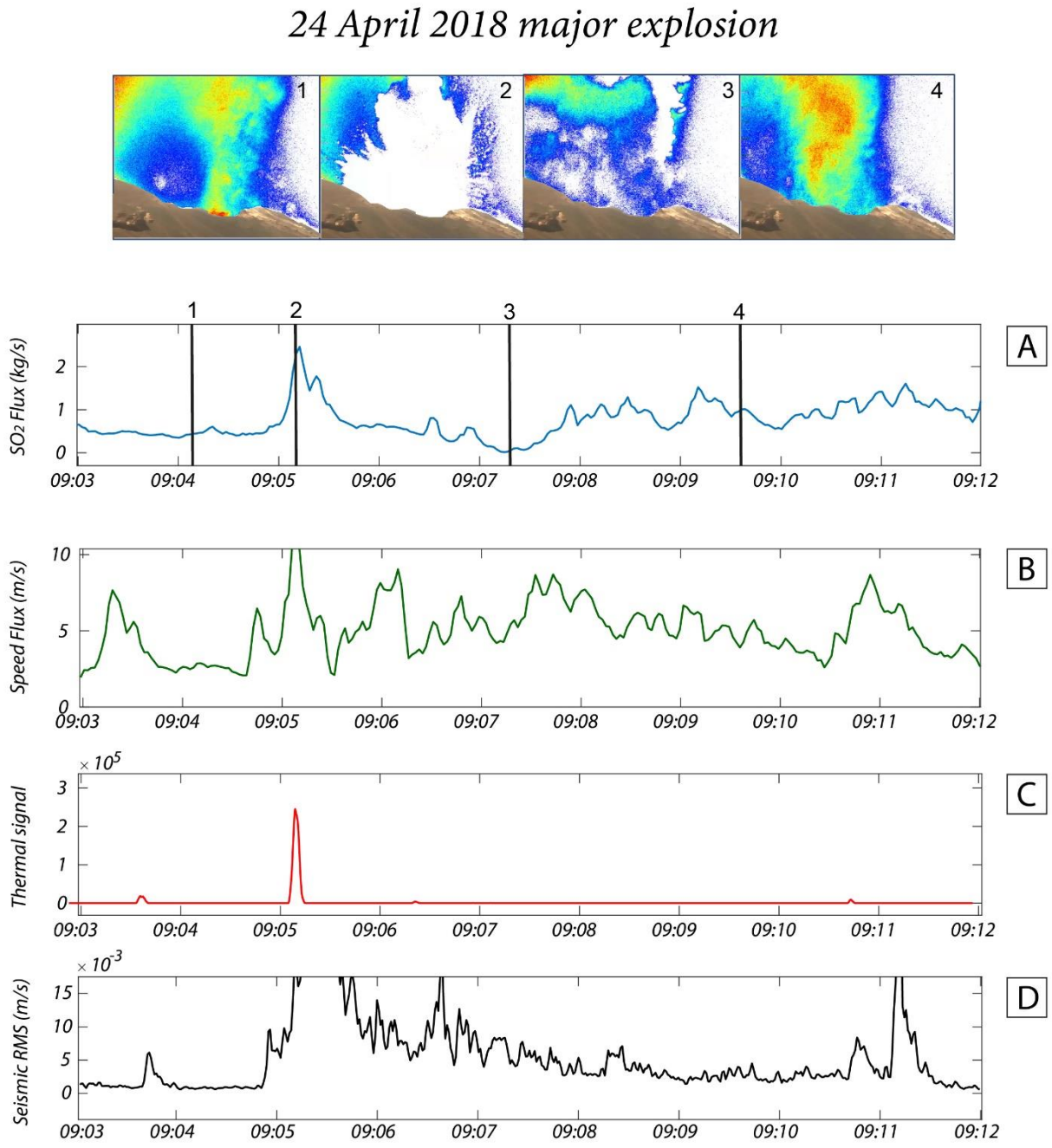

Figure 6.6 ***(a)*** *24 April 2018 zoom of SO_2 flux (kg/s) during explosive phase correlated with thermal signal* ***(c)*** *and seismic RMS (m/s)* ***(d)****. Explosive time duration measured by UV camera ($T_{expl\text{-}SO2}$) is much longer than thermal duration (T_{th}) of ~9-10 s related to the emission of incandescent material detected by thermal camera. Pre-and post-explosive SO_2 flux speed* ***(b)*** *suggests an enhanced degassing process associated with major explosions continuing also far after the end of main solid emission producing a thermal signal* ***(c)*** *implying a not necessarily association of active degassing to the emission of juvenile material. Elevated gas release* ***(a)*** *for several minutes after the main blast occurs in overpressure condition and is associated with elevated tremor amplitude* ***(d)****, implying that SO_2 active degassing was still ongoing after the blast although the emission of juvenile material* ***(c)*** *was apparently ceased.*

We outline that 24 April 2018 major explosion is characterized by a high ash concentration and ballistic during the first minute of eruption which may have prevented a reliable measurements during the main gas-thrust phase of explosion. Then, our measurements would correspond to a lower boundary estimate of the real SO_2 emitted mass. Nevertheless, we assume they may be equally representative of SO_2 explosive output considering that gas-thrust phase is short. Furthermore, we point out that we not consider 1 November 2017 major explosion SO_2 mass underestimated because ash presence only in the first seconds after onset explosion.

Degassing durations are measured of ~19 minutes and 21 s and 16 minutes for the 1 November 2017 and 24 April 2018, respectively (Figures 6.3 and 6.5). These durations are much longer than total solid and thermal emission as recorded by thermal signal ($T_{expl\text{-}th}$) of about ~9 seconds, for both major explosions (Figures 6.4 and 6.6), pointing to an enhanced degassing dynamic following the main thrust phase. It is worth noting that enhanced degassing duration is also associated with a relatively high amplitude tremor phase, and the suggesting degassing mechanisms is somehow linked with tremor source (Nadeau et al., 2011; Figures 6.3 and 6.5).

SO_2 explosive masses of the two major explosions are compared to 3655 ordinary explosions measured during May 2017-January 2018 for 243 acquisition days. These have an average SO_2 mass of 28 kg (range 1-178 kg; Figures 6.7a and 6.7b). In our dataset, we record 2740 ordinary events with an SO_2 mass mean of 17 kg and 8 ordinary events with an SO_2 mass mean of 125 kg. Figure 6.7a shows the comparison between ordinary and major explosions SO_2 masses. 1 November 2017 major explosion, in terms of SO_2 mass, is significantly higher than the former (Figure 6.7a). Explosive events frequency range from 370 explosive events corresponding to SO_2 masses of ~10 kg and a single event per day for SO_2 masses >168 kg (Figure 6.7b).

Figure 6.7a shows the distribution of SO_2 mass range of 3655 ordinary explosions dividing in 50 bins in relation of number of explosions normalized. In Figure 6.5b, we observe a straight line, although the right-hand end of the log-log distribution is noisy due to statistical errors. By applying a least squares regression, we find that a power equation well fits our dataset (R^2=0.95) and gives the value of the exponent (b) of this equation (3.124) (Fig. 6.1). Before applying the power-law distribution equation ($p(x) = C\ x^{-b}$) in order to estimate the probability distribution, we calculate a C constant value equal to 18.6. As expected, in semi-log plot explosions mass range versus p(x) (Figure 6.2), the highest distribution probability of explosions at Stromboli in function of the explosive mass is found for the lowest mass values. In Figure 6.9, in contrast, we notice that data distribution of Strombolian ordinary explosions clearly does not fit the two major explosions, which fall outside at sensibly higher values of mass.

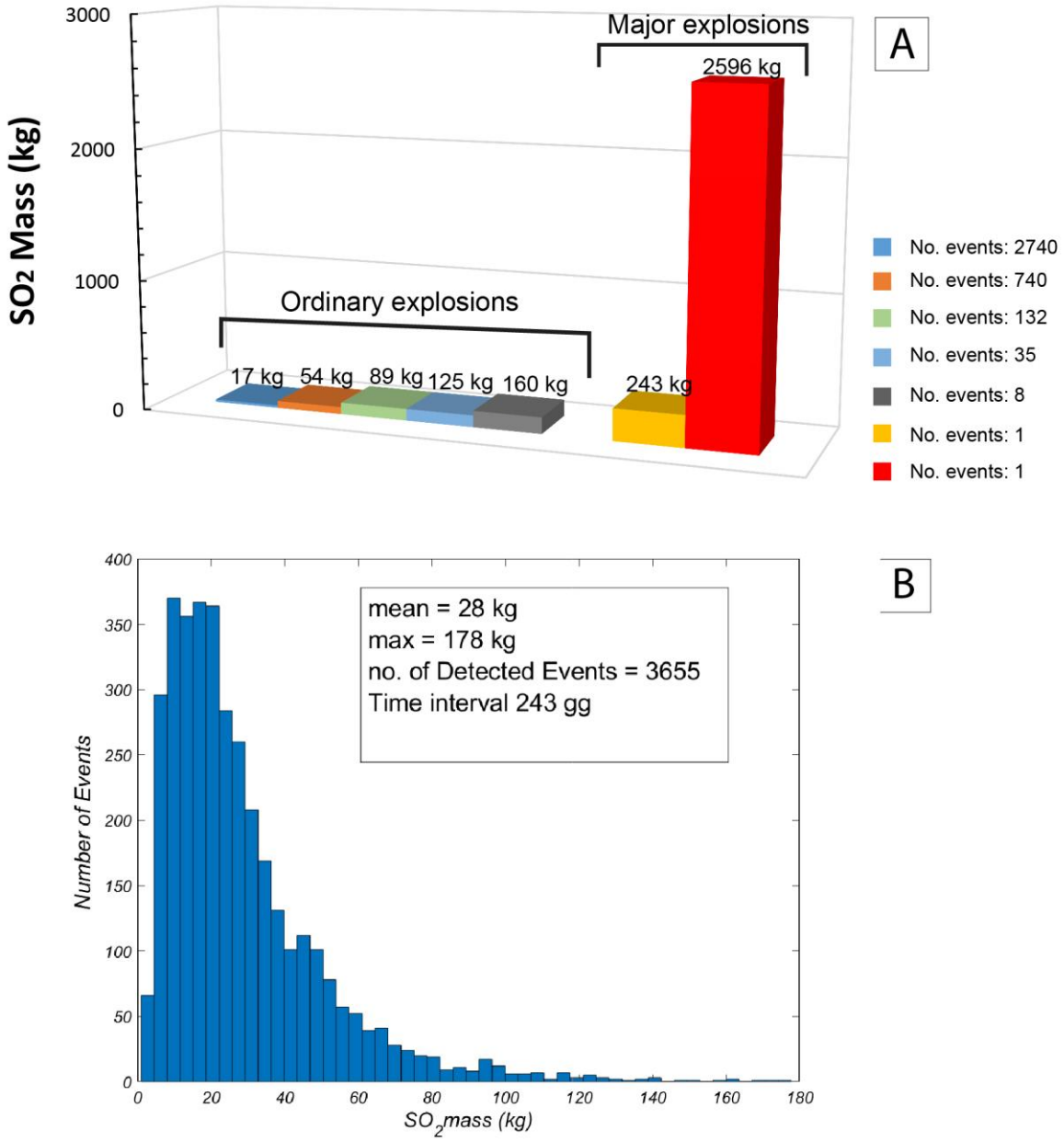

Figure 6.7 ***(a)*** *Histogram showing the different in SO_2 explosive masses between ordinary explosions and major explosions. SO_2 masses of 3655 ordinary explosions are calculated applying 'peak-finder' algorithm (see Section 6.2 for details) on May 2017-January 2018 SO_2 flux measurements. Major explosions SO_2 masses are calculated by integrating the SO_2 flux time series over the entire duration after de-trending it for the background SO_2 flux value (BF, 'background flux') (see Figures 6.1 and 6.3). n.b. SO_2 mass of 24 April 2018 major explosion could be underestimated because ash presence in the first minutes of our UV camera measurements.* ***(b)*** *Histogram of 3655 ordinary explosions detailed into 50 bins of SO_2 mass. This ranges between 1-178 kg (mean 28 kg).*

6.4 Discussion

6.4.1 SO_2 degassing, volcanic tremor and thermal signal

As other persistent open-vent activity of basaltic volcanoes, strong and hazardous major explosions periodically interrupt Stromboli volcanic activity. The rapid transition from quiescence degassing to these kind of high energetic explosive eruptions poses a significant challenge for volcanic hazard evaluation and mitigation. Improving our understanding of the processes that trigger these major events is crucial. Although magmatic gas is definitely the driver, direct measurements of a major explosion's gas flux budget have remained challenging, to date.

1 November 2017 and 24 April 2018 major explosions are characterized by an high SO_2 flux ($T_{expl\text{-}SO2}$) lasting ~16-20 minutes, and SO_2 masses of ~2.6 x 10^3 kg and ~0.24 x 10^2 kg (Figures 6.3 and 6.5). 1 November 2017 major explosion is ~1 order of magnitude higher than ordinary explosions in terms of mass (Figure 6.7a). SO_2 mass of 24 April 2018 major explosion is 'apparently' comparable to ordinary explosions because could be underestimated owing to ash presence in the first minutes of our UV camera measurements. Hence, it must be considered as a minimum value. The elevated gas release for several minutes after the main blast occurs in overpressure condition and is associated with elevated tremor amplitude, implying that SO_2 active degassing was still ongoing after the blast although the emission of juvenile material ceased apparently.

The dynamics of an eruptive column can be divided into a gas thrust and buoyant phase (e.g. Wilson and Self, 1980). The initial gas thrust phase is dominant during the early stage of the eruption, when over-pressurized gas is released and drives the cloud rapidly upwards. The buoyant phase will be dominant during the later stage of the eruption when the velocity decelerates to a constant buoyant velocity, resulting in a slower convective motion of the hot gas and ash mixture (Wilson and Self, 1980).

The fast ramp observed in explosive phase of these two major explosions is more likely related to gas burst of over-pressurized gas at the magma free surface and slower ones, visible on post-explosive phases (Figures 6.3 and 6.5), are related to fluctuation in passive degassing that follows gas buoyancy state (e.g. Wilson and Self, 1980; Patrick et al., 2007). Therefore, our results show a dominant active (over-pressurized) degassing mode, as totally representative of explosive SO_2 gas output for a major explosion. Studies on Strombolian explosions are based on observations of a stationary flux component during the explosive events. These typically show a post-explosive coda of enhanced passive degassing, with no associated seismic signal (Tamburello et al., 2012; Pering et al., 2016). Our results point out to active SO_2 emission also during the explosive degassing coda. SO_2 flux of the two analyzed major explosions return back to pre-explosive value, hence showing passive degassing, only after ~16-20 minutes.

Explosive SO_2 output, after the initial burst, occurs without a significant simultaneous emission of eruptive material (ash and ballistic). Explosive time duration measured by UV camera ($T_{expl\text{-}SO2}$) is much longer than thermal duration (T_{th}) of ~9-10 s related to the emission of incandescent material (ash and bombs) detected by thermal camera (Figures 6.4 and 6.6). Our results suggest that the emission of ash and ballistic, detected by thermal camera only during gas-thrust phase, is followed by an increased active degassing measured by UV camera indicating that active degassing is not necessarily associated with considerable emission of juvenile material.

The very long SO_2 flux explosive event ($T_{expl\text{-}SO2}$) of 1 November 2017 explosions is related to continuing volcanic tremor lasting the same time duration ($T_{expl\text{-}vt}$) (Figures 6.3 and 6.5). Time duration of high degassing phase after the explosion coincides with the duration in which volcanic tremor remains high after the explosion, also on a higher level than the pre-explosive phase. The observed correlation between SO_2 emission rates and volcanic tremor indicates that the generation of the seismic tremor and the rise and fall of SO_2 flux rates originate from the same source process (Nadeau et al., 2011). Previous works confirmed the long-held belief that there is a link between a rising gas slug and tremor (Chouet et al., 2003; Nadeau et al., 2011). However, the mechanism is still highly unconstrained and, e.g., Nadeau et al. (2011) inferred that it could be caused by the oscillation of bubbles, a resonance in the conduit, the movement of the magma or the coalescence of bubbles.

Our results of combined SO_2 fluxes and volcanic tremor suggest a very remarkable evidence that the latter is linked to the degassing process directly from Stromboli craters. The main source of seismic energy producing volcanic tremor has to be related to the degassing process of magma (Ripepe and Gordeev, 1999). Our results broaden evidences on sources of volcanic tremor suggesting that the source of tremor associated with major explosions has a component closely linked to shallow degassing on the surface (Ripepe et al., 1996; Ripepe and Gordeev, 1999)

We notice that volcanic tremor is related to the SO_2 degassing process from vents and, hence, over-pressurized degassing produces it. This consideration is outstanding for a better understanding of shallow volcanic tremor. Volcanic tremor is connected to a process whereby a constant depressurization induces bubbles growth in the magma and this, in turn, induces a pressure decrease, at date (Ripepe et al., 2009).

Therefore, we infer that volcanic tremor source in initial phase is linked to pressure decrease processes (Ripepe et al., 2009), and also to syn-eruptive phase, in which gas bubbles burst, at the top of free magma surface, causes a degassing which is itself source of volcanic tremor. Moreover, the persistence of volcanic tremor suggests that goes on to exist a gas supply such as to allow this continuing process.

Post-explosive high amplitude volcanic tremor, also on a higher level than the pre-explosive phase, could derive from a "sum" of seismic tremor signal deriving from the viscoelastic reaction processes of the magma (Ripepe et al., 1999) to which is added that deriving from the continuous bursting of gas bubbles.

Our interdisciplinary study of SO_2 degassing and volcanic tremor highlights considerable constraints on degassing mechanism of gases ascending to the surface and producing seismic waves and brings new insights showing that the coupled correlation between geochemical and geophysical data is the key to a better understanding of the degassing dynamics.

6.4.2 Major explosions are not larger ordinary explosions

Major explosions are currently unpredictable and thus raise dramatic issues to volcano hazard management and pose still unanswered questions to volcanologists: what are the trigger mechanisms for such events? (Aiuppa et al., 2011). What is recurrence time that might allow us to predict them?

Major explosions occurrence rate has been quantified to be 1-4 per year (Aiuppa et al., 2011; Bertagnini et al., 1993; Di Traglia et al., 2013). This occurrence rate in the last years changed drastically. During 2017-2018, eight major explosions occurred (Figure 6.8) and, specifically, four within our analysis period (June 2017- January 2018): 26th July, 23rd October, 1st November and 1st December 2017 (Giudicepietro et al., 2019). Two of these could not be analyzed because they occurred outside acquisition time of UV cameras. These major explosions succeeded within relatively short intervals. Such a clustering in their occurrence suggests a common source process or instability in the plumbing system.

We calculate the volumes of degassing magmas required to produce the inferred erupted SO_2 masses (e.g., the magma volume necessary to provide the gaseous content to drive them) of the 3655 ordinary Strombolian events and of 1 November 2017 and 24 April 2018 major explosions included in our dataset. For the former, we considered the minimum, maximum and mean values of SO_2 masses. In order to convert the SO_2 masses (MSO_2) into volumes of magma (Ve) needed to justify them, we use the same relation as in Allard (1997):

$$Ve = \frac{MSO_2}{2 \cdot [S] \cdot r \cdot (1 - x)}$$

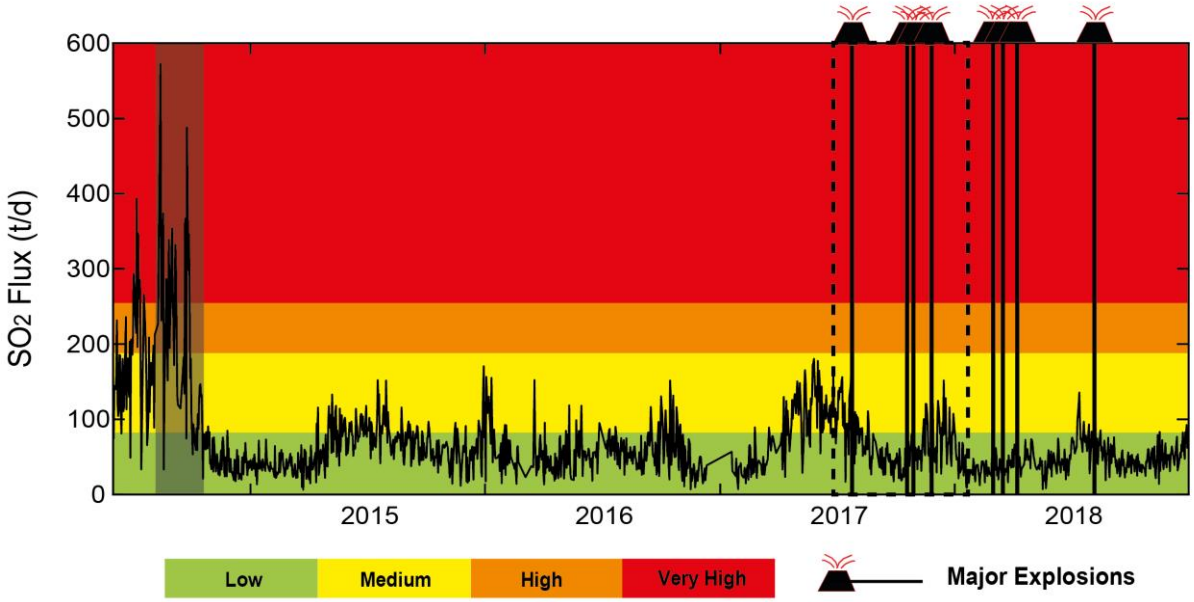

Figure 6.8 *SO_2 fluxes (t/d) encompassing 2014 effusive eruption (grey box) and 4 years of 'regular' ordinary activity. This is interrupted by eight major explosions. (box in black dashed line indicates our observational period). N.b. Investigation of major explosions is focused on two of these (1 November 2017 and 24 April 2018) because others occurred out of UV camera network acquisition time.*

where [S] is the weight fraction of elemental sulfur degassed per unit mass of magma (0.0018 wt%, from melt inclusion record; Métrich et al., 2010), *r* is typical basalt density (2700 kg/m^3) and *x* is magma crystallinity (0.3; Métrich et al., 2010).

Minimum, maximum and mean magma volumes calculated for the 3655 Strombolian explosions recorded during our observation period are 0.15, 4 and 26 m^3, respectively.

Therefore, these calculated values can be only compared with the volume of erupted products during Strombolian, major and paroxysmal explosions. However, we point out that it is not expected and correspondence between the volume of magma feeding the explosions and the products effectively erupted.

These values are comparable to the range of values (~1-20 m^3 of magma) reported by Aiuppa et al. (2010) for the erupted material during ordinary explosions. Instead, magma volumes calculated for 1 November 2017 and 24 April 2018 major explosions are 382 and 36 m^3, respectively. We recall that the calculated SO_2 mass for the 24 April 2018 major explosion could be underestimated because ash presence in the first minutes of our UV camera measurements. This implies that the calculated magma volume (36 m^3) could be also underestimated, but considering the difference of one order of magnitude between the two calculated magma volumes, we might infer that 24 April major explosion in terms of gas is not representative as a 'real', gas-rich major explosion. In support of this, Aiuppaet

al. (2010) report that ordinary activity is interspersed twice per year by larger explosions erupting ~100 m^3 of magma. This value is almost twice the volume of magma calculated for the 24 April 2018 major explosion, supporting the idea that our SO_2 mass measurements could be underestimated. Instead, the volume of magma calculated for the explosion of 1 November 2017 is much higher than the ~100 m^3 of magma erupted during major explosions proposed by Aiuppa et al. (2010), and appears to us more reasonable.

Our detailed study of SO_2 masses of 3655 ordinary explosions allows to define the ordinary activity in terms of gas associated with explosions. Our results of the SO_2 budget emitted during Strombolian activity are the scientific base for future estimations because they represents a fundamental benchmark in order to evaluate the volume of magma necessary to fuel ordinary explosions and, therefore, on the magmatic dynamics of the plumbing system of Stromboli. These types of evaluations are exclusively based on petrological data, to date. Future investigations, hence, might give the way to better define the gas budget of Stromboli and make inference on magma volumes feeding ordinary explosive degassing. These assessments will provide information on magmatic recharge. Furthermore, the comparing with the estimates of magma volumes from the erupted products will allow to better evaluate the 'deficit' of erupted magma compared to what feeds the active degassing of Strombolian activity.

Monitoring SO_2 explosive masses on active volcanoes may be an alternative way to have important information about major explosions' time occurrence. Improving our understanding about the relationship existing or not between Strombolian and major explosions and their relative SO_2 explosive masses emitted is a crucial point for monitoring high energetic and, hence, hazardous explosions in Stromboli. In order to investigate the possible existence of a relation between ordinary and major explosions at Stromboli, we adopt a statistical approach by using SO_2 mass, as a parameter describing their magnitude, in function of the frequency of occurrence of the explosions.

In nature, the probability distribution of many physical phenomena (e.g., the magnitude of earthquakes) approximately follows a power-law over a range of variable magnitudes, which is also known as Zipf's law or the Pareto distribution (Newman, 2006). The power law distribution is related to fractal properties and implies self-similarity in the system (Turcotte, 1986). The peculiarity of a power-law distribution is the scale-free distribution, which implies that in a peculiar phenomenon there is not a characteristic scale. Therefore, the power-law distribution is a special kind of probability distribution, which can be simplified as:

$$p(x) = C\, x^{-b} \qquad (\text{for } x \geq x_{min}),$$

where b is the exponent of the power-law distribution and C is a normalization constant that varies slowly and because of this can be considered constant. The constant C can be derived as follows:

$C = (b\text{-}1)\ x_{min}^{b-1}$ (this expression makes sense for b>1)

Therefore, the correct normalized expression for the power law itself results:

$$p(x) = \frac{b-1}{x_{min}}\left(\frac{x}{x_{min}}\right)^{-b}$$

A recent work of Nishimura et al. (2016), focusing on magnitude-frequency of volcanic explosion earthquakes, analyzes data of standard activity of Stromboli volcano, as no major explosion or paroxysmal activity occurred, and revealed that those data follow a power law distribution. In the case of the explosive activity at Stromboli and the occurrence of major explosions that we are investigating, we first evaluate if our data of daily explosions frequency in relation to their mass follows a power-law probability distribution. Figure 6.6 allows to immediately figuring out that for low ranges of mass recur the high explosions frequency, while we observe the opposite behavior at increasing mass ranges. For better evaluating the data distribution and quantifying the exponent of the power low distribution (b), we normalize the number of explosions considering the total number of explosions recorded in our observation period (3655).

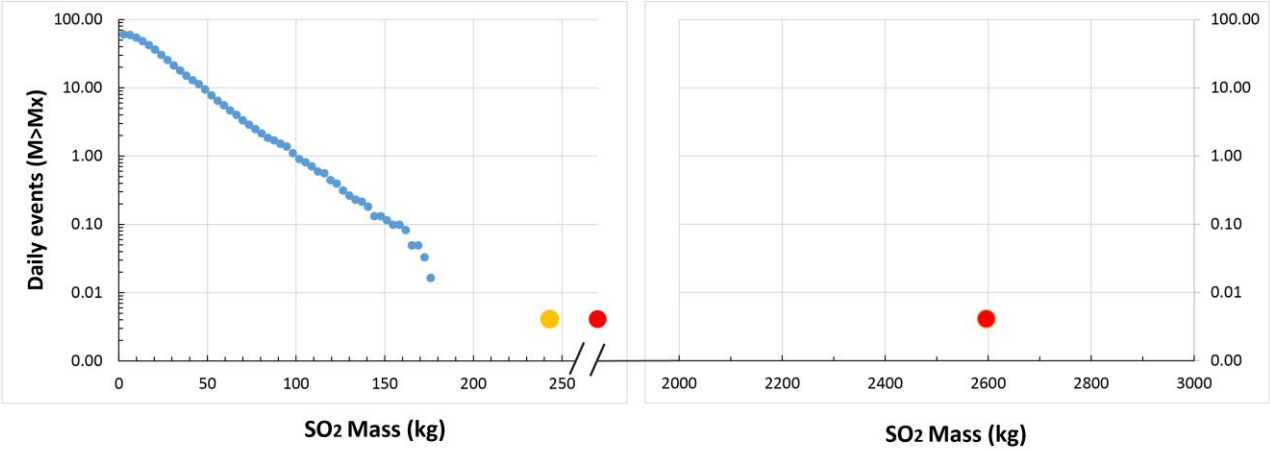

Figure 6.9 *Semi-log plot show Daily events (M>Mx) vs explosive SO_2 mass. Ordinary explosions (in blue squares) follow a power law distribution that does not fit the two major explosions (orange circle, 24 April 2018; red circle, 1 November 2017. On the left 1 November 2017 major explosion value is fictitiously plotted).*

Figure 6.9 shows again the data distribution following a power law and allows to evaluating the daily occurrence time of explosions in function of the selected mass ranges. We notice that the highest mass range (178 kg) measured in our period of observation approximates a daily number of explosions of 1.6×10^{-2}, which implies the occurrence of an explosion every 93 days. Assuming that

this statistic analysis can always be valid, we now consider the two major explosions. We recall that 1 November 2017 and 24 April 2018 major explosions yielded a mass of ~2.6 x 10^3 kg and ~0.24 x 10^3 kg, respectively, and that the latter is probably underestimated and must be considered as a minimum value. Considering that during our period of observation (243 days) we measured two major explosions, we calculate a daily occurrence value of 4.12 x 10^{-3} (red and orange circles on Figure 6.9). This value implies the occurrence of an explosion every 688 days. Following the trend associated to the power-law distribution fitting ordinary explosions, for a daily occurrence value of 1 x 10^0 we should have expected an SO_2 explosive mass of ~98 kg. These results suggests that ordinary and major explosions at Stromboli are not driven by the same magma degassing dynamics inside Stromboli conduit(s).

In conclusion, considering the system as scale-invariant, hence we might infer that major explosions are something other than the Strombolian explosions. Future statistical study that includes a greater number of major explosions with a wide range of SO_2 explosive masses is required. Our outlines concerning the relation of ordinary and major SO_2 mass explosions highlight an inverse link between magnitude of explosions and time occurrence with not trivial fallouts for explosive dynamics investigations of other open vent volcanoes.

4.5 Conclusions

We study two major explosions occurred on 1st November 2017 and 24th April 2018 and analyze in detail the SO_2 flux of the explosive sequence from the beginning to final long degassing coda and correlate it with thermal signal and volcanic tremor. Our results point to a dominant active (over-pressurized) degassing mode, as totally representative of explosive SO_2 gas output for a major explosion. Here, for the first time, SO_2 budget of a major explosion is estimated.

The interdisciplinary analysis of SO_2 degassing and volcanic tremor highlights evidences of a very long active degassing coda correlated with volcanic tremor amplitude, suggesting gas emission under over-pressurized conditions. We infer that degassing dynamic is strictly related to the source of tremor. Our inferences bring new achievements for understanding the seismic source process itself and the volcanic degassing system of Stromboli, and even extrapolate some implications that may also apply to other open-conduit basaltic volcanoes.

Here, for the first time, a magma volume necessary to provide the gaseous content to drive a major explosion is estimated. Our magma volumes of ordinary explosions are comparable to the range of

values reported for the erupted material during ordinary explosions. The volume of magma calculated for 1 November 2017 major explosion is orders of magnitude lower than the volume of magma erupted during paroxysmal explosions.- This marks the strong difference existing between the three types of explosions occurring at Stromboli (Strombolian, major and paroxysmal).

Furthermore, for a challenging comprehension about the relation between ordinary and major explosions, we make a statistics of these using SO_2 mass as a parameter describing their magnitude inferring presumable time occurrence for major explosions in Stromboli. Our calculated SO_2 mass for major explosion implies the occurrence of an explosion every ~688 days. The power-law distribution of Strombolian ordinary explosions clearly does not fit one out of the two recorded major explosions, which fall outside at sensibly higher values of mass. This means that ordinary and major explosions at Stromboli are not driven by the same magma degassing dynamics inside Stromboli conduit(s). All these conjunct studies might allow to understanding a challenging relation of low and high-energy explosive events in Stromboli with an important impact in terms of volcanic monitoring.

Concluding Remarks

Aristotele was the first to describe Stromboli's activity, which has persisted for perhaps as much as 5000 years (Allard et al., 1994). Convection of ascending gas-rich fresh magma into denser, more degassed magma in the conduit activates the "degassing machine" that relentlessly operates to sustain Strombolian activity (Allard et al., 1994, 2008; Harris and Stevenson, 1997; Chouet et al. 1974). This mechanism explains the longevity of Strombolian activity (Rosi et al., 2013). Ironically however, "explosive" gas release, albeit the focus of most studies, represents only a minor fraction of the total gas output at Stromboli. In fact, explosive activity is accompanied by continuous passive degassing (Allard et al., 1994, 2008; Burton et al., 2003, 2009) and puffing (Ripepe et al., 2002; Harris and Ripepe, 2007; Tamburello et al., 2012; Gaudin et al., 2017a, 2017b), which combine for the largest fraction of Stromboli's 'bulk degassing' (Tamburello et al., 2012). Regular Strombolian activity is periodically (1985, 2002–2003, 2007 and 2014) interrupted by lava effusions. Therefore, Stromboli exhibits a wide range of degassing regimes from passive degassing to explosive dynamics, which makes this volcano the ideal laboratory for volcanic monitoring measurements. The idea that degassing drives eruptive activity at Stromboli raises the question of why different eruptive regimes exist, and which factors determine the transition between those.

No specific work had been focused so far to studying the implications of UV Camera networks for understanding Stromboli's SO_2 flux behaviour during "regular" Strombolian activity. In **Chapter 4** of this dissertation we address this issue by reporting on the longest and most continuous SO_2 flux record obtained with permanent and automated UV camera system. Furthermore, results obtained highlight large fluctuations in SO_2 flux behaviour, which now grant the opportunity of setting thresholds between different activity levels.

Discrimination of outdegassing from individual craters at Stromboli, on a time scale of years, had this far been a challenge. Nowadays, thanks to a network of two permanent UV cameras located in strategic positions on the upper flanks of Stromboli volcano, unprecedented results are obtained. Within **Chapter 5**, simultaneously resolved SO_2 emissions from the northern (NEC) and central-southwestern (SWCC) crater vents allow the distinction of individual craters contributions to the bulk degassing output. In particular, the NEC vs SWCC relative contributions to the total SO_2 flux vary

between ~63% and ~37% (June-July 2017) to 54% and 46% (August-October 2017), respectively. Moreover, by applying a 'peak-algorithm', these first SO_2 vent-resolved measurements are also converted into active (explosions+puffing) vs. passive (quiescent) degassing modes during a larger acquisition period (~8 months). Importantly, these crater-to-crater modulations in SO_2 emissivity correspond to consistent shifts in infrasound source. Clustering of degassing activity at the NEC corresponds to periods of heightened explosive activity, as demonstrated by SO_2 and seismic records. This is interpreted as due to preferentially gas/magma channeling into the structurally weaker NE portion of the crater terrace as the supply rate of buoyant, bubble-rich magma increases (up to > ~0.3 m^3/s) in the shallow plumbing system. These vent-resolved degassing results at Stromboli volcano contribute to our ability to forecast effusive eruptions with direct implication on early warning procedures.

Rapid transitions from quiescence degassing to high-energy explosive eruptions poses a significant challenge for volcanic hazard evaluation and mitigation. 'Regular' activity at Stromboli is interrupted by so-called 'major explosions' 1-4 times per year (Aiuppa et al., 2011; Bertagnini et al., 1993; Di Traglia et al., 2013). Detailed petrological investigations have led to the conclusion that Stromboli's paroxysmal explosions, the largest explosive events, are produced by the rapid ascent and decompression of batches of gas-rich, low porphyric (LP) basaltic magma. This is erupted at the surface as highly vesiculated "blond" pumice, rising from a 7–10 km (below summit vents) deep magma storage zone. In contrast, the source mechanism of the "major" explosions is not yet understood, even though these are far more frequent and, therefore, potentially even more hazardous than paroxysmal events.

During 2017-2018, eight major explosions have occurred. Here, we use the high spatial resolution of UV cameras, to resolve the SO_2 emissions from Stromboli craters of two major explosions that occurred on 1 November 2017 and 24 April 2018 (**Chapter 6**). We analyze the SO_2 explosive sequences from the beginning to final long degassing coda, and corroborate by thermal and volcanic tremor records. Results point to: (i) a dominant active (over-pressurized) degassing mode, as largely representative of the explosive SO_2 gas output of a major explosion; (ii) an enhanced degassing process associated with major explosions continuing well after the end of the main blast (that produce the solid ejecta which consequently irradiates the thermal signal); and (iii) correlation between SO_2 degassing and volcanic tremor amplitude suggests gas emissions under over-pressure conditions. Our interdisciplinary analysis drives forward our understanding of SO_2 degassing and volcanic tremor that has the potential to constrain the degassing mechanisms with high level of detail.

This study brings new significant insights on: (a) understanding the sources of seismic tremor and (b) the dynamics of volcanic gas degassing at Stromboli. Our results also carry implications for other open-conduit basaltic volcanoes, showing that the interdisciplinary correlation between geochemical and geophysical data is key to a better understanding of eruption dynamics.

The magma volume necessary to supply the gas release during ordinary/major explosions is also estimated. Our estimated magma volumes for ordinary explosions are comparable to those previously reported. The degassing magma volume calculated for the major explosion of 1 November 2017 is much higher than the ~100 m^3 of magma erupted during major explosions (Aiuppa et al.,2010).

Furthermore, the relation between ordinary and major explosions is explored with a simple statistic treatment of SO_2 mass and recurrence time. The calculated SO_2 masses for a major explosion imply a recurrence time of an explosion every ~688 days. The power-law distribution of Strombolian ordinary explosions clearly does not fit the two major explosions, which fall outside at sensibly higher values of mass. This suggests that ordinary and major explosions at Stromboli are not driven by the same magma degassing dynamics inside Stromboli conduit(s). Although future statistical studies, including a greater number of major explosions with a wide range of SO_2 explosive masses are required, this study outlines the relationship between ordinary and major SO_2 mass explosions and highlights an inverse link between magnitude of explosions and time occurrence.

References

Acocella, V., M. Neri, and P. Scarlato (2006), Understanding shallow magma emplacement at volcanoes: Orthogonal feeder dikes during the 2002–2003 Stromboli (Italy) eruption, *Geophys. Res. Lett., 33*, L17310, doi:10.1029/2006GL026862.

Agnew, D.C. (2007), Treatise on Geophysics and Geodesy, Elsevier: New York.

Aiuppa, A., and C. Federico (2004), Anomalous magmatic degassing prior to the 5th April 2003 paroxysm on Stromboli, *Geophys. Res. Lett., 31*, L14607, doi:10.1029/2004GL020458.

Aiuppa A., Moretti R., Federico C., Giudice G., Gurrieri S., Liuzzo M., Papale P., Shinohara H., Valenza M. (2007), Forecasting Etna eruptions by real-time observation of volcanic gas composition, *Geology 35*, 1115 - 1118.

Aiuppa, A., Federico, C., Giudice, G., Giuffrida, G., Guida, R., Gurrieri, S., Liuzzo, M., Moretti, R., Papale, P (2009), The 2007 eruption of Stromboli volcano: Insights from real-time measurement of the volcanic gas plume CO_2/SO_2 ratio, *J. Volcanol. Geotherm. Res*, 182, 221–230.

Aiuppa, A., A. Bertagnini, N. Métrich, R. Moretti, A. Di Muro, M. Liuzzo, and G. Tamburello (2010), A model of degassing for Stromboli volcano, *Earth Planet. Sci. Lett., 295*, 195–204.

Aiuppa, A., M. Burton, P. Allard, T. Caltabiano, G. Giudice, S. Gurrieri, M. Liuzzo, and G. Salerno (2011), First observational evidence for the CO_2-driven origin of Stromboli's major explosions, *Solid Earth, 2*, 135–142, doi.org/10.5194/se-2-135-2011.

Aiuppa, A., J.M. de Moor, S. Arellano, D. Coppola, V. Francofonte, B. Galle, G. Giudice, M. Liuzzo, E. Mendoza, A. Saballos, A.et al.(2018), Tracking Formation of a Lava Lake From Ground and Space: Masaya Volcano (Nicaragua), 2014-2017. *Geochemistry, Geophys. Geosystems, 19*, 496–515.

A.Aiuppa., M. Bitetto, D. Delle Donne, R. D'Aleo, E. Lo Coco, G. Tamburello, A. Battaglia, M. Coltelli, D. Coppola, E. Pecora, and M. Ripepe (2018), Challenges in UV camera-based real-time SO_2 flux monitoring: insights from 5 years of continuous observations at Etna and Stromboli, Abstract Cities on Volcanoes 10.

Allard, P. A., J. Carbonelle, N. Métrich, H. Loyer, and P. Zettwoog (1994), Sulphur output and magma degassing budget of Stromboli volcano, *Nature, 368*, 326–330.

Allard, P., A. Aiuppa, M. Burton, T. Caltabiano, C. Federico, G. Salerno, and A. La Spina (2008), Crater gas emissions and the magma feeding system of Stromboli volcano, in The Stromboli Volcano: An Integrated Study of the 2002–2003 Eruption, *Geophys. Monogr. Ser., vol. 182*, edited by S. Calvari, et al., 65–80, AGU.

Allard P. (2010), A CO_2-rich gas trigger of explosive paroxysms at Stromboli basaltic volcano, Italy, *J. Volcanol. Geotherm. Res.189*, 363–374.

Andronico D., R.A. Corsaro, A. Cristaldi, and M. Polacci (2008), Characterizing high energy explosive eruptions at Stromboli volcano using multidisciplinary data: An example from the 9 January 2005 explosion, *J. Volcanol. Geotherm. Res., 176*, 541–550.

Andronico D., Cristaldi A., Del Carlo P., Taddeucci J. (2009), Shifting styles of basaltic explosive activity during the 2002–03 eruption of Mt. Etna, Italy, *J. Volcanol. Geotherm. Res., 180* (2–4), 110–122.

Andronico D., and M. Pistolesi (2010), The November 2009 paroxysmal explosions at Stromboli, *J. Volcanol. Geotherm. Res., Vol. 196,* Issues 1–2, 120-125, doi.org/10.1016/j.jvolgeores.2010.06.005.

Bachmann, O. and G.W. Bergantz (2006), Gas percolation in upper-crustal silicic crystal mushes as a mechanism for upward heat advection and rejuvenation of near-solidus magma bodies, *J. Volcanol. Geotherm. Res., 149*, 85–102.

Bani, P., and M. Lardy (2007), Sulphur dioxide emission rates from Yasur volcano, Vanuatu archipelago, *Geophys. Res. Lett. 34*:L20309. doi: 10.1029/2007GL030411.

Barberi F., F. Innocenzi, F. Ferrara, J. Keller, and L. Villari (1974), Evolution of Eolian Arc volcanism (southern Tyrrhenian sea) (1974), *Earth Planet. Sci. Lett., 21*, 269-276.

Barberi F., Rosi M., Sodi A. (1993), Volcanic hazard assessment at Stromboli based on review of historical data: *Acta Vulcanol. 3*, 173–187.

Barberi, F., L. Civetta, M. Rosi, and R. Scandone (2009), Chronology of the 2007 eruption of Stromboli and the activity of the Scientific Synthesis Group, *J. Volcanol. Geotherm. Res. 182* (3–4), 123–130.

Barnie T., M. Bombrun, M.R. Burton, A. Harris, and G. Sawyer (2015), Quantification of gas and solid emissions during Strombolian explosions using simultaneous sulphur dioxide and infrared camera observations, *J. Volcanol. Geotherm. Res. 300*, 167–174.

Beckett F.M., M. Burton, H.M. Mader, J.C. Phillips, M. Polacci, A.C. Rust, F. Witham (2014), Conduit convection driving persistent degassing at basaltic volcanoes, *J. Volcanol. Geotherm. Res., 283*, 19–35, http://dx.doi.org/10.1016/j.jvolgeores.2014.06.006.

Bertagnini A., M. Coltelli, M. Pompilio, and M. Rosi (1999), Violent Explosions Yield New Insights into Dynamics of Stromboli Volcano, *Eos, 80*, 52.

Bertagnini, A., N. Metrich, P. Landi, and M. Rosi (2003), Stromboli volcano (Aeolian Archipelago, Italy): An open window on the deepfeeding system of a steady state basaltic volcano, *J. Geophys. Res., 108*(B7), 2336, doi:10.1029/2002JB002146.

Bertagnini A., N. Métrich, L. Francalanci, P. Landi, S. Tommasini, S. Conticelli (2008), Volcanology and magma geochemistry of the present-day activity: constraints on the feeding system. In: Learning from Stromboli. Calvari S., Inguaggiato S., Puglisi G., Ripepe M., Rosi M. (eds) Am Geophys Union, *Geophys. Mon. 182*, 19–38.

Blackburn, E. A., L. Wilson, and R. J. Sparks (1976), Mechanisms and dynamics of strombolian activity, *J. Geol. Soc., 132*(4), 429–440.

Bluth, G. S. J., J. M. Shannon, I. M. Watson, A. J. Prata, and V. J. Realmuto (2007), Development of an ultra-violet digital camera for volcanic SO_2 imaging, *J. Volcanol. Geotherm. Res., 161*, 47–56.

Bonaccorso, A., S. Gambino, F. Guglielmino, M. Mattia, G. Puglisi, E. Boschi (2008), Stromboli 2007 eruption: Deflation modeling to infer shallow-intermediate plumbing system, *Geophys. Res. Lett., 35.*

Bonaccorso, A., S. Calvari, G. Garfì, L. Lodato, and D. Patanè (2003), Dynamics of the December 2002 flank failure and tsunami at Stromboli volcano inferred by volcanological and geophysical observations, *Geophys. Res. Lett., 30*(18), 1941, doi:10.1029/2003GL017702.

Bonaccorso, A., Gambino, S., Guglielmino, F., Mattia, M., Puglisi, G., and Boschi, E. (2008), Stromboli 2007 eruption: Deflation modeling to infer shallow-intermediate plumbing system, *Geophys. Res. Lett., 35*, L06311. doi:10.1029/2007GL032921.

Bonaccorso A., S. Calvari, A. Linde, S. Sacks, and E. Boschi (2012), Dynamics of the shallow plumbing system investigated from borehole strainmeters and cameras during the 15 March, 2007 Vulcanian paroxysm at Stromboli volcano, *Earth Planet. Sci. Lett., 357–358*, 249–256.

Bouche, E., Vergniolle, S., Staudacher, T., Nercessian, A., Delmont, J-C., Frogneux, M., Cartault, F., Le Pichon, A. (2010), The role of large bubbles detected from acoustic measurements on the dynamics of Erta ‘Ale lava lake (Ethiopia), *Earth Planet. Sci. Lett., 295* (1-2), 37-48, doi:10.1016/j.epsl.2010.03.020.

Burton, M., P. Allard, F. Murè, and C. Oppenheimer (2003), FTIR remotesensing of fractional magma degassing at Mount Etna, Sicily, in Volcanic Degassing, Vol. 213, eds C. Oppenheimer, D. M. Pyle, and J. Barclay (London: Geological Society Special Publication), 281–293. doi: 10.1144/GSL.SP.2003.213.01.17.

Burton, M., Caltabiano, T., Salerno, G., Mure, F., Condarelli, D. (2004), Automatic measurements of SO_2 flux on Stromboli using a network of scanning ultraviolet spectrometers, *Geophys. Res. Abstr. 6*, 03970.

Burton, M., P. Allard, F. Murè, and A. La Spina (2007a), Magmatic gas composition reveals the source depth of slug-driven Strombolian explosive activity, *Science, 317*, 227–230.

Burton M.R., Mader H.M., Polacci M. (2007b), The role of gas percolation in quiescent degassing of persistently active basaltic volcanoes, *Earth Planet. Sci. Let. 264*, 46-60.

Burton, M. R., T. Caltabiano, F. Murè, G. Salerno, and D. Randazzo (2009), SO_2 flux from Stromboli during the 2007 eruption: Results from the FLAME network and traverse measurements, *J. Volcanol. Geotherm. Res., 182*(3), 214–220.

Burton, M. R., F. Prata, and U. Platt (2015a), Volcanological applications of SO_2 cameras, *J. Volcanol. Geotherm. Res., 300*, 2–6.

Burton, M. R., Salerno, G. G., D'Auria, L., Caltabiano, T., Mure, F. & Maugeri, R. (2015), SO_2 flux monitoring at Stromboli with the new permanent INGV SO_2 camera system: A comparison with the FLAME network and seismological data, *J. Volcanol. Geotherm. Res.. 300*, 95-102.

Burton, M., G. Salerno, T. Caltabiano, D. Condarelli, V. Longo, Murà F. (2003), Volcanic SO_2 Emissions during the 2002/2003 Eruption of Stromboli, AGU, abstract id. V12H-04.

Caltabiano, T., and R. Romano (1988b), Messa a punto di metodologie di misura con apparecchiatura COSPEC del flusso di SO_2 da vulcani attivi italiani, Boll. GNV, 4, 133-145.

Calvari S., L. Spampinato, L. Lodato, A.J.L. Harris, M.R. Patrick, J. Dehn , M.R. Burton, and D. Andronico (2005), Chronology and complex volcanic processes during the 2002–2003 flank eruption at Stromboli Volcano (Italy) reconstructed from direct observations and surveys with a hand-held thermal camera, *J. Geophys Res., 110*, B02201, doi:10.1029/2004JB003129.

Calvari, S., L. Spampinato, and L. Lodato (2006), The 5 April 2003 vulcanian paroxysmal explosion at Stromboli volcano (Italy) from field observations and thermal data, *J. Volcanol. Geotherm. Res., 149*, 160–175.

Calvari S., S Inguaggiato, G. Puglisi, M. Ripepe, and M. Rosi (2008), The Stromboli Volcano: An integrated study of the 2002-2003 eruption---Introduction, in The Stromboli Volcano: An Integrated Study of the 2002–2003 Eruption, *Geophys. Monogr. Ser., vol. 182*, edited by S. Calvari, et al., pp. 1–3, AGU.

Calvari S., L. Lodato, A. Steffke, A. Cristaldi , A.J.L Harris, L. Spampinato, and E. Boschi (2010), The 2007 Stromboli flank eruption: event chronology and effusion rates using thermal infrared data, *J. Geophys Res., 115*(B04201), doi: 10.1029/2009JB006478.

Calvari S., L. Spampinato, A. Bonaccorso, C. Oppenheimer, E. Rivalta, and E. Boschi (2011) Lava effusion—a slow fuse for paroxysms at Stromboli Volcano?, *Earth Planet Sci Lett., 301*(1–2):317–323. doi:10.1016/j.epsl.2010.11.015.

Campion, R., Delgado-Granados, H., Mori, T. (2015), Image-based correction of the light dilution effect for SO_2 camera measurements, *J. Volcanol. Geotherm. Res., 300,* 48-57, doi:10.1016/j.volgeores.2015.01.004.

Capponi, A., M. R. James, and S. J. Lane (2016b), Gas slug ascent in a stratified magma: Implications of flow organisation and instability for Strombolian eruption dynamics, *Earth Planet. Sci. Lett., 435*, 159–70, doi:10.1016/j.epsl.2015.12.028.

Carniel R. and Iacop F. (2006), On the persistency of crater assignment criteria for Stromboli explosion-quakes, *Annali di Geofisica*, Vol. XXXIX, 2.

Casadevall T., Rose W., Gerlach T., Greenland L.P., Ewert J., Wunderman R., Symonds R. (1983), Gas emissions and the eruptions of Mount St. Helens through 1982, *Science, 221*, 1383-1385.

Chiocci F..L, C. Romagnoli, P. Tommasi, and A. Bosman (2008), The Stromboli 2002 tsunamigenic submarine slide: characteristics and possible failure mechanisms, *J. Geophys. Res. Solid Earth, 113*(10):B10102, doi:10.1029/2007JB005172.

Chouet B.A., Hamisevicz N., McGetchin T.R. (1974), Photoballistics of volcanic jet activity at Stromboli, Italy, *J. Geophys. Res. 79* (32), 4961–4976.

Chouet B.A., Saccorotti G., Dawson P., Martini M., Scarpa R., De Luca G., Milana G., Cattaneo M. (1999), Broadband measurements of the sources of explosions at Stromboli volcano, Italy., *Geophys. Res. Lett. 28,* 1937–1940.

Chouet, B., P. Dawson, T. Ohminato, M. Martini, G. Saccorotti, F. Giudicepietro, G. De Luca, G. Milana, and R. Scarpa (2003), Source mechanisms of explosions at Stromboli volcano, Italy, determined from moment-tensor inversions of very-long-period data, *J. Geophys. Res., 108*(B1), 2019, doi:10.1029/2002JB001919.

Christopher, T., Edmonds, M., Humphreys, M.C.S., Herd, R.A. (2010), Volcanic gas emissions from Soufrière Hills Volcano, Montserrat 1995-2009, with implications for mafic magma supply and degassing, *Geophys. Res. Lett., 37*, L00E04, doi:10.1029/2009GL041325.

Christopher, T.E., Blundy, J., Cashman, K., Cole, P., Edmonds, M., Smith, P.J., Sparks, R.S.J., Stinton, A. (2015), Crustal-scale degassing due to magma system destabilization and magma-gas decoupling at Soufrière Hills Volcano, Montserrat. *Geochem., Geophys. Geos., 16*, 2797–2811.

Cleveland R.B, Cleveland W.S., McRae J. E. and Terpenning I. (1990), STL: A Seasonal-Trend Decomposition Procedure Based on Loess, *Journal of Official Statistics, 6*, 3-73.

Colò, L., M. Ripepe, D. R. Baker, and M. Polacci (2010), Magma vesiculation and infrasonic activity at Stromboli open conduit volcano, *Earth Planet. Sci. Lett., 292*(3–4), 274–280, doi:10.1016/j.epsl.2010.01.018.

Corazzato C., L. Francalanci, M. Menna, C.M. Petrone, A. Renzulli, A. Tibaldi, and L. Vezzoli (2008), What controls sheet intrusion in volcanoes? Structure and petrology of the Stromboli sheet complex, Italy, *J. Volcanol. Geotherm. Res., 173*, 26–54, doi:10.1016/j.jvolgeores.2008.01.006.

Costa, A., Melnik, O., Sparks, R.S.J. (2007), Controls of conduit geometry and wall rock elasticity on lava dome eruptions. *Earth Planet. Sci. Lett., 260*, 137–151.

D'Aleo, R., M. Bitetto, D. Delle Donne, G. Tamburello, A. Battaglia, M. Coltelli, D. Patanè, M. Prestifilippo, M. Sciotto, and A. Aiuppa (2016), Spatially resolved SO_2 flux emissions from Mt Etna, *Geophys. Res. Lett., 43*, 7511–7519, doi:10.1002/2016GL069938.

D'Aleo R., M. Bitetto, D. Delle Donne, M. Coltelli, D. Coppola, B. McCormick Kilbride, E. Pecora, M. Ripepe, L.C. Salem, G. Tamburello and A. Aiuppa (2019), Understanding the SO_2 Degassing Budget of Mt Etna's Paroxysms: First Clues From the December 2015 Sequence., *Front. Earth Sci. 6*:239.doi: 10.3389/feart.2018.00239.

D'Auria L., Giudicepietro F., Martini M. and Orazi M. (2006), The April-May 2006 volcano-tectonic events at Stromboli volcano (Southern Italy) and their relation with the magmatic system, *Earth-Prints open archives*, http://www.earth-prints.org/handle/2122/1506.

D'Oriano C., Bertagnini A. and Pompilio M (2011), Ash erupted during normal activity at Stromboli (Aeolian Islands, Italy) raises questions on how the feeding system works, *Bull. Volcanol., 73*, 471-477, https://doi.org/10.1007/s00445-010-0425-0.

Daag A., Tubianosa B., Newhall C., Tungo N., Javier D., Dolar M., Delos Reyes P., Arboleda R., Martinez M., Regalado M. (1996), Monitoring sulfur dioxide emission at Mount Pinatubo. Fire and mud: eruptions and Lahars of Mount Pinatubo Philippines, *Institute of Volcanology and Seismology, and University of Washington press*, 409–414.

Dalton M.P., Watson I.M., Nadeau P., Werner C., Morrow W., Shannon J.M. (2009), Assessment of the UV camera sulfur dioxide retrieval for point source plumes, *J Volcanol.Geotherm. Res. 188*:358–366.

Dalton, M. P., G. P. Waite, I. M. Watson, and P. A. Nadeau (2010), Multiparameter quantification of gas release during weak strombolian eruptions at Pacaya volcano, Guatemala, *Geophys. Res. Lett., 37*, L09303, doi:10.1029/2010GL042617.

De Fino, M., L. La Volpe, S. Falsaperla, G. Frazzetta, G. Neri, L. Francalanci, and A. Sbrana (1988), The Stromboli eruption of December 6, 1985–April 25, 1986: Volcanological, petrological and seismological data, *Rend. Soc. Ital. Mineral. Petrol., 43*, 1021–1038.

Del Bello, E., E.W. Llewellin, J. Taddeucci, P. Scarlato, and S.J. Lane (2012), An analytical model for gas overpressure in slug-driven explosions: insights into Strombolian volcanic eruptions, *J. Geophys. Res.*, *117*, B02206.

Del Bello E., S.J Lane., M.R James., E.W Llewellin., J. Taddeucci, P. Scarlato, and A. Capponi (2015) Viscous plugging can enhance and modulate explosivity of strombolian eruptions, *Earth Planet. Sci. Lett.*, *423*, 210–218.

Delle Donne, D., and M. Ripepe (2012), High-frame rate thermal imagery of Strombolian explosions: Implications for explosive and infrasonic source dynamics, *J. Geophys. Res.*, *117*, B09206, doi:10.1029/2011JB008987.

Delle Donne, D., M. Ripepe, G. Lacanna, G. Tamburello, M. Bitetto, and A. Aiuppa (2016), Gas mass derived by infrasound and UV cameras: Implications for mass flow rate, *J. Volcanol. Geotherm. Res.*, *325*, 169–178.

Delle Donne, D., G. Tamburello, A. Aiuppa, M. Bitetto, G. Lacanna, R. D'Aleo, and M. Ripepe (2017), Exploring the explosive-effusive transition using permanent ultraviolet cameras, *J. Geophys. Res. Solid Earth*, *122*, 4377–4394.

Delle Donne D., A. Aiuppa, M. Bitetto, R. D'Aleo , M. Coltelli, D. Coppola, E. Pecora, M. Ripepe, and G. Tamburello (2019), Changes in SO_2 Flux Regime at Mt. Etna Captured by Automatically Processed Ultraviolet Camera Data, *Remote Sens.***,** *11*, 1201, doi:10.3390/rs11101201.

Dinger, F., Bobrowski, N., Warnach, S., Bredemeyer, S., Hidalgo, S., Arellano, S., Galle, B., Platt, U., Wagner, T. (2018), Periodicity in the BrO/SO_2 molar ratios in the volcanic gas plume of Cotopaxi and its correlation with the Earth tides during the eruption in 2015, *Solid Earth*, *9*, 247–266.

Di Traglia F., T. Nolesini, E. Intrieri, F. Mugnai, D. Leva, M. Rosi, and N. Casagli (2014), Review of ten years of volcano deformations recorded by the ground-based InSAR monitoring system at Stromboli Volcano: a tool to mitigate volcano flank dynamics and intense volcanic activity, *Earth-Sci. Rev.*, *139*, 317–335, doi:10.1007/s00445-013-0786-2.

Di Traglia, F., Calvari, S., D'Auria, L., Nolesini, T., Bonaccorso, A., Fornaciai, A., Esposito, A., Cristaldi, A., Favalli, M., and Casagli, N. (2018), The 2014 Effusive Eruption at Stromboli: New Insights from In Situ and Remote-Sensing Measurements, *Remote Sens.*, *10*, 2035.

Falsaperla S., Langer H. and Spampinato S. (1998), Statistical analysis and characteristics of volcanic tremor on Stromboli Volcano (Italy), *Bull. Volcanol.*, *60*,75–88

Falsaperla S., Lanzafame G., Longo V. and Spampinato S. (1999), Regional stress field in the area of Stromboli Italy : insights into structural data and crustal tectonic earthquakes, *J. Volcanol. Geotherm. Res. 88*, 147–166.

Fee D., and R.S. Matoza (2013), An overview of volcano infrasound: From hawaiian to plinian, local to global, *J. Volcanol. Geotherm. Res.*, *249*, 123-139, ISSN 0377-0273, https://doi.org/10.1016/j.jvolgeores.2012.09.002.

Flower, V.J.B., Carn, S.A. (2015), Characterising volcanic cycles at Soufriere Hills Volcano, Montserrat: Time series analysis of multi-parameter satellite data, *J. Volcanol. Geotherm. Res.*, *304*, 82–93.

Francalanci L., Davies G. R., Lustenhouwer W., Tommasini S., Mason P.R.D., Conticelli, S. (2005), Intra-grain Sr isotope evidence for crystal recycling and multiple magma reservoirs in the recent activity of Stromboli volcano, southern Italy, *J. Petrol., 46*, 1997-2021.

Francalanci L., F. Lucchi, J. Keller, G. De Astis, and C. A. Tranne (2013), Geological Society, London, *Memoirs, v.37*, p397-471, doi: 10.1144/M37.13, In Lucchi, F., Peccerillo, A., Keller, J., Tranne, C. A. & Rossi, P. L. (eds) 2013. The Aeolian Islands Volcanoes, *Geol. Soc. London Mem.*, 37.

Francis P., Oppenheimer C., Stevenson D. (1993), Endogenous growth of persistently active volcanoes, *Nature 366*, 554–557.

Galle B., Oppenheimer C., Geyer A., McGonigle A.J.S., Edmonds M., Horrocks L. (2003), A miniaturized ultraviolet spectrometer for remote sensing of SO_2 fluxes: a new tool for volcanic surveillance, *J. Volcanol. Geotherm. Res., 119*, 241-254.

Galle, B., Johansson, M., Rivera, C., Zhang, Y., Kihlman, M., Kern, C., Lehmann, T., Platt, U., Arellano, S., Hidalgo, S. (2010), Network for Observation of Volcanic and Atmospheric Change (NOVAC)—A global network for volcanic gas monitoring: Network layout and instrument description, *J. Geophys. Res. 2010, 115*, D05304.

Gaudin D., Taddeucci J., Scarlato P., Moroni M., Freda C., Gaeta M., Palladino D.M. (2014) Pyroclast tracking velocimetry illuminates bomb ejection and explosion dynamics at Stromboli (Italy) and Yasur (Vanuatu) volcanoes, *J. Geophys. Res. Solid Earth, 119*, 5384–5397.

Gaudin, D., J. Taddeucci, P. Scarlato, A. J. L. Harris, M. Bombrun, E. Del Bello, and T. Ricci (2017a), Characteristics of puffing activity revealed by ground-based, thermal infrared imaging: The example of Stromboli volcano (Italy), *Bull. Volcanol., 79*, 24, doi:10.1007/s00445-017-1108-x.

Gaudin, D., J. Taddeucci, P. Scarlato, E. del Bello, T. Ricci, T. Orr, B. Houghton, A. Harris, S. Rao, and A. Bucci (2017b), Integrating puffing and explosions in a general scheme for Strombolian-style activity, *J. Geophys. Res. Solid Earth, 122(3)*, 1860–1875, doi:10.1002/2016JB013707.

Giberti G., C. Jaupart, and G. Sartorius (1992), Steady state operation of Stromboli volcano, Italy: constraints on the feeding system, *Bull. Volcanol., 54*, 535-541.

Girona, T., Costa, F., Taisne, B., Aggangan, B., Ildefonso, S. (2015), Fractal degassing from Erebus and Mayon volcanoes revealed by a new method to monitor H_2O emission cycles, *J. Geophys. Res. Solid Earth 120 (5)*, 2,988-3,002, doi:10.1002/2014JB011797.

Giudicepietro, F., S. Calvari, S. Alparone, F. Bianco, A. Bonaccorso, V. Bruno, T. Caputo, A. Cristaldi, et al. (2019), Integration of Ground-Based Remote-Sensing and In Situ Multidisciplinary Monitoring Data to Analyze the Eruptive Activity of Stromboli Volcano in 2017–2018, *Remote Sens., 11*, 1813.

Harris, A.J L., and D.S. Stevenson (1997), Thermal observations of degassing open conduits and fumaroles at Stromboli and Vulcano using remotely sensed data, *J. Volcanol. Geothem. Res., 76*, 175–198.

Harris, A., and M. Ripepe (2007b), Synergy of multiple geophysical approaches to unravel explosive eruption conduit and source dynamics—A case study from Stromboli, *Chem. Erde - Geochem., 67*(1), 1–35, doi:10.1016/j.chemer.2007.01.003.

Harris, A., and M. Ripepe (2007a), Temperature and dynamics of degassing at Stromboli, *J. Geophys. Res., Solid Earth 112*, B03205, doi:10.1029/2006JB004393.

Hoff R.M. (1992), Differential SO_2 column measurements of the Mt. Pinatubo volcanic plume, *Geophys. Res.Lett., 19*, 175-178.

Holland A.S.P., Watson I.M., Phillips J.C., Caricchi L., Dalton M.P. (2011), Degassing processes during lava dome growth: Insights from Santiaguito lava dome, Guatemala, *J. Volcanol. Geotherm. Res. 202*, 153–166.

Hornig-Kjarsgaard, Keller I., Koberski J., Stadlbauer U., Francalanci L., Lenhart R. (1993), Geology, stratigraphy and volcanological evolution of the island of Stromboli, Aeolian arc, Italy, *Acta Vulcanol. 3*, 21–68.

Houghton B.F., Gonnermann H.M. (2008), Basaltic explosive volcanism: Constraints from deposits and models, *Chem. Erde Geochem. 68(2),* 117–140.

Kantzas E.P., Mcgonigle A.J.S., Tamburello G., Aiuppa A., Bryant R.G. (2010), Protocols for UV camera volcanic SO_2 measurements, *J. Volcanol. Geotherm. Res. 194*, 55–60.

Kazahaya, R., T. Mori, M. Takeo, T. Ohminato, T. Urabe, and Y. Maeda (2011), Relation between single very long period pulses and volcanic gas emissions at Mt. Asama, Japan, *Geophys. Res. Lett., 38*, L11307, doi:10.1029/2011GL047555.

Kern, C., Lubcke, P., Bobrowski, N., Campion, R., Mori, T., Smekens, J.F., Stebel, K., Tamburello, G., Burton, M., Platt, U., Prata, F. (2015), Intercomparison of SO2 camera systems for imaging volcanic gas plumes, *J. Volcanol. Geotherm. Res. 300*, 22-36, doi:10.1016/j.volgeores.2014.08.026.

Kern C., Kick F., Lübcke P., Vogel L., Wöhrbach M., Platt U. (2010a), Theoretical description of functionality, applications, and limitations of SO_2 cameras for the remote sensing of volcanic plumes, *Atmos. Meas. Tech. 3*, 733–749.

Kern C., Deutschmann T., Vogel L., Wöhrbach M., Wagner T., Platt U. (2010b), Radiative transfer corrections for accurate spectroscopic measurements of volcanic gas emissions, *Bull. Volcanol., 72*, 233-247.

Kokelaar P. and Romagnoli C. (1995), Sector collapse, sedimentation, and clast population evolution at an active island-arc volcano: Stromboli (Italy), *Bull. Volcanol., 57*, 240-262.

Kondo G., Aoyama H., Nishimura T., Ripepe M., Lacanna G., Genco R., Kawaguchi R., Yamada T., Miwa T. and Fujita E. (2019), Gas flux cyclic regime at an open vent magmatic column inferred from seismic and acoustic records, *Sci. Rep.* 9, 5678.

James M.R., Lane S. J., Chouet B. (2004), Pressure changes associated with the ascent and bursting of gas slugs in liquid-filled vertical and inclined conduits, *J. Volcanol. Geotherm. Res., 129* (1–3), 61–82.

James M. R., Lane S.J., Chouet B. (2006), Gas slug ascent through changes in conduit diameter: Laboratory insights into a volcano-seismic source process in low-viscosity magmas, *J. Geophys. Res., 111,* B05201.

James M. R., Lane S.J., Corder S.B. (2008), Modelling the rapid near surface expansion of gas slugs in low viscosity magmas, in Fluid Motion in Volcanic Conduits: A Source of Seismic and Acoustic Signals, edited by S. J. Lane and J. S. Gilbert, *Geol. Soc. Spec. Publ, 307*, 147–167.

James M.R., Lane S.J., Wilson L., Corder S.B. (2009), Degassing at low magma-viscosity volcanoes: Quantifying the transition between passive bubble-burst and Strombolian eruption, *J. Volcanol. Geotherm. Res., 180* (2–4), 81–88.

Jaupart C., S. Vergniolle (1988), Laboratory models of Hawaiian and Strombolian eruptions, *Nature, 331,* 58-60.

Johansson, M., B. Galle, Y. Zhang, C. Rivera, D. Chen, and K. Wyser (2009), The dual-beam mini-DOAS technique—Measurements of volcanic gas emission, plume height and plume speed with a single instrument, *Bull. Volcanol., 71(7*), 747–751.

Johnson J. B., and M. Ripepe (2011), Volcano infrasound: A review, *J. Volcanol. Geotherm. Res., 206,* 61–69, doi:10.1016/j.jvolgeores.2011.06.006.

Ilanko, T., Oppenheimer, C., Burgisser, A., Kyle, P. (2015a), Cyclic degassing of Erebus volcano, Antarctica, *Bull. Volcanol.77*, doi:10.1007/s00445-015-0941-z.

Ilanko, T., Oppenheimer, C., Burgisser, A., Kyle, P. (2015b), Transient degassing events at the lava lake of Erebus volcano, Antarctica: Chemistry and mechanism, *Geo. Res. J., 7,* 43-58, doi:10.1016/j.grj.2015.05.001.

La Felice S. and Landi P. (2011a), A spatter-forming, large-scale paroxysm at Stromboli Volcano (Aeolian Islands, Italy): insight into magma evolution and eruption dynamics, *Bull. Volcanol., 73,* 1393-1406, https://doi.org/10.1007/s00445-011-0476-x.

La Felice S. and Landi P. (2011b), The 2009 paroxysmal explosions at Stromboli (Italy): magma mixing and eruption dynamics, *Bull. Volcanol*., *73*, 1147-1154, doi.org/10.1007/s00445-011-0502-z.

Landi P., Métrich N., Bertagnini A., Rosi M. (2008), Recycling and "re-hydratation" of degassed magma inducing transient dissolution/crystallization events at Stromboli (Italy), *J. Volcanol. Geotherm. Res. 174,* 325–336.

Landi, P., Marchetti, E., La Felice, S., Ripepe, M., and Rosi, M. (2011), Integrated petrochemical and geophysical data reveals thermal distribution of the feeding conduits at Stromboli volcano, Italy, *Geophys. Res. Lett.*, 38, L08305, doi:10.1029/2010GL046296.

Lautze N. C., Houghton B. F. (2007), Linking variable explosion style and magma textures during 2002 at Stromboli volcano, Italy, *Bull. Volcanol., 69*, 445–460.

La Rocca, M., D. Galluzzo, G. Saccorotti, G., S. Tinti, G.B. Cimini, and E. Del Pezzo (2004), Seismic signals associated with landslides and with a tsunami at Stromboli volcano, Italy, *Bull. Seismol. Soc. America, 94(5),* 1850-1867.

Leduc, L., L. Gurioli, A. Harris, L. Colò, and E. F. Rose-Koga (2015), Types and mechanisms of Strombolian explosions: Characterization of a gas dominated explosion at Stromboli, *Bull. Volcanol., 77*(1), 1–15, doi:10.1007/s00445-014-0888-5.

N. Linde, L. Baron, T. Ricci, A. Finizola, A. Revil, F. Muccini, L. Cocchi, C. Carmisciano (2014), 3D density structure and geological evolution of Stromboli volcano (Aeolian Islands, Italy) inferred

from land-based and marine gravity data, *J. Volcanol. Geotherm. Res., 273*, 58-69, doi:10.1016/j.jvolgeores.2014.01.006.

Liu, E.J., Wood, K., Mason, E., Edmonds, M., Aiuppa, A., Giudice, G., Bitetto, M., Francofonte, V., Burrow, S., Richardson, T., et al. (2019), Dynamics of Outgassing and Plume Transport Revealed by Proximal Unmanned Aerial System (UAS) Measurements at Volcán Villarrica, Chile. *Geochem., Geophys. Geosys., 20*, 730–750.

Lübcke P., Bobrowski N., Illing S., Kern C., Alvarez Nieves J.M., Vogel L., Zielcke J., Delgado, Granados H., Platt U. (2013), On the absolute calibration of SO_2 cameras, *Atmos. Meas. Tech. 6* (3), 677–696.

Lucas, B. D., and T. Kanade (1981), An iterative image registration technique with an application to stereo vision, IJCAI, 81(1), 674–679.

Malinconico, L. L. (1987), On the variation of SO_2 emission from volcanoes, *J. Volcanol. Geotherm. Res., 33*, 231-237.

Manga M. (1996), Waves of bubbles in basaltic magmas and lavas, *J. Geophys. Res.,101*(17), 457–17, 465.

Marchetti, E., M. Ripepe, G. Ulivieri, M.R. Burton, T. Caltabiano, and G. Salerno (2008), Gas Flux Rate and Migration of the Magma Column, in The Stromboli Volcano: An Integrated Study of the 2002–2003 Eruption, *Geophys. Monogr. Ser., vol. 182*, edited by S. Calvari, et al., 259-267, AGU, https://doi.org/10.1029/182GM21.

Marchetti, E., M. Ripepe, A. J. L. Harris, and D. Delle Donne (2009), Tracing the differences between Vulcanian and strombolian explosions using infrasonic and thermal radiation energy, *Earth Planet. Sci. Lett., 279*(3), 273–281, doi:10.1016/j.epsl.2009.01.004.

Marchetti E., R. Genco, and M. Ripepe (2009) Ground deformation and seismicity related to the propagation and drainage of the dyke feeding system during the 2007 effusive eruption at Stromboli Volcano (Italy), *J. Volcanol. Geotherm. Res., 182*(3–4),155–161, doi:10.1016/j.jvolgeores.2008.11.016.

Marchetti E. , M. Ripepe, P. Campus, A. Le Pichon, J.Vergoz, G. Lacanna, P. Mialle, P. Héreil and P. Husson (2019), Long range infrasound monitoring of Etna volcano, *Sci. Reports, 9*, 18015, doi.org/10.1038/s41598-019-54468-5.

Mercalli G. (1881), Natura delle eruzioni dello Stromboli ed in generale dell'attività sismico-vulcanica delle isole Eolie, *Atti. Soc. Ital. Sci. Nat., 24*, 105-135.

Métrich, N., Bertagnini, A., Landi, P., Rosi, M. (2001), Crystallization driven by decompression and water loss at Stromboli volcano (Aeolian Islands, Italy), *J. Petrol., 42*, 1471-1490, doi:10.1093/petrology/42.8.1471.

Métrich N., Bertagnini A., Landi P., Rosi M. (2005), Triggering mechanism at the origin of paroxysms at Stromboli (Aeolian Arcipelago, Italy): The 5 April 2003 eruption, *Geophys. Res. Lett., 32*, 10305.

Métrich N., Bertagnini A., Di Muro A. (2010), Conditions of magma storage, degassing and ascent at Stromboli: new insights into the volcano plumbing system with inferences on the eruptive dynamics, *J. Petrol., 51,* 603–626.

McGonigle A.J.S., Oppenheimer C., Galle B., Mather T., Pyle D. (2002), Walking traverse and scanning DOAS measurements of volcanic gas emission rates, *Geophys. Res. Lett., 29* (20),1985.

McGonigle A.J.S., Hilton D.R., Fischer T.P., Oppenheimer C. (2005), Plume velocity determination for volcanic SO_2 flux measurements, *Geophys. Res. Lett., 32*, L11302.

McGonigle A.J.S. (2007), Measurement of volcanic SO 2 fluxes with differential optical absorption spectroscopy*, J. Volcanol. Geotherm. Res. 162*, 111–122.

McGonigle A.J.S., Aiuppa A., Ripepe M., Kantzas E.P., Tamburello G. (2009), Spectroscopic capture of 1 Hz volcanic SO_2 fluxes and integration with volcano geophysical data, *Geophys. Res. Lett., 36* (L21309).

McGonigle, A.J.S., T.D. Pering, T.C. Wilkes, G. Tamburello, R. D'Aleo, M. Bitetto, A. Aiuppa, J.R. Willmott (2017), Ultraviolet Imaging of Volcanic Plumes: A New Paradigm in Volcanology, *Geosciences, 7*, 68.

McGreger A.D., Lees J.M. (2004), Vent discrimination at Stromboli Volcano, Italy, *J. Volcanol. Geotherm. Res., 137*, 169–185.

Moffat A.J., M. Millán (1971), The application of optical correlation techniques to the remote sensing of SO_2 plumes using sky light, *Atmos. Environ., 5*, 677-690.

Mori, T., and M. Burton (2006), The SO_2 camera: A simple, fast and cheap method for ground-based imaging of SO_2 in volcanic plumes, *Geophys. Res. Lett., 33*, L24804, doi:10.1029/2006GL027916.

Mori, T., and M. Burton (2009), Quantification of the gas mass emitted during single explosions on Stromboli with the SO_2 imaging camera, *J. Volcanol. Geotherm. Res*, *188*, Issue 4, 395-400, https://doi.org/10.1016/j.jvolgeores.2009.10.005.

Moussallam, Y., Tamburello, G., Peters, N., Apaza, F., Schipper, C.I., Curtis, A., Aiuppa, A., Masias, P., et al. (2017), Volcanic gas emissions and degassing dynamics at Ubinas and Sabancaya volcanoes, implications for the volatile budget of the central volcanic zone, *J. Volcanol. Geotherm. Res., 343*, 181–191.

Nadeau P., Palma J.L., Waite G.P. (2011), Linking volcanic tremor, degassing and eruption dynamics via SO_2 imaging, *Geophys. Res. Lett., 38*, 1–5.

Nadeau, P. A., C. A. Werner, G. P. Waite, S. A. Carn, I. D. Brewer, T. Elias, A. J. Sutton, and C. Kern (2015), Using SO_2 camera imagery and seismicity to examine degassing and gas accumulation at Kilauea volcano, May 2010, *J. Volcanol. Geotherm. Res., 300*, 70–80.

Namiki A., M. Manga (2008), Transition between fragmentation and permeable outgassing of low viscosity magmas, *J. Volcanol. Geotherm. Res. 169* (1–2), 48–60.

Neri, M., and G. Lanzafame (2009), Structural features of the 2007 Stromboli eruption, *J. Volcanol. Geotherm. Res., 182*, 137–144.

Newcomb, G.S., Millán, M.M., 1970. Theory, applications and results of the long-line correlation spectrometer. IEEE Transactions *Geoscience Electronics GE-8,* 149-157, doi:10.1109/TGE.1970.271410.

Newman M.E.J (2006), Power laws, Pareto distributions and Zipf's law, *Contemporary Physics.*

Nicholson, E.J., Mather, T.A., Pyle, D.M., Odbert, H.M., Christopher, T. (2013), Cyclical patterns in volcanic degassing revealed by SO_2 flux timeseries analysis: An application to Soufrière Hills Volcano, Montserrat, *Earth Planet. Sci. Lett., 375*, 209–221.

Nishimura T., Iguchi M., Hendrasto M , Aoyama H., Yamada T. , Ripepe M. and Genco R. (2016), Magnitude–frequency distribution of volcanic explosion earthquakes, *Earth, Planets and Space, 68*, 125 DOI 10.1186/s40623-016-0505-2.

Olmos R., Barrancos J., Ivera C.R., Barahona F., López D.L., Henriquez B., Hernández A., Benitez E., Hernández P.A., Pérez N.M., Galle B.O. (2007b), Anomalous emissions of SO_2 during the recent eruption of Santa Ana volcano, El Salvador, Central America, *Pure and Appl.Geoph. 164 (12*), 2489-2506.

Oppenheimer C., Francis P., Burton M.R., Maciejewski A., Boardman L. (1998a), Remote measurement of volcanic gases by Fourier transform infrared spectroscopy, *Appl. Phys. B., 67*, 505–515.

Oppenheimer C., D.M., Pyle, J., Barcaly (2003), Volcanic degassing, *Geol. Soc. London, Special Publication, 213.*

Oppenheimer, C., P. Kyle, F. Eisele, J. Crawford, G. Huey, D. Tanner, S. Kim, L. Mauldin, D. Blake, and A. Beyersdorf (2010), Atmospheric chemistry of an Antarctic volcanic plume, *J. Geophys. Res., 115*, D04303, doi:10.1029/2009JD011910.

Oppenheimer, C., B. Scaillet, and R. S. Martin (2011), Sulfur degassing from volcanoes: Source conditions, surveillance, plume chemistry and Earth system impacts, *Rev. Mineral. Geochem., 73*, 363–421.

Palma, J. L., Calder, E. S., Basualto, D., Blake, S., Rothery, D. A. (2008), Correlations between SO_2 flux, seismicity, and outgassing activity at the open vent of Villarrica volcano, Chile. Journal of Geophysical Research 113 (B10201), doi:10.1029/2008JB005577.

Palma, J. L., Blake, S., Calder, E. S (2011), Constraints on the rates of degassing and convection in basaltic open-vent volcanoes. *Geoch., Geoph., Geos. 12 (11*), doi :10.1029/2011GC003715.

Parfitt E.A., Wilson L. (1995), Explosive volcanic-eruptions: the transition between Hawaiian-style lava fountaining and Strombolian explosive activity, *Geophys. J. Int. 121*(1), 226–232.

Parfitt E.A. (2004), A discussion of the mechanisms of explosive basaltic eruptions, *J. Volcanol. Geotherm. Res. 134*, 77–107.

Pasquaré G., Francalanci L., Garduno V.H., Tibaldi A. (1993), Structure and geologic evolution of the Stromboli volcano, Aeolian Islands, Italy, *Act. Vulcanol., 3*, 79-90.

Patrick, M. R., A. Harris, M. Ripepe, J. Dehn, D. A. Rothery, and S. Calvari (2007), Strombolian explosive styles and source conditions: Insights from thermal (FLIR) video, *Bull. Volcanol., 69(7*), 769–784.

Pering T.D, Tamburello G., McGonigle A.J.S., Aiuppa A., Cannata A., Giudice G., Patanè D. (2014a), High time resolution fluctuations in volcanic carbon dioxide degassing from Mount Etna, *J. Volcanol. Geotherm. Res.*, *270*, 115–121.

Pering T.D., Tamburello G., McGonigle A.J.S., Aiuppa A., James M.R., Lane S.J., Sciotto M. (2014b), Dynamics of mild strombolian activity on Mt. Etna, *J. Volcanol. Geotherm. Res.*, *300*, 103–111.

Pering, T. D., A. J. S. McGonigle, M. R. James, G. Tamburello, A. Aiuppa, D. Delle Donne, and M. Ripepe (2016), Conduit dynamics and post explosion degassing on Stromboli: A combined UV camera and numerical modeling treatment, *Geophys. Res. Lett.*, *43*, doi:10.1002/2016GL069001.

Pering, T.D., McGonigle, A.J.S., Tamburello, G., Aiuppa, A., Bitetto, M., Rubino, C., Wilkes, T.C. (2017), A Novel and Inexpensive Method for Measuring Volcanic Plume Water Fluxes at High Temporal Resolution. *Remote Sens*, *9*, 146.

Pering, T.D. and McGonigle, A.J.S. (2018), Combining Spherical-Cap and Taylor Bubble Fluid Dynamics with Plume Measurements to Characterize Basaltic Degassing, *Geosciences*, *8*, 42.

Pering, T.D., Ilanko, T., Wilkes, T.C., England, R.A., Silcock, S.R., Stanger, L.R., Willmott, J.R., Bryant, R.G., McGonigle, A.J.S. (2019), A Rapidly Convecting Lava Lake at Masaya Volcano, Nicaragua, *Front. Earth Sci.*, *6*, 241.

Peters, N., Oppenheimer, C., Killingsworth, D.R., Frechette, J., Kyle, P. (2014a), Correlation of cycles in Lava Lake motion and degassing at Erebus Volcano, Antarctica, *Geochem., Geoph., Geos. 15* (8), 3,244-3,257, doi:10.1002/2014GC005399.

Peters, N., Oppenheimer, C., Kyle, P., Kingsbury, N. (2014b), Decadal persistence of cycles in lava lake motion at Erebus volcano, Antarctica. *Earth Planet. Sci. Lett.*, *395*, 1-12, doi:10.1016/j.epsl.2014.03.032.

Peters N., Hoffmann A., Barnie T., Hergoz M., Oppenheimer C. (2014), Use of motion estimation algorithms for improved flux measurements using SO_2 cameras, *J. Volcanol. Geotherm Res.*, *8*-31.

Peters, N., Hoffmann, A., Barnie, T., Herzog, M., Oppenheimer, C. (2015), Use of motion estimation algorithms for improved flux measurements using SO_2 cameras. *J. Volcanol. Geotherm. Res*., *300*, 58-69, doi:10.1016/j.volgeores.2014.08.031.

Pichavant M., Di Carlo I., Le Gac Y., Rotolo S.G., Scaillet B. (2009), Experimental Constraints on the Deep Magma Feeding System at Stromboli Volcano, Italy, *J. Petrol. 50*-4, 601-624.

Pichavant M., Pompilio M., D'Oriano C. and Di Carlo I. (2011), Petrography, mineralogy and geochemistry of a primitive pumice from Stromboli: implications for the deep feeding system, *Eur. J. Mineral.*, *23*, 499–517.

Pichavant M., Di Carlo I., Rotolo S.G., Scaillet B., Burgiss A., Le Gall N., Martel C. (2013), Generation of CO2-rich melts during basalt magma ascent and degassing, *Contrib. Mineral. Petrol.*, *166*, 545–561.

Pino N.A., Ripepe M. and Cimini G.B. (2004), The Stromboli Volcano landslides of December 2002: A seismological description, *Geophys. Res. Lett., 31*, L02605.

Pino N.A. and Boschi E. (2009), Seismic detection of island trapped sea waves from a landslide-generated tsunami at Stromboli (Italy*), Geophys. Res. Lett., 36*, L09305.

Pioli L., M. Pistolesi, and M. Rosi (2014) Transient explosions at open-vent volcanoes: the case of Stromboli (Italy), *Geology, 42*(10):863–866, doi:10.1130/G35844.1.

Pistolesi, M., M. Rosi, L. Pioli, A. Renzulli, A. Bertagnini, and D. Andronico (2008), The paroxysmal explosion and its deposits, in The Stromboli Vol-cano: An Integrated Study of the 2002–2003 Eruption, Geophys. Monogr.Ser., vol. 182, edited by S. Calvari et al., 317–329, AGU, Washington,D. C., doi:10.1029/182GM26.

Pistolesi M., D. Delle Donne, L. Pioli, M. Rosi, and M. Ripepe (2011), The 15 March 2007 explosive crisis at Stromboli Volcano, Italy: assessing physical parameters through a multidisciplinary approach, *J. Geophys. Res., 116*, B12206, doi:10.1029/2011JB008527.

Pistolesi M., A. Bertagnini, A. Di Roberto, M. Ripepe, and M. Rosi (2020), Tsunami and tephra deposits record interactions between past eruptive activity and landslides at Stromboli volcano, Italy, *Geology*, doi.org/10.1130/G47331.1.

Platt, U., Stutz, J. (2008) Differential Optical Absorption Spectroscopy, *Phys. Earth and Space* Environments, doi:10.1007/978-3-540-75776-4.

Polacci M., Baker D.R., Bai L. and Mancini L. (2008), Large vesicles record pathways of degassing at basaltic volcanoes, *Bull. Volcanol, 70*, 1023 – 1029, doi:10.1007/s00445-007-0184-8

Ripepe, M., Rossi, M., Saccorotti, G. (1993), Image processing of explosive activity at Stromboli, *J. Volcanol. Geotherm. Res., 54*, 335–351.

Ripepe M., Braun T. (1994), Air-wave phases in strombolian explosion-quake seismograms: a possible indicator for magma level?, *Acta Vulcanol., 5*, 201–206.

Ripepe, M., Poggi, P., Braun, T., Gordeev, E. (1996), Infrasonic waves and volcanic tremor at Stromboli, *Geophys. Res. Lett., 23*, 181-184.

Ripepe, M., Gordeev, E. (1999), Gas bubble dynamics model for shallow volcanic tremor at Stromboli, *J. Geophys. Res., 104*, 10639-10654.

Ripepe, M., Ciliberto, S., Della Schiava, M. (2001), Time constraint for modelling source dynamics of volcanic explosions at Stromboli, *J. Geophys. Res., 106*, 8713-8727.

Ripepe, M., A. J. L. Harris, and R. Carniel (2002), Thermal, seismic and infrasonic evidences of variable degassing rates at Stromboli volcano, *J. Volcanol. Geotherm. Res., 118*(3–4), 285–297, doi:10.1016/S0377-0273(02)00298-6.

Ripepe, M., and E. Marchetti (2002), Array tracking of infrasonic sources at Stromboli volcano, *Geophys. Res. Lett., 29*(22), 33-1–33–4, doi:10.1029/2002GL015452.

Ripepe M., E. Marchetti, G. Ulivieri, A. Harris, J. Dehn, M.R. Burton, T. Caltabiano, G. Salerno (2005), Effusive to explosive transition during the 2003 eruption of Stromboli Volcano, *Geology, 33*(5), 341– 344. doi:10.1130/G21173.1.

Ripepe M., E. Marchetti, and G. Ulivieri (2007), Infrasonic monitoring at Stromboli Volcano during the 2003 effusive eruption: insights on the explosive and degassing process of an open conduit system, *J. Geophys. Res., 112*, B09207, doi:10.1029/2006 JB004613.

Ripepe, M., and A. J. L. Harris (2008), Dynamics of the 5 April 2003 explosive paroxysm observed at Stromboli by a near-vent thermal, seismic and infrasonic array, *Geophys. Res. Lett., 35*, L07306, doi:10.1029/2007GL032533.

Ripepe, M., D. Delle Donne, A. J. L. Harris, E. Marchetti, and G. Ulivieri (2008), Dynamics of strombolian activity, in The Stromboli Volcano: An Integrated Study of the 2002–2003 Eruption, *AGU Geophysical Monograph Series, vol. 182*, edited by S. Calvari et al., pp. 39–48., doi:10.1029/182GM05.

Ripepe, M., D. Delle Donne, G. Lacanna, E. Marchetti, and G. Ulivieri (2009), The onset of the 2007 Stromboli effusive eruption recorded by an integrated geophysical network, *J. Volcanol. Geotherm. Res., 182*, 131–136, doi:10.1016/j.jvolgeores.2009.02.011.

Ripepe, M., D. Delle Donne, R. Genco, G. Maggio, M. Pistolesi, E. Marchetti, and P. Poggi (2015), Volcano seismicity and ground deformation unveil the gravity-driven magma discharge dynamics of a volcanic eruption, *Nat. Commun., 6*.

Ripepe M, M. Pistolesi, D.Coppola , D.Delle Donne , R. Genco, G. Lacanna , M. Laiolo, E. Marchetti, G. Ulivieri, S. Valade (2017), Forecasting effusive dynamics and decompression rates by magmastatic model at open-vent volcanoes, *Sci. Rep., 7*, 3885, doi:10.1038/s41598-017-03833-3SREP-16-46587.

Ripepe, M., Marchetti, E., Delle Donne, D., Genco, R., Innocenti, L., Lacanna, G., & Valade, S. (2018), Infrasonic early warning system for explosive eruptions, *J. Geophys. Res. Solid Earth*, 123, 9570–9585, doi.org/10.1029/2018JB015561.

Rizzo, A.L., C. Federico, S. Inguaggiato, A. Sollami, M. Tantillo, F. Vita, S. Bellomo, M. Longo, F. Grassa, and M. Liuzzo (2015), The 2014 effusive eruption at Stromboli volcano (Italy): Inferences from soil CO_2 flux and $^3He/^4He$ ratio in thermal waters, *Geophys. Res. Lett., 42*, 2235–2243.

Rosi, M., A. Bertagnini, and P. Landi (2000), Onset of the persistent activity at Stromboli volcano (Italy), *Bull. Volcanol., 62*(4–5), 294–300, doi:10.1007/s004450000098.

Rosi M., A. Bertagnini, A.J.L. Harris, L. Pioli, M. Pistolesi, and M. Ripepe (2006), A case history of paroxysmal explosion at Stromboli: timing and dynamics of the April 5, 2003 event, *Earth Planet Sci. Lett., 243*:594–606.

Rosi M., M. Pistolesi, A. Bertagnini, P. Landi, M. Pompilio, and A. Di Roberto (2013), Stromboli volcano, Aeolian Islands (Italy): present eruptive activity and hazards. In: Lucchi F, PeccerilloA, Keller J, Tranne CA, Rossi PL (ed), The Aeolian Islands volcanoes, *Geol.Soc., London Mem., 37*, 473–490, doi:10.1144/M37.14.

Rymer, H., Locke, C.A., Brenes, J., Williams-Jones, G. (2005),Magma plumbing processes for persistent activity at Poás volcano, Costa Rica. *Geophys. Res. Lett., 32*, L08307.

Saballos, J.A., V. Conde, R. Malservisi, *et al.* (2014), Relatively short-term correlation among deformation, degassing, and seismicity: a case study from Concepción volcano, Nicaragua, *Bull. Volcanol., 76***,** 843 https://doi.org/10.1007/s00445-014-0843-5.

Salerno, G.G., Burton, M.R., Oppenheimer, C., Caltabiano, T., Randazzo, D., Bruno, N., Longo, V., (2009a), Three-years of SO_2 flux measurements of Mt. Etna using an automated UV scanner array: comparison with conventional traverses and uncertainties in flux retrieval, *J. Volcanol. Geotherm. Res.*, *183* (1–2), 76–83.

Salerno, G.G., Burton, M.R., Oppenheimer, C., Caltabiano, T., Tsanev, V.I., and Bruno, N. (2009b), Novel retrieval of volcanic SO_2 abundance from ultraviolet spectra, *J. Volcanol. Geotherm. Res.*, *181* (1–2), 141–153.

Salerno G.G., M. Burton, G. Di Grazia, T. Caltabiano, and C. Oppenheimer (2018), Coupling Between Magmatic Degassing and Volcanic Tremor in Basaltic Volcanism, *Front. Earth Sci.*, *6*:157.doi: 10.3389/feart.2018.00157.

Seyfried R., Freundt A. (2000), Experiments on conduit flow and eruption behavior of basaltic volcanic eruptions, *J. Geophys. Res.*, *105*(B10), 23,727–23,740.

Shinohara, H. (2008), Excess degassing from volcanoes and its role on eruptive and intrusive activity, *Rev. Geophys.*, *46*, RG4005, doi:10.1029/2007RG000244.

Smekens J.F., Burton M.R. and Clarke A.B. (2015), Validation of the SO_2 camera for high temporal and spatial resolution monitoring of SO_2 emissions, *J. Volcanol. Geotherm. Res.*, *300*, 37–47.

Spampinato L., Oppenheimer C., Cannata A., Montalto P., Salerno G., Calvari S. (2012), On the time-scale of thermal cycles associated with open-vent degassing, *Bull. Volcanol.*, *74*(6), 1281–1292.

Stevenson D.S., and S. Blake (1998), Modelling the dynamics and thermodynamics of volcanic degassing, *Bull. Volcanol.*, *60*, 307–317, doi:10.1007/s004450050234.

Stoiber R.E., Malone G.B., and Bratton G.P. (1978), *Geol. Soc. Am.*, Abstr. Progm. 10, 148.

Stoiber R.E., Lawrence L., Malinconico L., Williams S.N. (1983), Use of the correlation spectrometer at volcanoes. In: Tazieff, H., Sabroux (Eds.), Forecasting volcanic events. Elsevier, New York, 425–444.

Suckale, J, Hager, B.H., Elkins-Tanton, L.T., Nave, J-C. (2010b), It takes three to tango: 2. Bubble dynamics in basaltic volcanoes and ramifications for modelling normal Strombolian activity. *J. Geoph. Res., 115* (B07410), doi:10.1029/2009JB006917.

Sutton, A.J., Elias, T., Gerlach, T.M., and Stokes, J.B. (2001), Implications for eruptive processes as indicated bysulfur dioxide emissions from Kilauea Volcano, Hawaii, 1979—1997. *J. Volcanol. Geotherm. Res.*, *108*, 283–302.

Sweeney, D., Kyle, P.R., Oppenheimer, C. (2008), Sulfur dioxide emissions and degassing behavior of Erebus volcano, Antarctica, *J. Volcanol. Geotherm. Res.*, *177*, 725–733.

Symonds R.B., Rose W.I., Bluth G.J.S., Gerlach T.M. (1994), Volcanic gas studies: methods, results, and applications, in Volatiles in Magmas, edited by M.R. Carroll And J.R. Holloway, *Rev. Mineral. 30*, 1-60.

Symonds R.B., Gerlach T.M., Reed M.H. (2001), Magmatic gas scrubbing: implications for volcano monitoring, *J. Volcanol. Geotherm. Res.*, *108*, 303-341.

Taddeucci J., Alatorre-Ibargüengoitia M.A., Moroni M., Tornetta L., Capponi A. (2012b), Physical parameterization of Strombolian eruptions via experimentally-validated modeling of high-speed observations, *Geophys. Res. Lett., 39*, L16306, doi:10.1029/2012GL052772, 2012

Taddeucci, J.,D. M. Palladino, G. Sottili, D. Bernini, D. Andronico, andA. Cristaldi (2013), Linked frequency and intensity of persistent volcanic activity at Stromboli (Italy), *Geophys. Res. Lett., 40*, 3384–3388, doi:10.1002/grl.50652.

Tamburello G., E.P. Kantzas, A.J.S. McGonigle, and A. Aiuppa (2011a), Vulcamera: A program for measuring volcanic SO_2 using UV cameras, *Ann. Geophys., 54*, 219–221.

Tamburello, G., A. Aiuppa, E. P. Kantzas, A. J. S. McGonigle, and M. Ripepe (2012), Passive vs. active degassing modes at an open-vent volcano (Stromboli, Italy), *Earth Planet. Sci. Lett., 359–360*, 106–116.

Tamburello G., Aiuppa A., McGonigle A.J.S., Allard P., Cannata A., Giudice G., Kantzas E.P., Pering T.D. (2013), Periodic volcanic degassing behavior: The Mount Etna example. *Geophys. Res. Lett.,40*:4818–4822.

Tarchi D., N. Casagli, J. Fortuny-Guasch, L. Guerri, G. Antonello, and D. Leva (2008), Ground deformation from ground-based SAR interferometry, in *The Stromboli Volcano: An Integrated Study of the 2002–2003 Eruption, Geophys. Monogr. Ser., vol. 182*, edited by S. Calvari, et al., pp. 65–80, AGU.

Tibaldi A. (2001), Multiple sector collapses at Stromboli Volcano, Italy: how they work, *Bull. Volcanol., 63*, 112–125, doi:10.1007/s004450100129.

Tinti, S., A. Manucci, G. Pagnoni, A. Armigliato, and F. Zaniboni (2005), The 30 December 2002 landslide-induced tsunamis in Stromboli: Sequence of events reconstructed from the eyewitness accounts, *Nat. Hazards Earth Syst. Sci., 5*, 763–775.

Tinti S., A. Maramai, A. Armigliato, L. Graziani, A. Manucci, G. Pagnoni, and F. Zaniboni (2006), Observations of physical effects from tsunamis of December 30, 2002 at Stromboli Volcano, Southern Italy, *Bull. Volcanol., 68*, 450–461, doi:10.1007/s00445-005-0021-x.

Tommasi,P., P.Baldi, F.L.Chiocci, M.Coltelli, M.Marsella, and C. Romagnoli (2008), Slope failures induced by the December 2002 eruption at Strom-boli volcano in *The Stromboli Volcano: An Integrated Study of the 2002–2003 Eruption, Geophys. Monogr. Ser., vol. 182*, edited by S. Calvari, et al., AGU.

Turcotte, D.L. (1986), Fractals and fragmentation, *J. Geophys. Res., 91*, 1921–1926.

Valade, S., G. Lacanna, D. Coppola, M. Laiolo, M. Pistolesi, D. Delle Donne, and C. Cigolini (2016), Tracking dynamics of magma migration in open-conduit systems, *Bull. Volcanol., 78*(11), 78.

Vandaele A.C., Simon P.C., Guilmot J.M., Carleer M., Colin R. (1994), SO_2 absorption cross section measurements in the UV using a Fourier transform spectrometer, *J. Geophys. Res., 99*, 25599-25605.

Vergniolle S., Brandeis G. (1996), Origin of sound generated by Strombolian Explosions, *Geophys. Res. Lett., 21*, 1959-1962.

Vergniolle S., Brandeis G., Mareschal J.C. (1996), Strombolian explosions: 2. Eruption dynamics determined from acoustic measurements, *J. Geophys. Res., 101*(B9), 20449–20466.

Waite, G. P., P. A. Nadeau, and J. J. Lyons (2013), Variability in eruption style and associated very long period events at Fuego volcano, Guatemala, *J. Geophys. Res. Solid Earth, 118*, 1526–1533, doi:10.1002/jgrb.50075.

Watson I.M., C. Oppenheimer, B. Voight, P.W. Francis, A. Clarke, J. Stix, A. Miller, D.M. Pyle, et al. (2000), The relationship between degassing and ground deformation at Soufriere Hills Volcano, Montserrat, , *J. Volcanol. Geotherm. Res., 98*, 117-126, doi.org/10.1016/S0377-0273(99)00187-0.

Weibring P., Edner H., Svanberg S., Cecchi, G., Pantani L., Ferrara R., and Caltabiano T. (1998) Monitoring of volcanic sulphur dioxide emissions using differential absorption lidar (DIAL), differential optical absorption spectroscopy (DOAS), and correlation spectroscopy (COSPEC), *Appl. Phys., B67*, 419-426.

Weibring P, Swartling J, Edner H, Svanberg S, Caltabiano T, Condarelli D, Cecchi G, Pantani L (2002) Optical monitoring ofvolcanic sulphur dioxide emissions: comparison between fourdifferent remote-sensing spectroscopic techniques, *Opt. Las. El., 37*, 267–284.

Welch, P.D. (1967), The Use of Fast Fourier Transform for the Estimation of Power Spectra: A Method Based on Time Averaging Over Short, Modified Periodograms.,*IEEE Transactions on Audio Electroacoustics* AU-15 (2), 70–73, doi:10.1109/TAU.1967.1161901.

Williams-Jones, G., Horton, K. A., Elias, T., Garbeil, H., Mouginis-Mark, P. J., Sutton, A. J., Harris, A. J. L. (2006), Accurately measuring volcanic plume velocity with multiple UV spectrometers, *Bull. Volcanol., 68*, 328-332, doi:10.1007/s00445-005-0013-x.

Wilson L. (1980), Relationship between pressure, volatile content and eject velocity in three types of volcanic explosion, *J. Volcanol. Geotherm. Res., 8*, 297‐313.

Wilson, L., and J.W. Head (1981), Ascent and Eruption of Basaltic Magma on the Earth and Moon, *J. Geophys.Res., 86* (B4), 2, 971-3001, doi:10.1029/JB086iB04p02971.

Wilson, L., and Self, S. (1980), Volcanic explosions clouds: density, temperature, and particlecontent estimates from cloud motion, *J. Geophys. Res., 85* (B5), 2567–2572.

Young S., Francis P.W., Barclay J., Casadevall T.J., Gardner C.A., Darroux B., Davies M.A., Delmelle P., Norton G.E., Maciejewski A.J.H., Oppenheimer C., Stix, J. Watson, I.M. (1998), Monitoring SO_2 emission at the Soufriére Hills volcano: implications for changes in eruptive conditions, *Geophys. Res. Lett., 25*, 3681.

Young S., Voight B., Duffell H. (2003), Magma extrusion dynamics revealed by highfrequency gas monitoring at Soufrière Hills volcano, Montserrat, In: Oppenheimer, C., Pyle, D.M., Barclay, J. (Eds.), Volcanic Degassing: Special Publications, vol. 213, *Geol.Soc. London*, 219–230.

Zakšek K, Hort M, Lorenz E (2015), Satellite and ground based thermal observation of the 2014 effusive eruption at Stromboli Volcano, *Remote Sens., 7*, 17190–17211, doi:10.3390/rs71215876.

Zapata G.J.A., Calvache V.M.L., Cortes J.G.P., Fischer T.P., Garzon V.G., G.mez M.D., Narvaez M.L., Ordonez VM, Ortega EA, Stix J, Torres CR, Williams SN (1997), SO_2 fluxes from Galeras volcano, Colombia, 1989-1995: progressive degassing and conduit obstruction of a Decade Volcano, *J. Volcanol. Geotherm. Res., 77*, 195-208.